Jørgen Skogstad

Shear-driven and Static winterization of Algae oil: Impact on crystal morphology and separation efficiency

Bachelor's thesis in Food Science, Technology and Sustainability
Supervisor: Kirill Mukhatov
Co-supervisor: Ignat Tolstorebrov
May 2024

Bachelor's thesis

NTNU
Norwegian University of
Science and Technology

Jørgen Skogstad

Shear-driven and Static winterization of Algae oil: Impact on crystal morphology and separation efficiency

Bachelor's thesis in Food Science, Technology and Sustainability
Supervisor: Kirill Mukhatov
Co-supervisor: Ignat Tolstorebrov
May 2024

Norwegian University of Science and Technology
Faculty of Natural Sciences
Department of Biotechnology and Food Science

NTNU
Norwegian University of
Science and Technology

Sammendrag

Formålet med denne oppgaven var å undersøke skjærstyrt og statisk vinterisering, og deres respektive påvirkinger på krystallmorfologier og separasjonseffektivitet i algeolje.

For å gjøre dette ble algeolje vinterisert ved flere temperaturintervaller, med den flytende fraksjonen som utgangspunkt i hver påfølgende vinterisering. Vinteriseringen ble utført i to parallelle forsøk, hvor den skjærstyrte vinteriseringen ble utsatt for skjærkrefter i form av en magnetisk omrører, mens den statiske vinteriseringen hadde fravær av skjærkrefter. Krystallmorfologiene som ble dannet under krystalliseringen ble undersøkt under et mikroskop og sammenlignet. Separasjonseffektiviteten ble også evaluert for begge metoder og hvert temperaturinterval.

I tillegg ble de termodynamiske egenskapene og fettsyresammensetningen av alle fraksjonene analysert. Termodynamiske egenskaper ble undersøkt ved bruk av differensiell skanningskalorimetri (DSC). Fettsyresammensetningen av prøvene ble undersøkt ved bruk av gasskromatografi (GC) og konvertering av triglyserider til fettsyremetylestere.

Undersøkelsene viste at vinterisering uten skjærkrefter viste seg å være mer effektiv sammenlignet med påføring av skjærkrefter under vinterisering, og i tillegg ga krystaller med større gjennomsnittlig diameter. Krystallmorfologiene dannet under statisk vinterisering var lettere å separere, og førte generelt til en høyere separasjonseffektivitet. Dette ble også styrket av GC-analyseresultatene, som viste at den statiske vinteriseringen ga en bedre separasjon av fraksjonene som ble dannet, sammenlignet med den skjærstyrte vinteriseringen. Det er imidlertid viktig å merke seg at skjærhastigheten som ble brukt i oppgavenes eksperimenter kan ha overskredet en kritisk skjærhastighetsgrense, og derfor hatt en overordnet negativ innvirkning med hensyn til krystalldannelse. Å bruke en lavere skjærhastighet kunne ha drastisk endret resultatene på en fordelaktig måte. DSC-resultatene som ble oppnådd bekreftet også at vinterisering var en effektiv metode for å separere triglyserider i olje, basert på smeltepunkt.

Fra resultatene som ble oppnådd i denne oppgaven, viste vinterisering utført uten skjærkrefter seg å være mer fordelaktig, men dette kan skyldes at skjærhastigheten brukt i den skjærstyrte vinteriseringen kan ha hatt en negativ effekt på separasjon og krystalldannelse. Å bruke en lavere skjærhastighet kunne ha ført til et mer fordelaktig resultat for den skjærstyrte vinteriseringen.

Abstract

The purpose of this thesis was to investigate shear-driven and static winterization, and their respective effects on crystal morphologies and separation efficiency in algae oil.

To do this, algae oil was winterized at multiple temperature ranges, with the liquid fraction being the subject for each subsequent winterization. The winterization was performed in two parallels, where the shear-driven winterization was subject to shear-forces by form of a magnetic stirrer, while the static winterization had an absence of shear-forces. The crystal morphologies formed during crystallization was investigated under a microscope and compared. The efficiency of separation was also evaluated for both methods and each temperature range.

Additionally, the thermodynamic properties and fatty acid composition of the samples obtained was analyzed. Thermodynamic properties were investigated by use of differential scanning calorimetry (DSC). The fatty acid composition of the samples were investigated by use of gas chromatography (GC) and converting the triacylglycerides to fatty acid methyl esters.

The investigations showed that winterization with an absence of shear-force proved to be more efficient compared to applying shear-force during winterization, and additionally yielded crystals with larger average diameters. The crystal morphologies formed during static winterization were easier to separate, and overall led to a higher separation efficiency. This was also strengthened by the GC-analysis results, which showed that the static winterization yielded a better separation of the fractions which were obtained, compared to the shear-driven winterization. It is however important to note that the shear-rate which was utilized in the thesis' experiments may have exceeded a critical shear-rate limit, and therefore had an overall negative impact in regard to crystal formation. Utilizing a lower shear-rate may have drastically altered the results in a beneficial manner. The DSC results obtained also confirmed that winterization was an effective method of separating triacylglycerides in oils, based on melting points.

From the results obtained in this thesis, winterization performed with an absence of shear-forces proved to be more beneficial, though the shear-rate utilized in the shear-driven winterization may have had a negative effect on separation and crystal formation. Utilizing a lower shear-rate may have led to a more beneficial result for the shear-driven winterization.

Forord

Denne oppgaven er skrevet som en avsluttende del av studiet «Matvitenskap, teknologi og Bærekraft» ved Institutt for bioteknologi og matvitenskap i Trondheim ved NTNU. Oppgaven ble skrevet på bakgrunn av den økende viktigheten av bærekraftig prosessering av marine lipider, noe som er svært viktig for Norsk næring og eksportindustri. De praktiske eksperimentene i oppgaven tok hovedsaklig sted ved Institutt for energi og prosessteknikk på Gløshaugen kampus. GC-analyse ble utført ved Institutt for bioteknologi og matvitenskap på Kalvskinnet kampus.

Jeg vil takke NTNU som dekket alle kostnader i oppgaven, og en takk til GC Rieber som leverte algeoljen som ble brukt som basis for alle eksperimenter i oppgaven.

Jeg ønsker også å rekke en stor takk til veilederne mine, Ignat Tolstorebrov og Kirill Mukhatov. Deres støtte under hele oppgaven har vært til en utrolig stor hjelp. Veiledning deres har hjulpet meg i mål, og gitt meg utrolig mye læring. Kaffepratene våre på kontoret var alltid en trivelig seanse, og noe jeg alltid så fram til. Videre vil jeg også takke John-Kristian Jameson som assisterte med GC-analyse på Kalvskinnet.

Jeg ønsker også å takke Kristi Ekrann Aarak som mottok meg på besøk ved GC Rieber i Kristiansund og viste meg rundt på anlegget. Det var veldig interessant å se bedriften og trivelig å møte alle som arbeidet der!

Jørgen Skogstad

Trondheim, 20.05.2024

Contents

Nomenclature

TAG - Triacylglyceride

FA – Fatty acid

SFA – Saturated fatty acid

PUFA – Polyunsaturated fatty acid

EE – Ethyl ester

FAME – Fatty acid methyl ester

DHA – Docosahexaenoic acid

EPA – Eicosapentaenoic acid

DSC – Differential scanning calorimetry

GC – Gas chromatography

rT – Retention time

$T_{g\ onset}$ – The temperature in which a glass transition starts occurring.

$T_{g\ end}$ – The temperature in which a glass transition is completed.

ΔH_{fus} – The amount of energy in J/g which is needed to convert a substance from a liquid to a solid phase.

List of figures

List of tables

1. Introduction

Fish oil stands as an important industry that encompasses processing of oils for human consumption (Pike & Jackson, 2010). Global fish oil production has remained stable at roughly 1 – 1.25 million tons yearly, which is a show of sustainability. The usage of fish oil in a purified form as dietary supplements (nutraceuticals) is also an important area, showing the need for sustainable and food-grade marine oils. Though a good source of ω-3/6 fatty acids, alternatives to fish for the same fatty acids have been explored, and of particular interest are marine protists (microalgae). They are regarded as a viable alternative to supply ω-3/6 fatty acids, due to their more sustainable cultivation strategies and PUFA content (Russo et al., 2021).

Of rising importance is the need for sustainable processing methods of food-grade oils. Many of the steps in this processing is very energy demanding, and of particular concern is winterization. Winterization is based on separating TAGs by utilizing their differing crystallization and melting points (Kreulen, 1976). Pre-processed oils are often comprised of several TAGs, which again are comprised of a plethora of fatty acids. Separating them from one another allows for further processing of high-purity fractions for respective products. Due to the large volumes which need to be heated and cooled, winterization stands as an energy demanding process, and as such exploring sustainable methods to do so is of great importance.

Research on vegetable oils and their behavior during winterization is quite extensive when compared to their marine counterparts, which may be considered lacking. This demonstrates the importance of investigating winterization of marine lipids, and the circumstances and parameters that affect their behavior. The aim of this thesis is to investigate winterization of algae oil, and in particular the impact different winterization methods have on crystal morphologies and separation efficiency. Of interest here, is shear-driven and static winterization. This gives rise to the thesis focus:

"How does shear-driven and static winterization of algae oil respectively affect the formation of crystal morphologies and separation efficiency?"

2. Theory

2.1 - Lipids

2.1.1 – Triacylglycerides

Triacylglycerides, commonly abbreviated TAG's, are organic compounds consisting of three fatty acids bound to a glycerol molecule. Figure 1 describes the general structure of a given triacylglyceride, denoting the positions of the fatty acids and the glycerol molecule. The physical properties of TAG's may have significant implications on the organoleptic and technological aspects of foods. Especially the aggregate state of TAG's has a great implication on the mouthfeel and consistency of certain foods, such as butter. At given temperatures TAG's can exist in either a liquid or solid state, where the latter is a crystalline form. The solid-liquid state of any given TAG's is dependent on several factors, as described by Walstra (1987). Particularly the fatty acid residues are responsible for the temperatures at which these aggregate states occur. Instead of having a specific melting point, like most compounds do, TAG's have a melting range as a result of the respective fatty acids' property to have different melting points. This results in TAG's being able to have certain fatty acids that exist in a liquid state, while others still exist in a crystalline state, where they may dissolve in the liquid phase of the lower melting point fatty acids. TAG's also have a clear point, meaning a temperature where the crystals with the highest melting points finally convert to a liquid state. In addition to these aspects, TAG's also exhibit crystalline properties when in a solid phase, and particularly they have the ability to crystallize into different polymorphic configurations. This crystallization occurs when the TAG's reach a certain temperature that allows for a phase-transition to occur, and when sufficient nucleation opportunity is present. In doing so, the TAG's may crystallize into either a α, β' or β configuration. These different configurations in turn affect the structure and symmetry of the solid phase that is formed.

Triacylglycerides are an important component of fish, though the exact percentage composition compared to other components such as proteins, water, carbohydrates etc. is highly variable due to several factors. Seasonal variations, differences between species, climate, feeding regiment and age are only a few to name. For some fish such as herring, the content might be as low as 2%, all the way up to 25% (Petricorena, 2015).
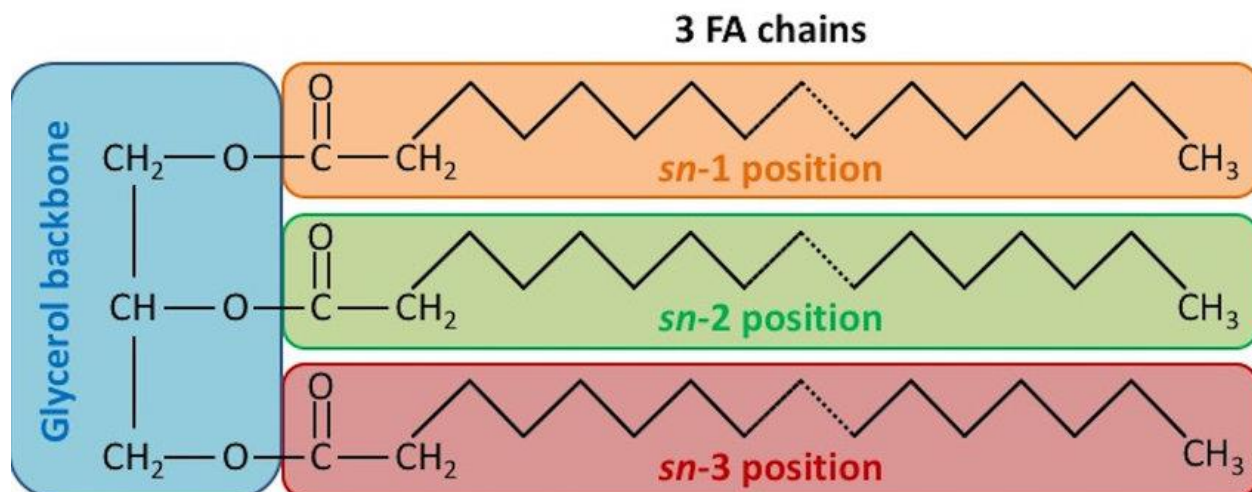
Figure 1: A schematic overview of a general saturated triacylglyceride with notations for the sn-1,2,3 positions, and the glycerol molecule forming the backbone (Alfieri et al., 2017).

There are several factors which impact the melting points of a given triacylglyceride. Table 1 gives a general overview of the variations in thermal properties of pure TAGs, meaning TAGs that only consist of one specific fatty acid. As may be observed in conjunction with the table, the fatty acid residues which make up the composition of the triacylglyceride are cardinal in deciding the melting point for that specific TAG, but these will be discussed in section 2.1.2. Eminently, the position of the given fatty acid residues on the triacylglyceride has a significant impact on the melting point. A more symmetrical structure of the TAG as a consequence of the positioning, here regarding the respective sn-1/2/3 positions, allows the TAG to pack itself more tightly with neighboring molecules, which leads to an increase in melting point (Walstra, 1987). Consequently, TAGs with an asymmetrical conformation are more prone to steric hindrance which makes packing tightly with neighboring molecules more challenging. This leads to a decrease in melting point. The main factor deciding the symmetry of a TAG is highly dependent on the fatty acid residues bound to the glycerol backbone, however aside from this the positioning of the fatty acid residues on a given TAG is also random, which might give subtle variations in melting points.

Table 1: Thermal properties of mixed TAGs with the fatty acid composition, abbreviation, temperature of glass transition, polymorphism and melting temperature, and the heat of fusion for the respective β-crystals.

Nomenclature	Fatty acid	Abbreviation	Glass transition (°C)	Polymorphism, melting temperature (°C)	B-crystals heat of fusion (J g^{-1})
Triolein (9c); 1,2,3-tri-(9Z-hexadecenoyl)-sn-glycerol	18:1ω9c	OOO	Not detected	α = -35,0 β' = -15,6 β = +1,5	113,0
Tripalmitolein (9c); 1,2,3-tri-(9Z-hexadecenoyl)-sn-glycerol	16:1ω9C	PoPoPo	Not detected	α = -25,5 α' = -21,6 β = -13,1	103,2
1,2-Palmitolein-3-Olein;1,2-di-(9Z-hexadecenoyl)-3-(9Z-octadecenoyl)-sn-glycerol	16:1ω9C (2x) 18:1ω9C	PoPoO	Not detected	α = -27,4 β = -14,5	94,8
1,2-Palmitin-3-Olein;1,2-dihexadecanoyl-3-(9Z-octadecenoyl)-sn-glycerol	16:0 (2x) 18:1ω9C	PPO	Not detected	α = +17,0 β' = +27,9 β = +31,1	132,6
Trilinoelaidin (9tr,12tr);1,2,3-tri-(9E,12E-octadecadienoyl)-sn-glycerol	18:2ω(9tr,12tr)	GLAx3	Not detected	α = -25,1 β = +16,0	106,4
Trilinoleinin(9c,12c,15c);1,2,3-tri-(9Z,12Z,15Z-octadecatrienoyl)-sn-glycerol	18:3ω(9c,12c,15c)	LnLnLn	T_{go} = -112,6 T_{gi} = -109,0 T_{ge} = -99,7 T_{cc} = -68,5	α = -47,7 β = -24,8	62,1
Trieicosenoin (11c);1,2,3-tri-(11Z-icosenoyl)-sn-glycerol	20:1ω11c	EeEeEe	T_{cc} = -2,4	β = +17,27	140,7
1,2-Olein-3-Linolein;1,2-di-(9Z-octadecenoyl)-3-(9Z,12Z-octadecadienoyl)-sn-glycerol	18:1ω9C (2x) 18:2ω(9c,12c)	OOLi	T_{cc} = -57,3	β = -17,2	76,5
1,3-Olein-2-Palmitin;1,3-di-(9Z-octadecenoyl)-2-hexadecanoyl-sn-glycerol	18:1ω9C 16 18:1ω9C	OPO	T_{cc} = +6,1	β = +18,5	140,2

1,2-Linolein-3-Palmitin1,2-di-(9Z,12Z-octadecadienoyl)-3-hexadecanoyl-sn-glycerol	18:2ω(9c,12c) (2x) 16	LiLiP	T_{go} = -121,1 T_{gi} = -117,5 T_{ge} = -113,9 T_{cc} = -33,3	β = -8,3	78,3
1,3-Linolein-2-Olein;1,3-di-(9Z,12Z-octadecadienoyl)-2-(9Z-octadecenoyl)-sn-glycero	18:2ω(9c,12c) 18:1ω9C 18:2ω(9c,12c)	LnOLn	T_{cc} = -75,4	β = -21,9	76,4
1,3-Palmitin-2-Myristin;1,3-dihexadecanoyl-2-tetradecanoyl-sn-glycerol	16 14 16	PMP	Not detected	β = 17,8	119,3
1,2-Olein-3-Linolenin1,2-di-(9Z-octadecenoyl)-3-(9Z,12Z,15Z-octadecatrienoyl)-sn-glycerol	18:1ω9C (2x) 18:3ω(9c,12c,15c)	OOLn	Not detected	β = -16,3	78,4

2.1.2 – Fatty acids

Fatty acids are a large group of compounds, which are made of a long chain of hydrocarbons connected to a carboxyl group (Coultate, 2023). Figure 2 gives an overview of the structures of common fatty acids, showcasing their structure and the structural differences that may occur as a result of double bonds in the acyl chain. The melting point for a given fatty acid is dependent on several factors, which in turn affects a given TAG's melting range and aggregate state (Walstra, 1987). Table 2 gives an overview of some fatty acids' melting points and the enthalpy. The chain length of a fatty acid residue affects the melting point, and longer chain length leads to a higher melting point. The bonds between the carbon molecules in the fatty acid will also affect the melting point. A higher amount of double bonds (unsaturated) will decrease the melting point, and consequently singular bonds will increase it. These double bonds also give rise to double bond stereoisomerism, which is where the double bonds occur as either a cis or trans configuration. Trans double bonds give a lower melting point, due to allowing the acyl chain to align in a linear conformation (similar to a single bond), while a cis bond gives rise to a conformational kink. This kink gives rise to asymmetry, which in effect may lower the melting point of the fatty acid. In addition, the position of any given double bonds may affect the melting point as well. Conjugated double bond pairs allow for a linear conformation, which increases the

melting point compared to irregular or singular double bonds. Branching of the acyl chain may also decrease the melting point. All of these aspects affect the symmetry and the distribution of the fatty acids, which in effect has an impact on the total melting range of the TAG.

Table 2: A table giving an overview of some free fatty acids, their melting points, the melting enthalpy (i.e. the energy needed to perform a phase transition), and the heat of fusion. (Sathivel et al., 2008).

Free fatty acids	Onset temperature (melting point °C)	Maximum temperature (°C)	Melting enthalpy (kJ/kg)	Heat of fusion ΔH (kJ/mol)
C14:0	53,5	55,5	198,3	45,8
C16:0	59,8	63,9	212,8	53,9
C18:0	67,6	70,0	226,3	61,3
C20:0	70,6	75,8	236,9	53,2
C16:1	-0,90	1,64	125,8	32,1
C18:1	-5,7	15,2	152,2	39,6
C18:2	-13,0	-4,1	119,1	51,5
C18:3	-21,0	-10,4	115,0	48,7
C20:2	-8,3	0,9	103,1	53,7
C20:4	-43,4	-38,4	113,3	54,1
C22:6	-47,4	-42,2	82,1	59,6
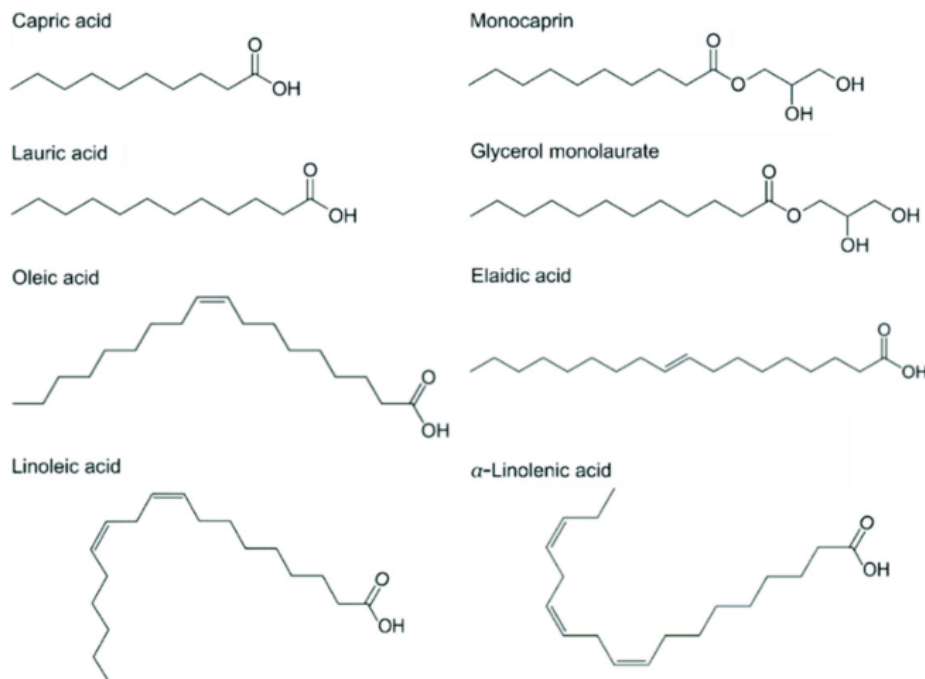
Figure 2: An overview of common fatty acids showcasing their structure and the structural differences that occur as a result of variance in double bonds. An increased amount of double bonds in different positions may lead to greater steric hindrance (Yoon et al., 2018).

The fatty acids making up the compositions of the TAGs in fish is recognized by a high amount of long chained acyl-chains, monounsaturated bonds and polyunsaturated bonds (McGill & Moffat, 1992). While the exact ratios of these fats in relation to one another may vary, there is generally a high amount of polyunsaturated fatty acids (PUFA), which leads to fish oils generally existing in a liquid-phase at room temperature. Concordantly, seasonal variations and other factors that affect the total fat content may lead to variations in the exact proportions of monounsaturated/polyunsaturated fat to saturated fats.

2.1.3 – Ethyl esters

Ethyl esters (EE) are a group of compounds commonly synthesized from fish oil. They consist of a fatty acid, with its carboxyl group, connected to the hydroxyl group of ethanol. EE's are synthesized by subjecting TAG's from fish oil to base-catalyzed transesterification in an ethanol solution (Sullivan et al., 2009). In this process, the alkyl chain in ethanol is connected to the hydroxyl group of the TAG, and an ethyl ester is formed. The following EE oil contains ethyl esters of all the respective fatty acids that the TAG mixture contained and can be fractioned to extract the desired fatty acids. Figure 3 describes a general reaction process which is used to produce ethyl esters, more specifically fatty acid ethyl esters.
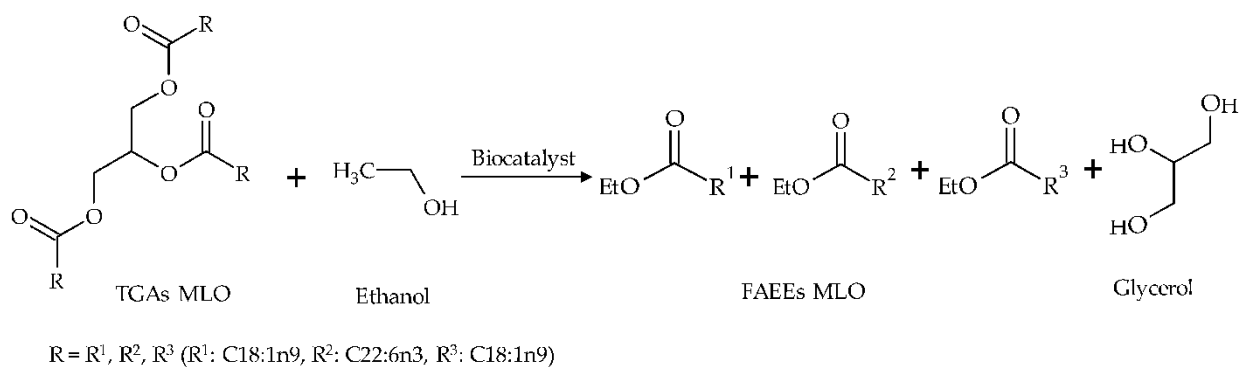
Figure 3: An overview of the reaction process producing fatty acid ethyl esters from TAGs. The process is driven by a biocatalyst that reacts ethanol and a TAG to produce fatty acid ethyl esters and glycerol. (Aguilera-Oviedo et al., 2021)

2.2 – Lipid crystallization

As previously mentioned, TAG's exhibit the ability to form crystals when transforming from a liquid state to a solid state. Specifically, they are able to form different polymorphic configurations. These configurations, α, β' or β, have varying degrees of stability, where the latter is the most stable in terms of thermodynamic stability (Smith, 2001). The designations α, β' or β, refer to the chain packing, or rather the three-dimensional alignment of the acyl chains in relation to each other, for a given polymorphic configuration. In reality the possible different packing modes and different crystal lattices which may form during crystallization are profusely abundant (Walstra, 1987), so for simplicity's sake these three simple designations are given. These given designations may however also have additional forms, such as α which has a sub-α mode that exhibits lower stability than α.

The different polymorphic configurations have varying three-dimensional structures, which impact their thermodynamic stability and melting point (Smith, 2001). In the α form, the crystals have a hexagonal arrangement which exhibits little symmetry compared to the β' and β forms, and the acyl chains are randomly orientated. Figure 4 shows the orientations of the acyl chains and spatial arrangements between them for different polymorphic configurations. In the β' form the melting point and thermodynamic stability is increased, compared to the α form, and the crystals show a degree of symmetry. The acyl chains are now orientated perpendicularly and are packed together in an orthorhombic structure. For the β configuration, the melting point and thermodynamic stability is higher. Here the acyl chains are orientated parallel to one another and are packed in a rhomboid structure.

Figure 4: The polymorphic configurations α, β' and β, which a given TAG may crystallize into. The configurations exhibit increasing melting points and thermodynamic stability from left to right (Smith, 2001)

Lipid crystallization in itself is a process which has several steps. First and foremost, to convert a given lipid from a liquid to a solid state, a thermodynamic driving force must be generated to allow for crystallization (Hartel & Kaylegian, 2001). This is in most cases the removal of heat through cooling, i.e. energy is removed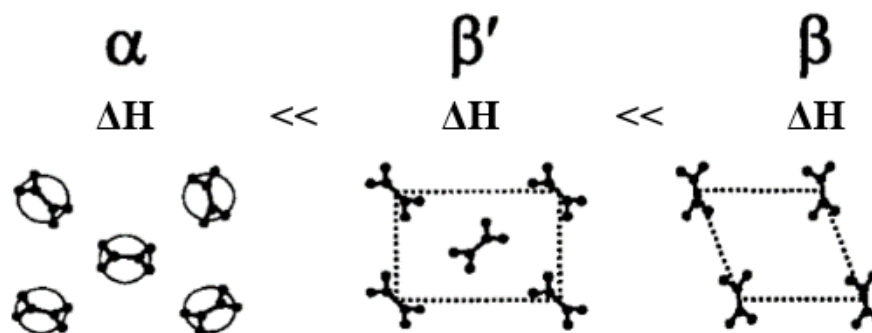 from the system through heat transfer. When sufficient energy has been removed, the system reaches a state of nonequilibrium, where an imbalance is created. This imbalance allows for the nucleation of crystals from the liquid phase, meaning that a new thermodynamic phase is being formed. These crystals continue to form until a thermodynamic equilibrium is once again attained. This equilibrium persists until the temperature changes again, which may lead to either an increase in the crystal phase volume, or a reduction of it.

Markedly, the formed crystals may also crystallize as the aforementioned polymorphic configurations. Whichever polymorphic configuration is formed depends on several factors, however the rate of cooling on the liquid phase is a significant aspect (Smith, 2001). Figure 5 gives an overview of the thermodynamic conditions necessary to form the different polymorphic configurations, as well as polymorphic transitions between them. A rapid cooling of the liquid phase forms sub-α crystals, which is the least stable configuration in terms of thermodynamic stability. However, this configuration is quite transient due to its thermodynamic stability and is quickly transformed to the α phase upon further cooling. A slightly slower cooling may also initially yield the α configuration and avoid the ephemeral sub-α phase. Heating of this α form may also yield the more stable β' form. Alternatively cooling above the α form's melting point will yield the β' form. The most stable configuration, the β form, is formed either by heating the β' form, or exposing the liquid phase to an even slower cooling. These phase transitions between the different polymorphic configurations are also notably irreversible, with respect to the most stable form. This means that crystals formed in a given polymorphic configuration may only transform to a polymorphic configuration with a higher degree of thermodynamic stability (unless of course the solution is reverted to a liquid phase).
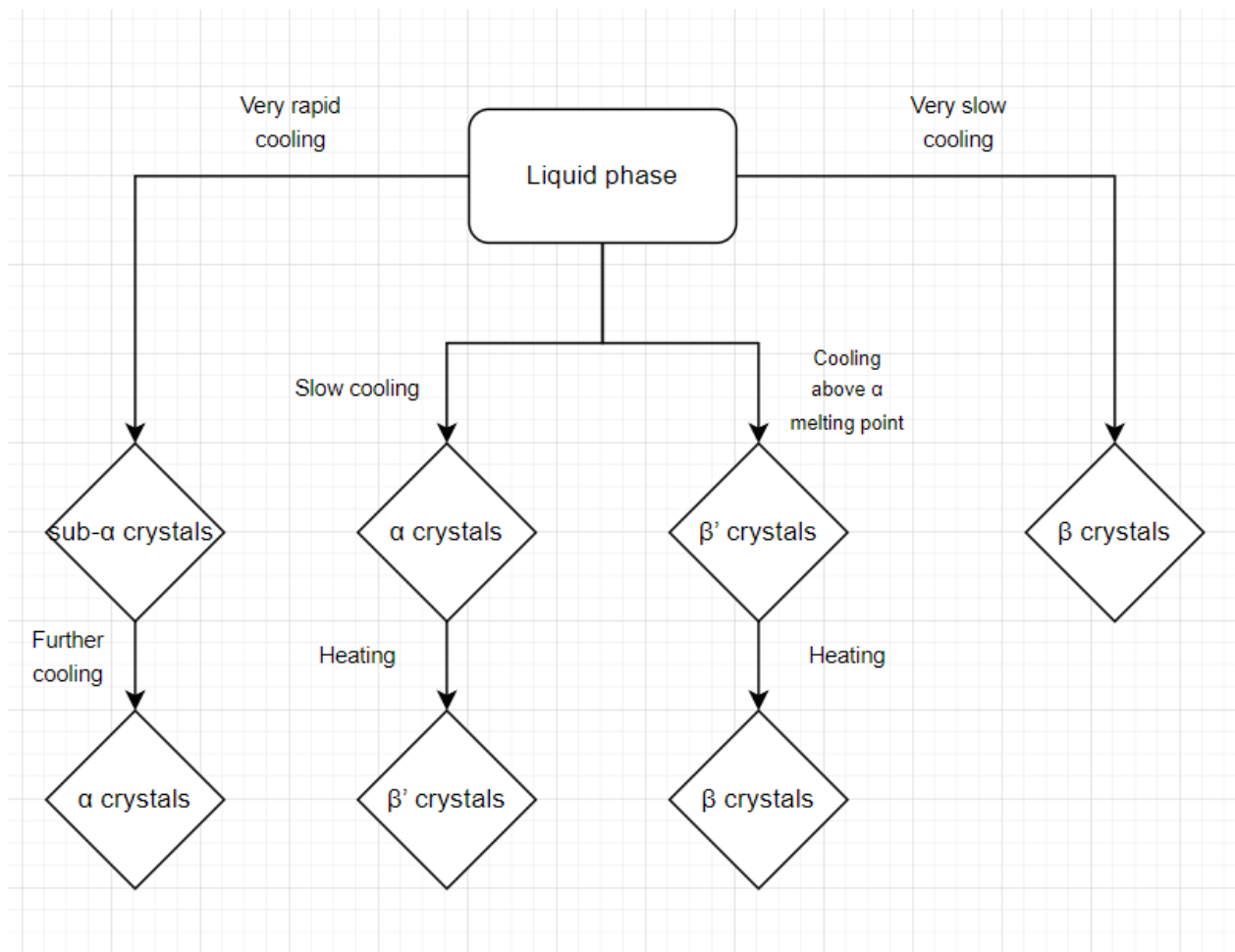
Figure 5: An overview of thermodynamic conditions needed to form the respective polymorphic configurations, and the transitions between them.

Another significant phenomenon which takes place during lipid crystallization is the formation of compound crystals. In most practical applications, a fat will contain a plethora of different TAG's, which in turn leads to a wide range of melting ranges and polymorphic conformations. This gives rise to the formation of compound crystals, which are crystals that incorporate one or more TAG's (Tran & Rousseau, 2016). These compound crystals may exhibit properties that incorporate the respective incorporated TAGs' properties, especially thermodynamically. Such compound crystals typically form in the α conformation but are generally short-lived and transition to a β' marked configuration. The formation of compound crystals in a given fat is often not homogenous, as other compound crystals with differing TAG compositions may also readily form. This occurrence also increases depending on the composition of the fat which is crystallizing. Namely, milk fat exhibits a wide variation in its TAG composition with up to 400

different TAG species (Hartel & Kaylegian, 2001). As such, the different compound crystal combinations which are able to form during initial crystallization are complex and varied.

2.3 – Crystallization and structure formation

The process of crystallization is a complex process with several factors and aspects which affect the outcome. Of particular importance is the structure which is formed during crystallization. With the transition from a liquid-phase to a solid one, a crystalline fat network is formed within the liquid-phase. Additionally, during crystallization, there is not only a singular process taking place which leads to a given outcome. Several phenomena take place at any given time, all of which affect the resulting crystal formation (Walstra et al., 2001). Figure 6 gives a general description of the most significant factors and processes taking place during crystallization of a given fat.

Figure 6: A general overview of the different factors and processes which affect the crystallization of a given fat, and the resulting crystalline structures at different points in time (Walstra et al., 2001)
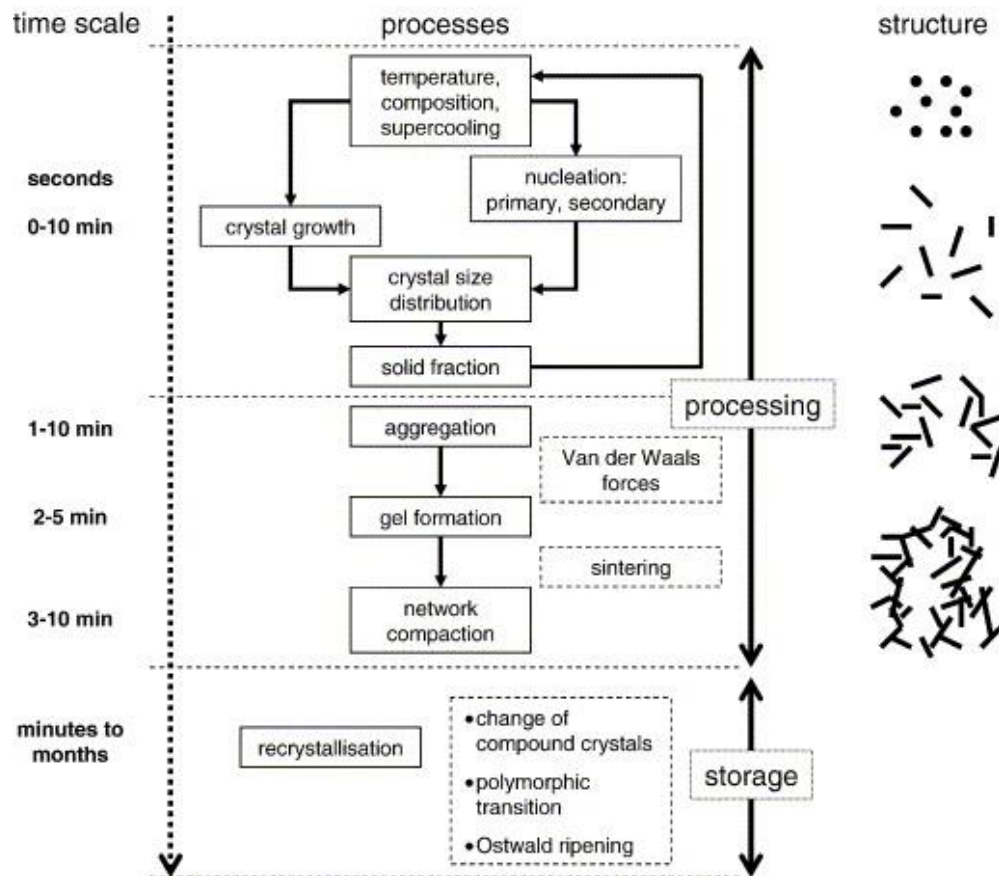
As Figure 6 describes the time scale over which crystallization takes place ranges from just a few seconds to months. Though we may generally divide the process into three different phases: initial crystallization, structure formation and long-term changes. The initial crystallization is dependent on the three major factors: temperature, composition and supercooling. The temperature aspect is cardinal due to deciding which FAs in a given TAG are able to crystallize due to the absence of thermodynamic equilibrium. This aspect also ties into the composition, which regards the composition of the given fat. Depending on the composition of the fat, a given number of FAs are able to transition to a solid-phase and form crystals, which affects the total solid-phase volume in the fat. Supercooling of the fat is also a crucial factor in terms of compound crystal formation, as described by Hartel & Kaylegian (2001). With a lower degree of crystallization kinetics, the degree of variation between the solid and liquid phases of the TAG composition is increased. Consequently, a higher degree of crystallization kinetics leads to a greater formation of compound crystals. All of these factors affect the crystal growth, their sizes and distribution in the liquid-phase of the fat. Generally, the structures formed in this initial phase are non-homogenous, small crystals distributed in the liquid-phase. A crystalline three-dimensional network has yet to be formed.

After the initial crystallization has taken place, a three-dimensional network may be formed by the crystals in the liquid-phase. This can take place due to the aggregation of the crystalline structures, and later on gel-formation and network compaction which forms a larger three-dimensional structure which has a huge practical implication on the fat and its properties. After the crystals reach a certain size, Van der Waals forces attract the crystals together and form a fractal aggregate (Walstra et al., 2001). This leads to the formation of the initial continuous network. The resulting network already affects the viscoelastic properties of the fat and gives it elastic properties, as opposed to freely distributed crystals which just increase the general viscosity of the solution in general. An especially significant phenomenon which takes place in this network formation phase is sintering. Sintering occurs when two adjacent crystals that aren't initially connected come into contact with each other. Figure 7 gives a visual representation of how sintering occurs between two non-connected crystals.
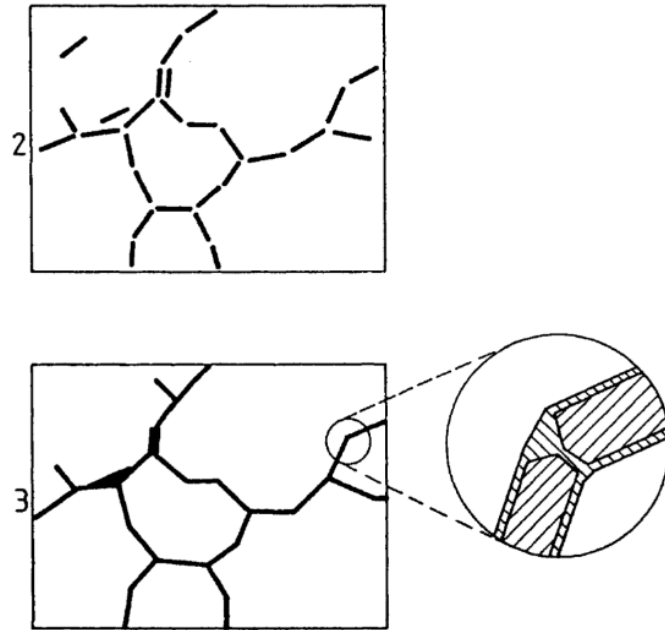
Figure 7: A 2D representation of sintering between crystals and the respective orientation of the crystals (Walstra et al., 2001)

Normally the orientation of the crystals in relation to each other doesn't allow for them to "grow on top" of each other. Due to this, sintering occurs which leads to the formation of a crystalline "bridge" between the two crystal-aggregates. The orientation of the crystals in this "bridge" is perpendicular to the connected crystals. This sintering allows for the connection of different crystals to form a crystalline three-dimensional network throughout the liquid-phase of the fat. Generally, during fast cooling more α crystals are formed than the other configurations. α crystals (and β') are more prone to sintering than the more stable β polymorph, which leads to an increased degree of sintering if a high degree of cooling is exerted on the fat.

After the structure formation within the fat has taken place, there may be several long-term changes that take place over time. Recrystallization following Ostwald ripening, polymorphic transitions and changes in compound crystals may affect the properties of the fat over time. Polymorphic transitions are most often done from a liquid-state, however over long-term storage solid-state transitions may occur (Tran & Rousseau, 2016). These polymorphic transitions lead to changes in the thermodynamic properties of the crystals, and as such affect the thermodynamic properties of the fat in general. Such changes in polymorphic configurations happen due to the internal energy of the crystals or their free surface energy continuing to decrease, eventually

reaching a thermodynamic minimum (Smith, 2001). During storage, the crystals are also generally never in a thermodynamic equilibrium, which leads to slow recrystallization over time and a deposit of more crystalline material into the network. This will increase the firmness of the fat over time. Ostwald ripening may also take place over time, which is a process where smaller crystals formed dissolve in the liquid-phase and then deposit onto larger crystals over time. This happens due to the fact that such a process favors the larger crystalline structures thermodynamically. This leads to an increase in the size of larger crystals and generally increases the size of the three-dimensional network in the fat.

2.4 – Winterization principles and methods

Winterization is an umbrella term for processes which separate particular fractions of fats and oils utilizing cooling, and sometimes solvents. The different methods used might vary depending on the desired fractions to be separated, the temperature range of the constituents of the fat/oil, available equipment and the volumes which are to be separated. However, all winterization processes are based on the principle of utilizing temperature reduction to separate the constituents of a fat/oil due to the different melting ranges of the TAG's which compose it. Kreulen (1976) describes the principles of industrial fractionation in three general steps which are performed consecutively. Firstly, liquid oil is cooled until it reaches supersaturation. This supersaturation comes as a result of solid TAG's that are dissolved in the liquid-phase of the oil reaching a point where no more solids are able to be dissolved. This brings the liquid-phase to a point of supersaturation, in which nuclei are formed that allow for crystallization. These nuclei are generally not formed homogenously throughout the liquid and may especially form on surfaces and imperfections that the liquid is in contact with. This leads into the second step, crystalline growth. As the nuclei are formed throughout the liquid-phase, as a result of the TAGs with a higher melting point being subject to cooling, the solid-phase takes shape as crystalline structures dispersed in the liquid-phase. The size, shape and volume of these crystalline structures may vary greatly depending on a plethora of factors (as discussed in previous sections), but in general they will keep growing as the temperature keeps being lowered, or until the oil is held at a specific temperature for long enough time. After sufficient crystallization has occurred, the last step of separation may take place. Due to the presence of a solid- and liquid-phase in the oil, they may be

separated with the use of filters that allow the liquid-phase to pass through but retain the solid-phase. In doing so, we obtain two different fractions, one solid and one liquid. These fractions exhibit different thermodynamic properties, mostly due to the compositional differences in the TAGs that are present in the respective fractions.

The current state of the art technology for winterization can be separated into three methods. Several different concepts and methods to perform winterization exist, though these three methods are the only ones which are mainly being used (or have been used) on industrial scales. Figure 8 describes the different winterization methods and the factors which differ them from one another.
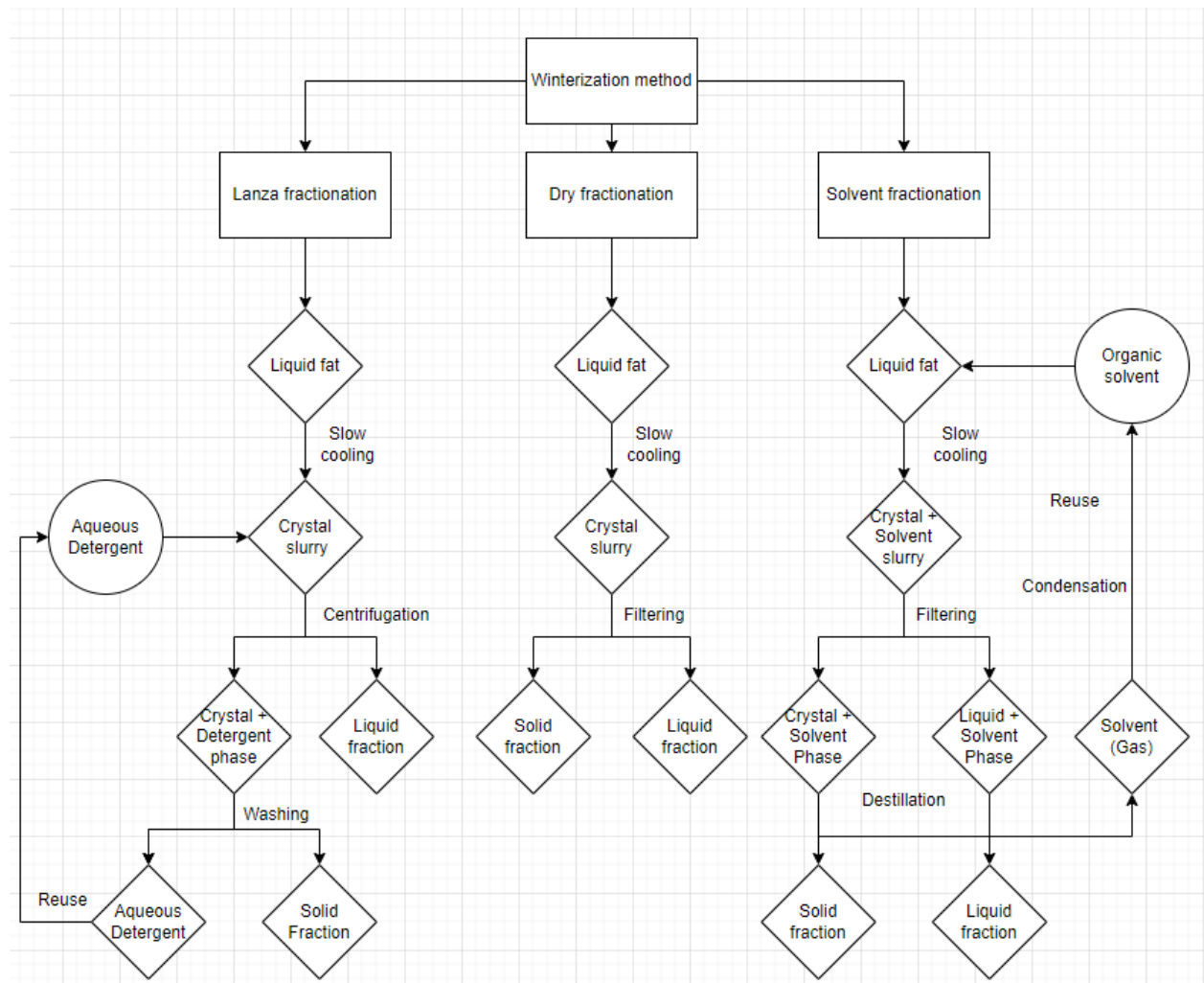

Figure 8: A flowchart describing the current state of the art technologies utilized in industrial winterization, and their differing factors.

These are dry fractionation, Lanza fractionation and solvent fractionation. Dry fractionation is the simplest process and is based on cooling an oil under controlled conditions without the addition of chemicals (Kreulen, 1976). In this process, oil is slowly cooled to the optimal temperature while crystallization occurs. After sufficient crystallization, a slurry has formed which may be filtered to separate the solid and liquid fractions. Lanza fractionation is a process which is quite similar to dry fractionation, however in this method an aqueous detergent is added to the oil after crystallization has occurred. Normal detergents are solutions containing lauryl sulphate and magnesium sulphate to act as an electrolyte. This detergent phase takes the place of the liquid-phase that is present on the surface of the crystalline solid-phase. This leads to the formation of an aqueous suspension of the crystals and detergent. The detergent and crystal phase have two properties that are exploited to separate them. Firstly, they are heavier than the oil-phase which means they will naturally sink to the bottom of the container they are in. Secondly, the aqueous nature of the detergent leads to a natural separation from the oil-phase, due to the polarity of the molecules. These two properties allow for separation through centrifugation, which separates the two fractions efficiently. After separation the detergent solution may be washed out from the crystalline phase and recycled for later use. Solvent fractionation is a process where an organic solvent is added to the oil prior to crystallization. Normal organic solvents utilized today are hexane and acetone. When subjected to cooling, this organic solvent allows for the precipitation of the solid phase mixed with the solvent. This leads to two phases being formed during crystallization. The liquid-phase which contains the oil and the solvent, and the solid-phase which contains the crystals and the solvent. These may then be separated with the use of a filter, and then distillation is utilized to remove the solvent phase. After distillation, the organic solvent may be recycled and used again.

In regard to the size and morphology of the crystals that are formed during winterization, the factors which may impact them are complex and contingent. Of particular importance is the cooling rate expressed in °C/min, and the shear forces (if any) that are applied upon the fat during cooling. The extent of research that has been done on marine oils specifically and the factors which impact crystalline formation, and their resulting rheology is lacking. However, similar research is extensive on vegetable oils, particularly due to their importance in the food industry. The cooling rate of the oil may lead to differing crystal morphologies and differences in mean particle sizes (Litwinenko et al., 2002). Slower cooling rates (1°C/min) may lead to a distinct

crystallization of separate fractions with different morphologies. The resulting morphologies may manifest as several formations, such as spherulites, rods, needles or finely dispersed granules. At low cooling rates the crystals may form into spherulitic conformations, which is also suggested to be related to the presence of β' polymorphs. A higher cooling rate, however, yields more needle-like morphology that is more finely dispersed throughout the solution. This higher rate of cooling may also lead to more uniform crystal morphologies throughout the oil. This also closely correlates to the polymorphic configurations of the crystals, where high cooling may lead to the formation of α' crystals. Inversely, slow cooling may also yield more thermodynamically stable polymorphs such as β' and β. The resulting sizes of crystals formed crystallization is dependent on several factors, and especially the constituents of the oil and the temperature range at which the solution is being separated over. In general, however, slower cooling rates may seem to yield larger mean sizes of crystals, due to the more non-homogenous formation of crystals, as this allows for crystals to grow independently and not be interdicted by neighboring crystals. Higher cooling rates may yield the opposite, due to a more homogenous crystallization throughout the solution, which resultantly may lead to crystals growing into each other and limiting their size. The size of the crystals is also often correlated to morphology. Typical morphologies seen are platelet-like crystals (<1μm), needles (1-5μm) and spherulites (5-20μm) (Nguyen et al., 2020). The crystals also often form aggregates together, which yield larger structures overall throughout the solution. Figure 9 showcases a 2D representation of the structures of the different crystal morphologies which may manifest in crystallized fats.

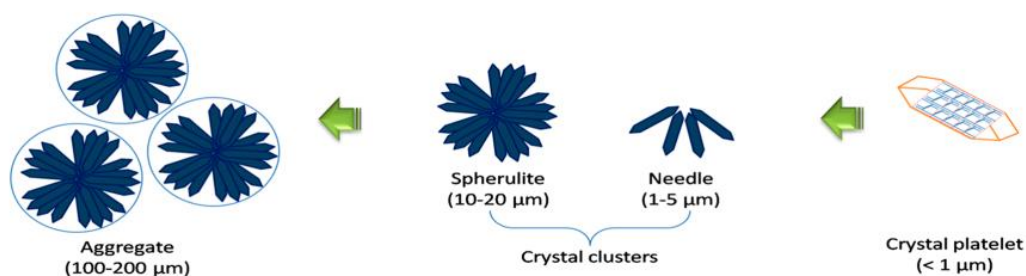*Figure 9: A 2D representation of some crystal morphologies that may manifest in crystallized fats (Nguyen et al., 2020b)*

Another important factor during winterization is the presence, or absence, of shear forces. In industrial practice, this is normally done through the use of scraped surface heat exchangers (SSHE). In smaller scales, this may alternatively be achieved through the use of magnetic

stirring. For static crystallization, the resulting crystals tend to manifest as spherulites (5-20μm) in β polymorphic configurations (Nguyen et al., 2020). The reasoning for this is not well understood, but some research seems to suggest it is a result of shear-forces leading to different orientations and nucleation of the crystals during crystallization (Tran & Rousseau, 2016). For dynamic crystallization, the resulting crystals tend to manifest as more spherical clusters of β' crystals. This is most likely as a result of the shear-forces promoting the aggregation and clustering of crystals during the crystallization process.

2.5 – Liquid-phase TAGs function as a solvent

In a given fat, there often exists a plethora of fatty acids, and consequentially a large number of TAGs. This also results in several fats that have different melting points and crystallization points. During crystallization and melting of a fat, there is also the possibility of TAGs interacting with one another as a result of their given phase, at a respective temperature in the solution. A significant point to consider in this is liquid-phase TAGs acting as a solvent for solid-phase TAGs in a solution. Figure 10 shows a visualization of the percentages of liquid-phase by volume of given TAGs at a given temperature range, where the increasing amount of liquid-phase by volume leads to an overall increase due to the TAG acting as a solvent.
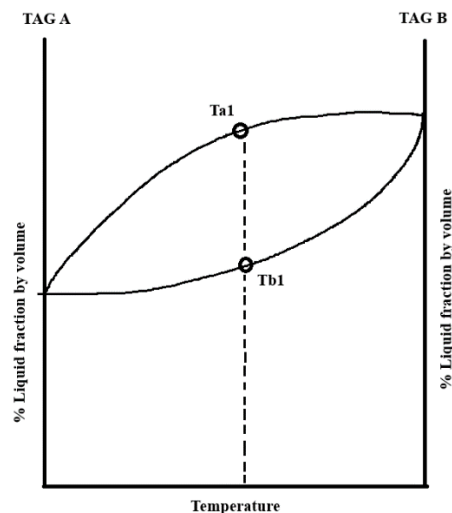

Figure 10: A graph that visualizes the relationship between two TAGs in a given temperature range, where the increasing amount of liquid-phase TAG acts as a solvent for the solid-phase TAGs present, leading to an overall increase in liquid-phase TAG by volume. Ta1 and Tb1 represents the respective percentages of liquid-phase for each TAG at a given temperature point.

In this example, TAG A is a TAG that has a lower melting range compared to TAG B, which leads to an increase in the liquid-phase as the temperature increases. Consequentially, the liquid-phase of TAG B will also increase eventually due to the increasing temperature, however a given amount of the solid-phase will also be able to dissolve in the liquid-phase of TAG A, as a result of the liquid-phase TAG A acting as a solvent. This inherent property of liquid-phase TAGs being able to act as solvents for the solid-phase leads to an increase in the total liquid-phase by volume, as a result of the solid-phase decreasing by dissolving in the liquid-phase. The amount which is able to be dissolved ultimately depends on the degree of saturation which the liquid-phase is able to undergo, the total amount of liquid-phase by volume, and the temperature of the solution.

2.6 – ω-6 and ω-3 fatty acids, and their glass transitions

ω-3 fatty acids are a group of FA's coined after the start of the first double bond in the acyl chain. As explained in section 2.1.2, FAs consist of a carboxyl group and an acyl chain. Unsaturated FA's also have double bonds at given points in the chain. ω-3 FA's double bonds begin on the n-3 point of the acyl chain, meaning the third carbon atom from the methyl end group (Breivik, 2007). Correspondingly, ω-6 FAs are named from the same logic, meaning that the double bonds start from the n-6 position. The amount of double bonds in the ω-6 and ω-3 FAs vary, but they generally contain between two to six double bonds, making them polyunsaturated fatty acids (PUFA's). Figure 11 shows the structure of the ω-3 FA's *α-linolenic, eicosapentaenoic* (EPA) and *docosahexaenoic* (DHA) acids. Fatty fish species, like *Salmo salar* are a rich source of ω-6 and ω-3 FA's, and particularly the ω-3 FAs EPA and DHA (Bou Mira, 2016). EPA and DHA are of particular interest to the pharmaceutical industry due to their well-documented health benefits (Swanson et al., 2012).
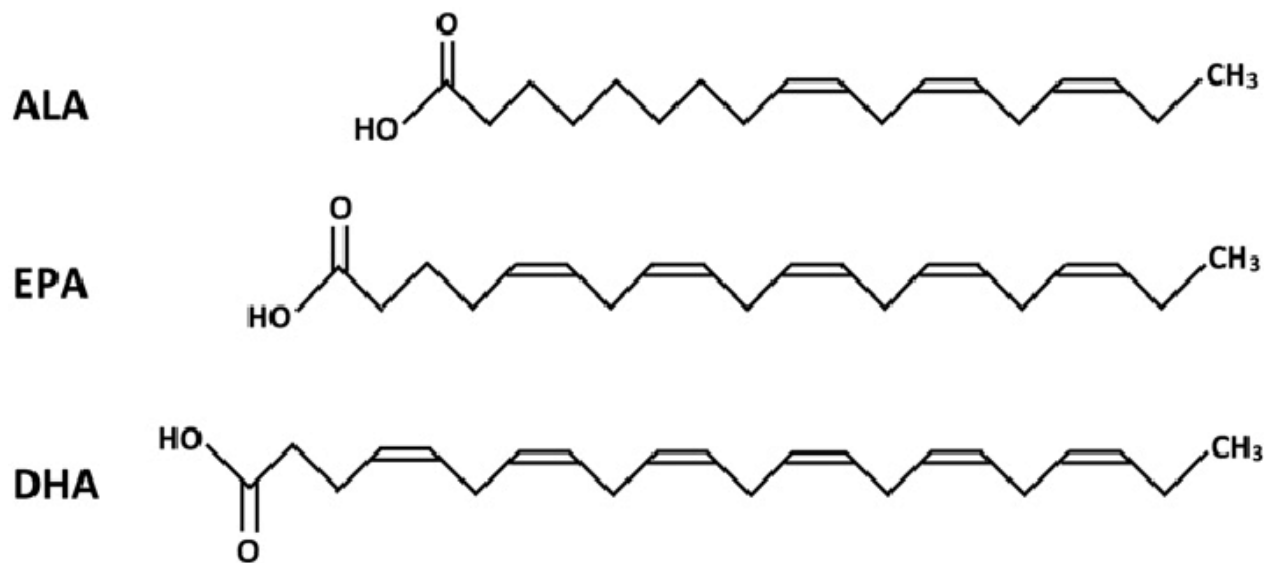
Figure 11: The structure of the ω-3 fatty acids, α-linolenic (ALA), eicosapentaenoic (EPA) and docosahexaenoic (DHA) acids. Notice the start of the double bonds from the n-3 position, respective of the methyl end group (Devassy et al., 2016).

Looking away from a nutritional standpoint, several of the FAs in the ω-6 and ω-3 groups also exhibit an interesting property when subjected to cooling aimed towards phase-transitions. Specifically, when certain FAs are present in TAGs, mixed or otherwise pure, and are subject to cooling that would normally lead to crystallization (i.e. a phase transition from a liquid to a solid phase), they instead form an amorphous substance that lack the normal degree of order that most crystalline substances exhibit (Dyre, 2006). The term "glass transition" is coined from the substance glass, which is a non-crystalline substance that exhibits amorphous qualities, much like the ω-6 and ω-3 FAs that are the subject of this section. Interestingly, in fish species it may also be observed that a TAG mixture from the respective fish may go through several glass transitions depending on the temperature (Tolstorebrov, 2014). This can also be seen in Table 1, where certain TAGs have several temperatures at which a glass transition can be observed. For example, tuna meat exhibits an initial glass transition at -21,0°C and a secondary glass transition at -72,0°C. As mentioned, the glass transition of ω-6 and ω-3 FAs may be observed both in mixed and pure TAGs. Table 1 shows the glass transition temperature in some mixed TAGs, while Table 3 shows the glass transition in some pure TAGs.

Table 3: An overview of pure TAGs with their corresponding fatty acid, the abbreviation, and the onset, inflection, and end of the glass transition which is exhibited for the respective TAG (Tolstorebrov, 2014).

Nomenclature	Fatty acid	Abbreviation	Onset °C	Inflection °C	End °C
Trieicosapentaenoin;1,2,3-tri-(5Z,8Z,11Z,14Z,17Z-icosapentaenoyl)-sn-glycerol	C20:5ω(5c,8c,11c,14c,17c)	EPA (3x)	-113,89	-111,78	-109,5
Tridocosahexaenoin;1,2,3-tri-(4Z,7Z,10Z,13Z,16Z,19Z-docosahexaenoyl)-sn-glycerol	C22:6ω(4c,7c,10c,13c,16c,19c)	DHA (3x)	-113,04	-110,39	-108,7
Trigammalinolenin;1,2,3-tri-(6Z,9Z,12Z-octadecatrienoyl)-sn-glycerol	18:3ω(6c,9c,12c)	γLi (3x)	-111,85	-109,8	-108,22
Triarachidonin;1,2,3-tri-(5Z,8Z,11Z,14Z-icosatetraenoyl)-sn-glycerol	20:4ω(5c,8c,11c,14c)	AaAaAa	-110,38	-107,25	-105,59

The respective TAGs in Table 3 all have three different temperature points which are of interest. Figure 12 visualizes the temperature points during a glass transition of an arbitrary TAG, and the difference in heat flow between the two phases. These are the onset, inflection and the end points. The onset point is the given temperature at which a TAG starts to undergo the glass transition, wherein the liquid TAGs exhibit both thermodynamic and viscoelastic changes. Of particular interest is the change in heat flow which marks the phase-change between liquid to glass. The inflection point marks the point in which the heat flow coefficient is at its highest. The end point is where the glass transition has been completed and the phase-change is done. After the given TAG has undergone glass transition, the viscosity of the compound increases significantly, giving a rubbery and hard consistency.
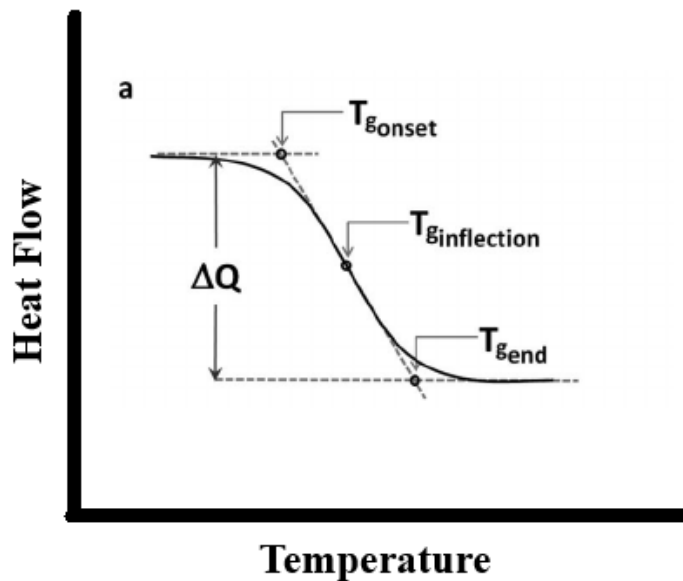
Figure 12: A graph visualizing the three points, onset, inflection and end, of the glass transition phenomenon. ΔQ describes the difference in heat flowing into the system pre-glass transition and post-glass transition. Adapted from (Abiad et al., 2014).

A significant consequence of the glass transition phenomenon is that when lipid solutions that contain the given TAGs that exhibit glass transition properties is exposed to very cold temperatures (<-30,0°C), a given fraction will always remain in a liquid-phase instead of crystallizing completely when subject to "normal" freezing temperatures (Tolstorebrov et al., 2014). The exception stands if a lipid solution is exposed to extreme freezing temperatures below <-111,0°C, which is where glass transitions for most fish oils occur. There is also the possibility that TAGs which exist in a crystalline solid-phase may dissolve in liquid-phase TAGs, and as such increase the total fraction of liquid-phase TAGs that are present in a given lipid solution. Aside from the practical implications this may have on storing stability, the need for adequate packaging and storing stability (Tolstorebrov, 2014), this also has implications on winterization of lipid solutions containing a high fraction of ω-6 and ω-3 fatty acids. Particularly, fish oil, which contains high amounts of the given fatty acids, are subject to these implications as a result of glass transition. Especially due to the low temperatures in which ω-6 and ω-3 fatty acids must be exposed to, the feasibility of concentration of these specific fractions with only dry fractioning is quite low. However, there have been studies exploring alternate winterization with use of solvents and low temperatures (-80,0°C) that have shown some success (Lei et al., 2016).

3. Materials and methods

During the course of this bachelor's thesis, winterization of BCr Algae oil from G.C Rieber has been conducted. Figure 13 shows a general overview of the project structure. During the course of the project, two methods of winterization were explored, namely shear-driven (henceforth called dynamic) and static winterization. The main difference between the two methods is dynamic winterization utilizing magnetic stirring during the crystallization phase. The general workflow of the sections included performing crystallization of the algae oil at a given temperature range, for example 20°C→15°C, analyzing the crystalline structures formed during crystallization, performing dry fractionation of the slurry that was formed, evaluating the filtering efficiency and then performing a chemical and thermodynamic analysis of the respective fractions.
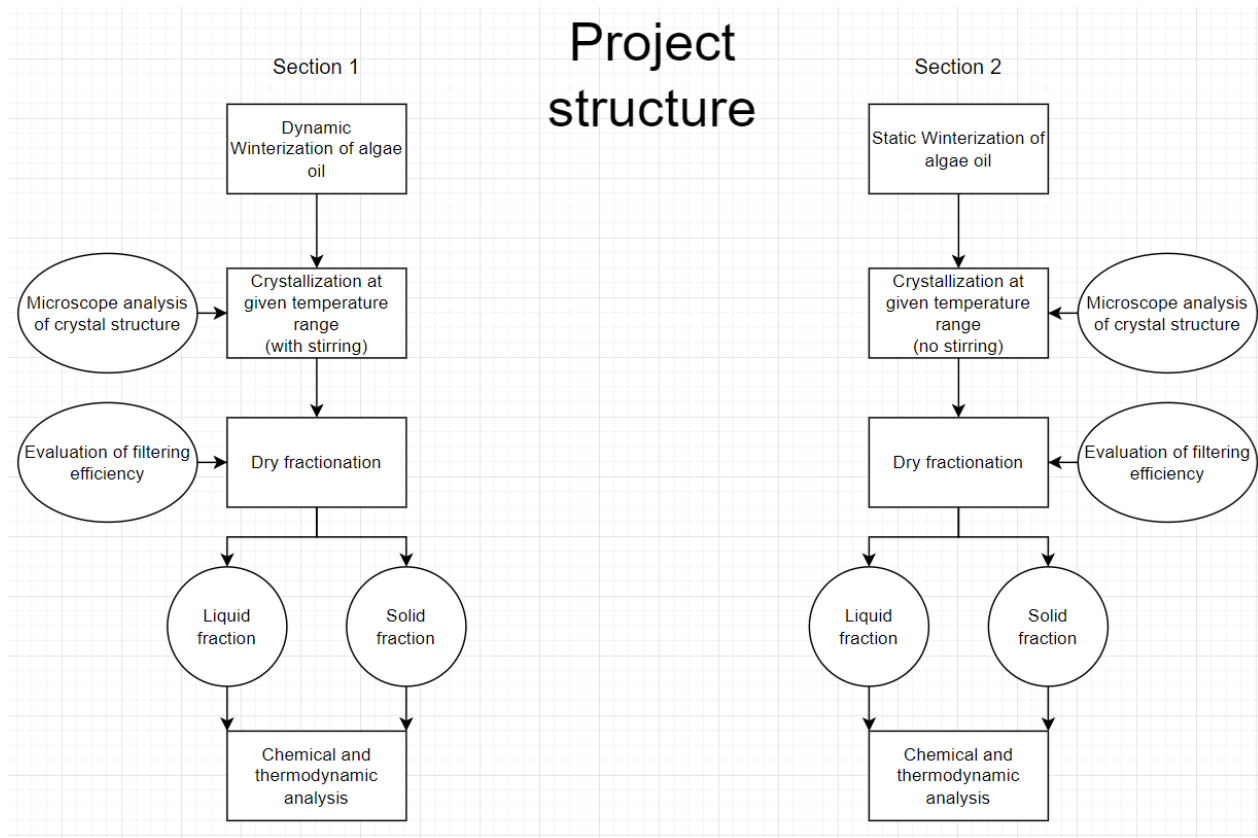

Figure 13: A flowchart describing the structure of the projects performed during the bachelor's thesis, with the respective sections and their workflow.

3.1 – Winterization of algae oil (BCr)

Algae oil of the brand DCR from G.C Rieber was used as the subject oil for winterization in both sections. Figure 14 shows the general workflow that was performed during winterization at a given temperature range.
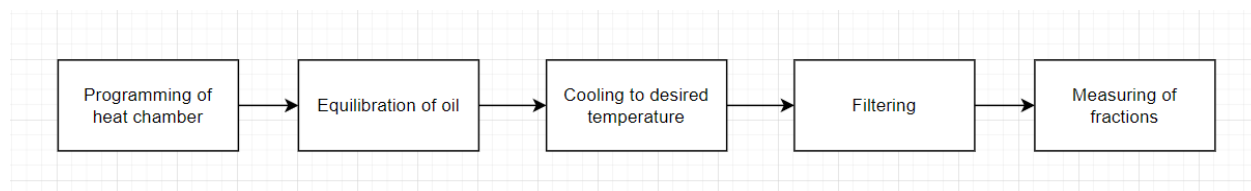

Figure 14: A flowchart of the workflow utilized while performing winterization at a given temperature range.

Prior to performing winterization at a given temperature range, a flask containing the oil was submerged in scalding water to allow for a less viscous product and to convert all crystalline structures to a liquid phase. For samples which were liquid at room temperature, tempering overnight in room temperature was instead performed. In the meantime, a Binder KMF 240-UL heat chamber was programmed to the desired temperature range. Table 4 shows an example of the programming that was utilized for the temperature range 50-20°C.

Table 4: A table describing the programming of the Binder KMF 240-UL heat chamber's program set up for the first fractioning. The ambient temperature in the laboratory is roughly ~23°C.

Stage	Description	Temperature (ºC)	Time (minutes)	Cooling rate
1	Equilibration	23°C → 50°C	60	-0.45°C/min
2	Cooling	50°C → 20°C	360	0.08°C/min
3	Equilibration	20°C	5400	0°C/min

After the oil was equilibrated and completely liquified, a sample was poured into a beaker, measured and inserted into the heat chamber. For the dynamic winterization section, an IKA RCT Basic magnetic stirrer was set to 50/rpm and utilized to expose the sample to shear while cooling. Figure 15 depicts the setup of equipment in the heat chamber. The sample was then cooled down to the desired temperature. Table 5 and Table 6 describes the cooling rates utilized for each temperature range for the dynamic and static winterization procedures respectively. The static winterization section initially used the same temperature ranges and cooling rates as for the dynamic section, however some temperature ranges did not yield crystallization, so alternative temperatures were used instead. Table 6 reflects this by mentioning if crystallization was

observed or not for each temperature range. Crystallization was observed for all the dynamic
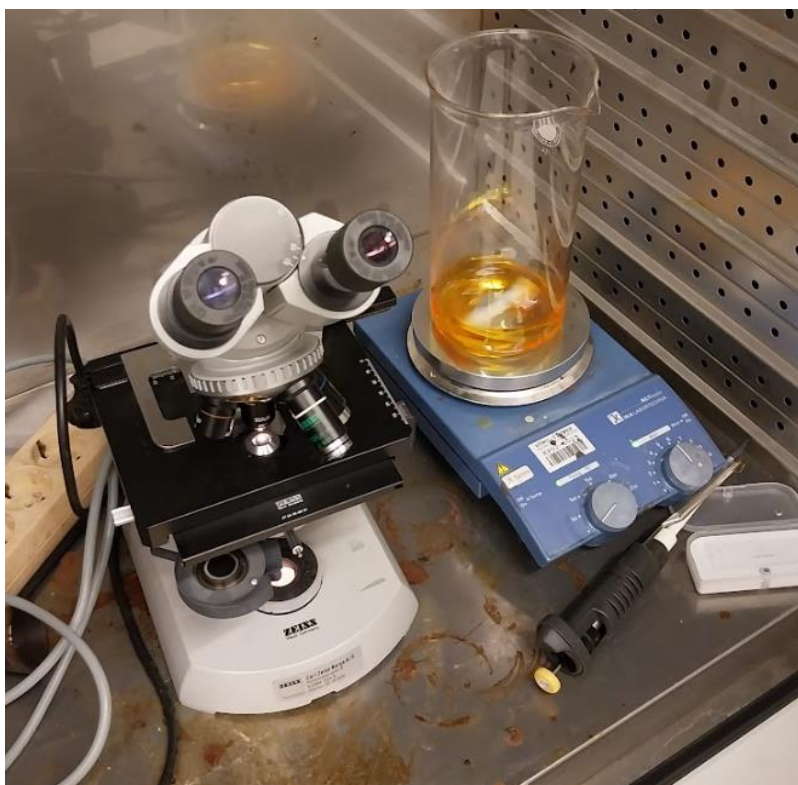
winterization temperature ranges.

Figure 15: A picture depicting the setup of the dynamic winterization in the heat chamber, with the Carl Zeiss compound microscope and IKA RCT Basic magnetic stirrer.

Table 5: A table describing the total time of cooling for each temperature range, and the respective cooling rate utilized for the dynamic winterization experiments.

Temperature range	Cooling time elapsed (minutes)	Cooling rate
50°C → 20°C	360	0.080°C/min
20°C → 15°C	240	0.020°C/min
15°C → 12°C	240	0.013°C/min
12°C → 10°C	180	0.011°C/min
10°C → 8°C	180	0.011°C/min

Temperature range	Cooling time elapsed (minutes)	Cooling rate	Crystallization observed?
50°C → 20°C	360	0.080°C/min	Yes
20°C → 15°C	240	0.020°C/min	Yes
15°C → 12°C	240	0.013°C/min	No
15°C → 10°C	240	0.020°C/min	Yes
10°C → 8°C	180	0.011°C/min	No
10°C → 6°C	240	0.016°C/min	No
10°C → 4°C	240	0.025°C/min	Yes

The sample was checked every hour until the desired temperature was reached, to check for crystallization. If crystallization was observed, a small sample would be taken with a pipette and analyzed with a Carl Zeiss compound microscope. These pictures were used as the basis for measuring crystal sizes and the types of crystals formed. These would later be noted in Microsoft Excel for statistical analysis. After the heat chamber had reached the desired temperature, the oil would be left overnight to equilibrate. The following day, a small sample would be taken with a pipette and analyzed with a Carl Zeiss compound microscope to observe the crystalline structures. Subsequently, a 500 mL Büchner flask was cleaned with absolute ethanol (99,8%) to remove impurities. A Büchner funnel was then inserted into the Büchner flask, and a blue ribbon (2µm retention) was placed on top. A tube was then connected to the spout and then connected to a vacuum pump. The slurry was then poured over the filter and the vacuum pump was turned on. Figure 16 depicts the setup of the Büchner flask, the Büchner filter and the pump tube. The filtration would then take place and continue until the slurry had completely drained of liquid. After filtration was done the respective fractions were weighed and samples were taken for analysis later. The total yield, distribution of liquid and solid fractions and loss during processing was found with equations 1-4. The fractions were then transferred to containers and put into a freezer. The liquid fraction obtained was then used as a basis for the next separation at the given temperature range.

Figure 16: A picture depicting the setup of the Büchner flask, the filter and the tube connecting to the vacuum pump. Notice the presence of the slurry in the Büchner filter and the liquid phase amassing in the bottom of the flask.

Equation 1

$$Yield = weight\ of\ solid\ fraction(g) + weight\ of\ liquid\ fraction(g)$$

Equation 2

$$\%\ Liquid\ fraction = \frac{weight\ of\ liquid(g)}{total\ yield(g)} * 100$$

Equation 3

$$\%\ Solid\ fraction = \frac{weight\ of\ solid(g)}{total\ yield(g)} * 100$$

Equation 4

$$Loss = \left(1 - \frac{yield(g)}{initial\ weight(g)}\right) * 100$$

3.2 – GC analysis of fatty acid composition

The analysis of the fatty acid composition was performed with gas chromatography (GC). Firstly, the samples obtained during the winterization experiments were prepared for GC analysis with the Bligh & Dyer method (NTNU, 2022). To do this, the solid fraction samples were transferred to small 1.5mL containers and placed in Stuart SBH130D/3 block heater with their tops open. The heat element of the block heater was turned to 65°C and N_2 gas was flushed over the samples to prevent oxidation of the lipids. After the samples were transformed to liquid, 250μL were transferred into 30cm^3 chloroform resistant sample tubes (PTFE). For the liquid fraction samples, 500μL were transferred into the sample tubes. Figure 17 depicts the setup used to prepare the samples for centrifugation. 3,0mL of deionized water was then added to each tube, along with 5,0mL of chloroform ($CHCl_3$) and 10,0mL of methanol (CH_3OH). The samples tubes were then placed in a tray of ice to prevent evaporation. One sample was then homogenized for 60 seconds at 12 000 rpm using a Polytron PT 3100 D homogenizer. 5,0mL more of chloroform ($CHCl_3$) was then added to the tube and homogenized again for 20 seconds. 5,0mL more of deionized water was then added to the tube and once again homogenized for 20 seconds. After one sample was prepared, the Polytron homogenizer was taken apart and washed thoroughly to prevent sample contamination. This process was then repeated for each sample until they were all prepared.
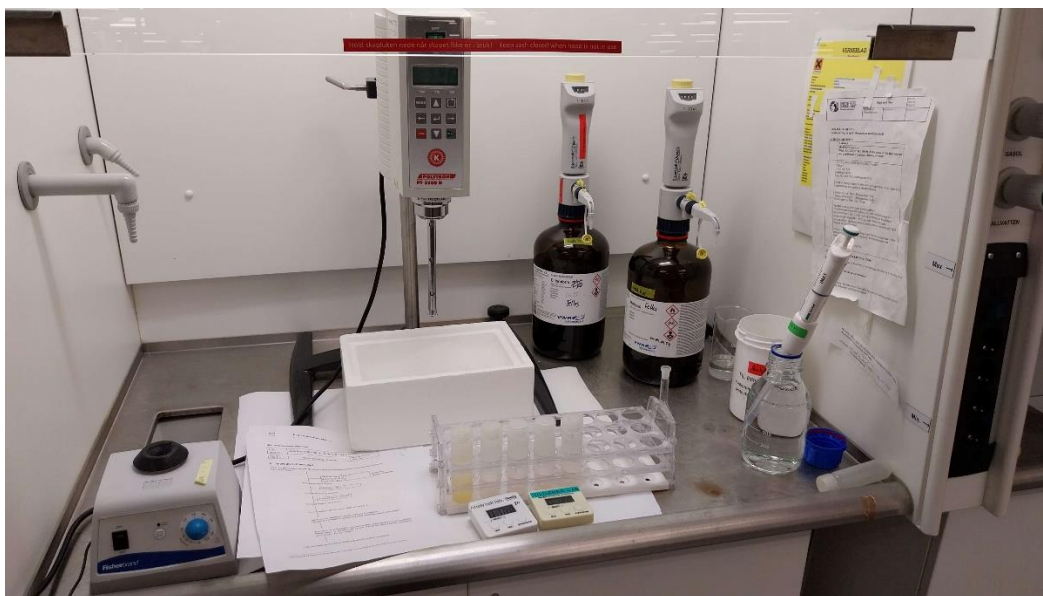

Figure 17: A picture depicting the setup and equipment used to prepare the lipid samples for GC, using the Bligh & Dyer method.

After the samples were homogenized, they were added to a Kubota 1700 centrifuge with cooling. The sample tubes were cooled down to 5°C, and centrifugated at 7000 rpm for 10 minutes. After the centrifugation was completed, the sample tubes were taken out and placed on racks. A glass Pasteur pipette with a Peleus balloon was then used to transfer the entirety of the bottom chloroform phase (see Figure 18) to chloroform resistant (PTFE) 15mL sample tubes. The samples tubes were then placed in a freezer for storage.
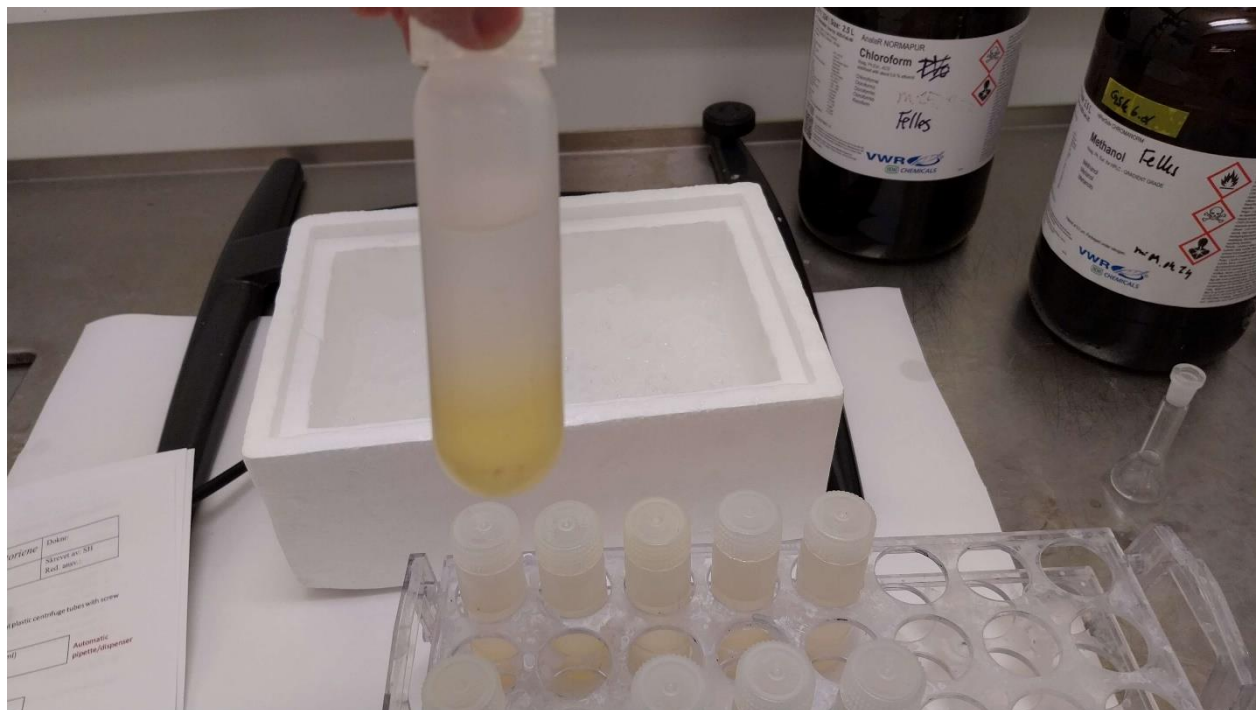

Figure 18: A picture depicting the two different phases that could be observed in the sample tubes. The translucent top phase is the non-polar water phase, while the bottom yellow phase is the chloroform phase with the lipids. The latter is the phase that was extracted from the tube.

The following day, the sample tubes were placed back on the block heater with their tops open. The temperature on the block heater was turned to 30°C, and N_2 gas was yet again flushed over the samples. This time the samples were kept for 2 hours to completely evaporate the chloroform phase, such that only the lipid phase remains. Figure 19 depicts the setup utilized for this. As the total liquid volume in the sample tubes decreased, the needles flushing the tubes with gas was lowered down until just above the surface of the liquid.
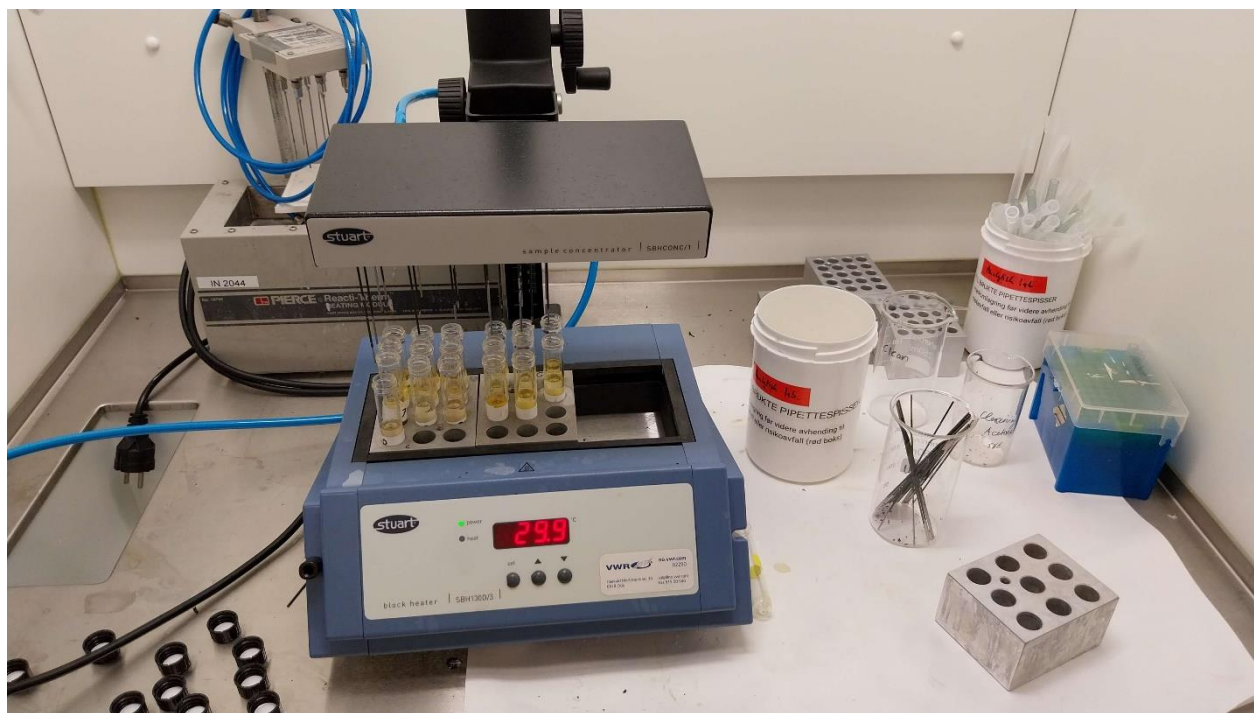
Figure 19: A picture depicting the setup used to evaporate the chloroform phase from the sample tubes containing the lipids. The sample concentrator above was lowered during the entirety of the process until a small amount of lipids remained.

Once the chloroform phase had been sufficiently evaporated, the lipid samples could now be converted to fatty acid methyl esters (FAME), such that GC analysis could be performed. To do this, 3mL of methanolic potassium hydroxide (KOH, 0.5M) was added to each sample tube, mixed and then put back on the block heater. The temperature was now turned up to 70°C, and the samples were left for 20 minutes. After 20 minutes had passed, the samples were transferred to a container containing ice to let them cool down. After this, 5mL of boron trifluoride-methanol (0.859g/mL) solution was added to each sample and then placed back on the block heater. This time they were left for 5 minutes. After 5 minutes had passed, the samples were placed back in ice to cool down. To each sample tube, 2mL of n-butylacetate was added and subsequently mixed with a vortex-mixer. After this was done, saturated NaCl liquid could be added to each sample tube up until approximately 1 cm away from the top of the sample tube's rim. One small scoop of anhydrous sodium sulphate was then added to each sample tube. This was then left for 5 minutes to allow for the organic phase to rise to the top of the tube. To allow for an easier extraction, 200μL of hexane was added to the organic phase. After this was done, the organic phase was transferred to a GC-vial using a glass pipette and Peleus balloon.

Figure 20: A picture depicting the GC instrument used for analysis of the FAME samples. The depicted GC instrument is an Agilent Technologies 6850 GC networking system.

With the lipids now converted to FAME's, GC analysis could now be performed. For this, an Agilent Technologies 6850 GC networking system was utilized, as depicted in Figure 20. The commercial fatty acid standard "Advanced FAME Supelco 37" with common fatty acids was utilized as the comparing standard. All the samples were inserted into the autosampler system, and analysis was started and left overnight. The following day when the analysis had been performed, the GC graphs could be analyzed and compared to the fatty acid standard provided. To do this, the retention time (rT) for each fatty acid in the standard was determined and compared against the rT's observed in the analyzed samples. The software utilized allowed for showing the area of each peak in the graph, and subsequently calculated the total concentration of each fatty acid. This was done for all the analyzed samples. Appendix 11 and 12 shows the fatty acid standard with all fatty acids identified, and the same fatty acid standard which was run alongside the FAME samples respectively. Appendix 13-31 shows all the GC graphs obtained from the samples.

3.3 – DSC analysis of thermodynamic properties

To perform differential scanning calorimetry analysis of the fractions, a Texas Instruments Q2000 DSC was utilized with a liquid nitrogen cooling system. Three samples were analyzed at a time due to the liquid nitrogen vat only holding enough for three samples at a given time. To prepare the samples, they were submerged in hot water (>60°C) to ensure a homogenous state. Meanwhile, TZero aluminum pans were weighed, and their weight was noted down with a three-decimal accuracy. After the samples had converted to a liquid phase, a micro-pipette was used to transfer 1 small droplet into a TZero aluminum pan. These pans were then hermetically sealed with a TZero DSC sample encapsulation press. The TZero aluminum pans were then weighed again, and their new weight noted down. The samples were then placed into the Q2000, along with an empty reference TZero aluminum pan. The aluminum pan weight and the sample weight was then noted in the software and a program was constructed for each sample. Table 7 depicts an example program utilized to analyze the liquid 15°C→12°C fraction. The program was then left to run overnight and analyze the samples. The following day, new samples would be prepared and the results of the previous were analyzed in TA Universal Analysis. This was then repeated until all desired samples were analyzed. Figure 21 depicts the setup used for analyzing the thermodynamic properties of the fractions, with the DSC instrument and the encapsulation press used for preparing the TZero aluminum pans. After the respective samples were finished with their cycles in the DSC, TA Universal Analysis software was used to view the resulting DSC graphs. Each temperature range could then be compared with their respective fractions.

Table 7: A table depicting an example program utilized for the Q2000 DSC to analyze a fraction sample for its thermodynamic properties. This program was used to analyze the liquid 15°C→12°C fraction.

Operation	Temperature
Equilibrate	Room temperature → 20.00°C
Isothermal for 5 minutes	20.00°C
Cooling (0.500°C/min)	20.00°C → -40.00°C
Equilibrate	-40.00°C
Isothermal for 5 minutes (End of cycle 1)	-40.00°C
Cooling (10.00°C/min)	-40.00°C → -150.00°C
Equilibrate	-150.00°C
Isothermal for 5 minutes (End of cycle 2)	-150.00°C
Heating (10.00°C/min) (End of cycle 3)	-150.00°C → 20.00°C

Figure 21: A picture depicting the Q2000 DSC instrument, TZero aluminum pans, and the TZero DSC Sample Encapsulation press used to secure the pans with the sample inside.

4. Results

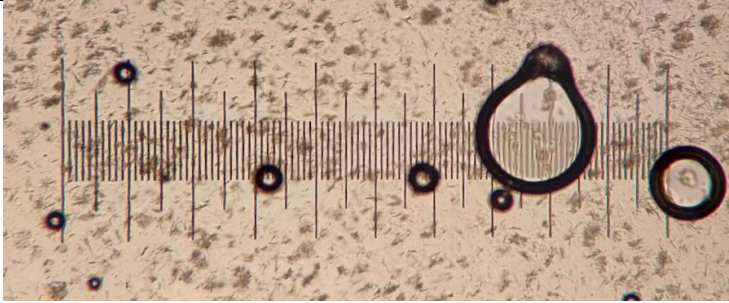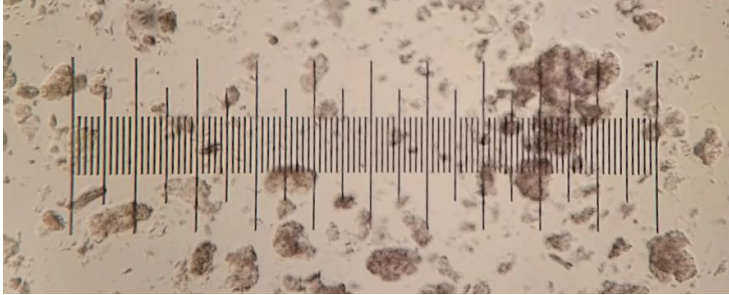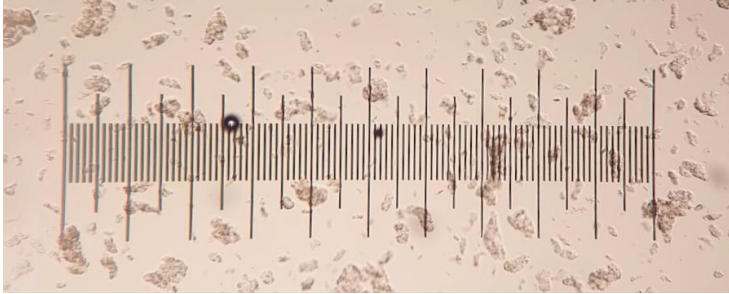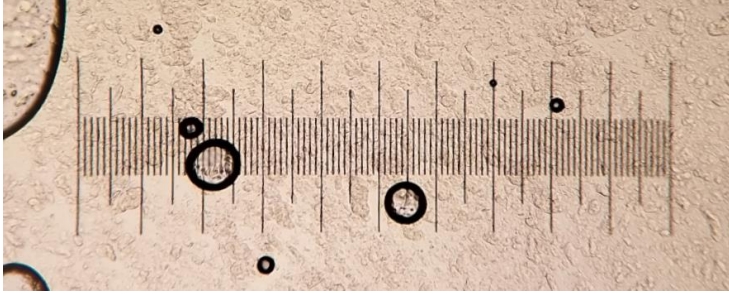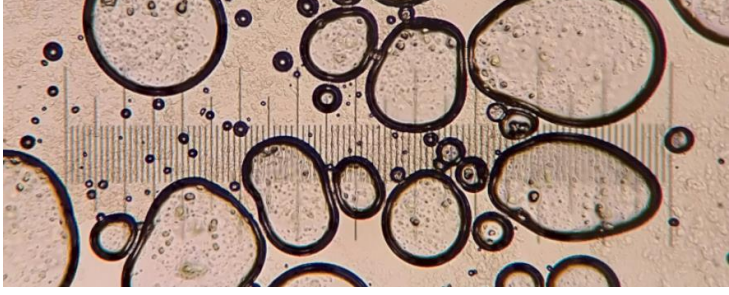## 4.1 – Dynamic winterization of algae oil (BCr)

The results of dynamic winterization of G.C Rieber BCr algae oil for each respective temperature range can be found in Table 8. The table describes the initial weight of the liquid phase prior to the respective winterization, total yield, yield of the respective liquid and solid fractions, loss during processing and elapsed time of filtering.

Table 8: An overview of the different temperature ranges utilized during dynamic winterization, the weight of the initial liquid phase prior to winterization, the total yield after filtering, loss during processing and the yield of the respective phases. Equations (1-4) were used to calculate the respective parameters.

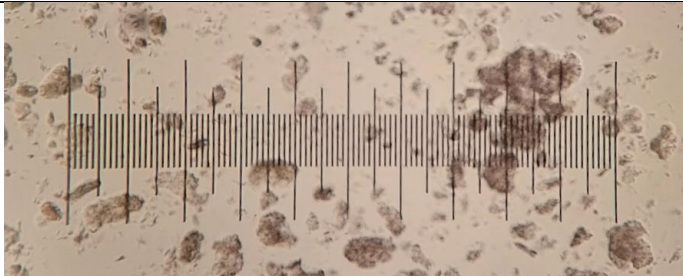| Temperature range	50°C → 20°C	20°C → 15°C	15°C → 12°C	12°C → 10°C	10°C → 8°C
Initial weight of liquid phase	302,12g	224,74g	78,98g	60,05g	37,93g
Total yield	284,61g	169,42g	65,02g	45,21g	26,97g
Loss during processing	5.8%	24.6%	12.7%	25.7%	28.9%
Liquid phase yield	228,09g (80.1%)	82,49g (48.7%)	62,30g (95.8%)	40,84g (90.3%)	26,69g (98.9%)
Solid phase yield	56,52g (18.9%)	86,93g (51.3%)	2,72g (4.2%)	4,37g (9.7%)	0,28g (1.1%)
Elapsed time for filtering (minutes)	95	200	60	150	60
Equilibration time (hours)	20	18	20	22	23

Table 9 depicts pictures of all the crystalline structures observed during the dynamic winterization process, from high to low temperature range. Each picture depicts the structures observed after tempering at the respective temperature overnight. Note temperature range 10°C → 8°C which has several large air bubbles, caused by air being mixed in with the solution during crystallization. This was an unintentional side effect of the low amount of liquid-phase.

Table 9: An overview of all the crystalline structures observed during dynamic winterization, with their respective temperature ranges listed.

Temperature range	Crystal structures
50°C → 20°C	
20°C → 15°C	
15°C → 12°C	
12°C → 10°C	
10°C → 8°C	

For the temperature ranges 50°C → 20°C and 20°C → 15°C crystallization was also observed on day 1, prior to the day 2 pictures which make up the entirety of Table 9. Table 10 depicts the crystalline structures observed on day 1 and 2, for the temperature ranges 50°C → 20°C and 20°C→ 15°C respectively, compared side by side to each other to visualize the progression of crystallization overnight.

Table 10: A table depicting the crystalline structures formed during dynamic winterization on day 1 and day 2 for the temperature ranges 50°C → 20°C and 20°C → 15°C respectively, comparing them side by side.

Temperature range	Day 1	Day 2
50°C → 20°C		
20°C → 15°C		

The diameter and types of crystals observed for dynamic winterization are depicted in Table 11. Each temperature range and the respective average crystal diameter, median and standard deviation is noted. Additionally, the largest and smallest crystal sizes for each range is also noted. The results are taken from the excel sheet in appendix 1.

Table 11: An overview of the crystal diameters observed, the median, standard deviation, largest and smallest crystals observed, and the type of crystals observed for each respective temperature range during dynamic winterization. Values taken from excel sheet in appendix 1. Observed crystal types is derived from figure 9.

Temperature range	50°C → 20°C	20°C → 15°C	15°C → 12°C	12°C → 10°C	10°C → 8°C
Average crystal diameter (μm)	19,2	64,2	36,1	14,7	14,0
Median (μm)	20	55	30	10	10
Standard deviation (μm)	12,3	38,0	24,1	10,1	9,0
Largest size observed	40	180	100	40	35
Smallest size observed	5	20	5	5	5
Crystal types observed	Needles and some spherulites	Medium aggregates and needles	Medium aggregates	Needles	Needles

The measured crystal sizes were also analyzed statistically to give an idea of their distribution, through a histogram. Table 12 depicts the histogram for each respective temperature range obtained during dynamic winterization.
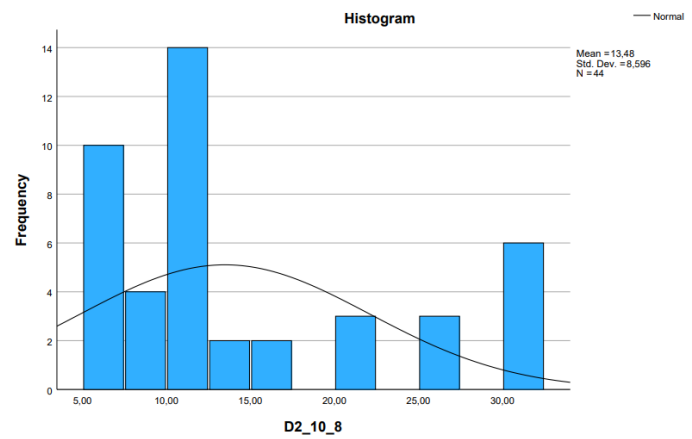
Table 12: A table depicting the histograms for each temperature range in dynamic winterization, using values from appendix 1, The x-axis represents the crystal diameter in μm, and the y-axis frequency of the respective size.

Temperature range	Histogram
50°C → 20°C	
20°C → 15°C	
15°C → 12°C	
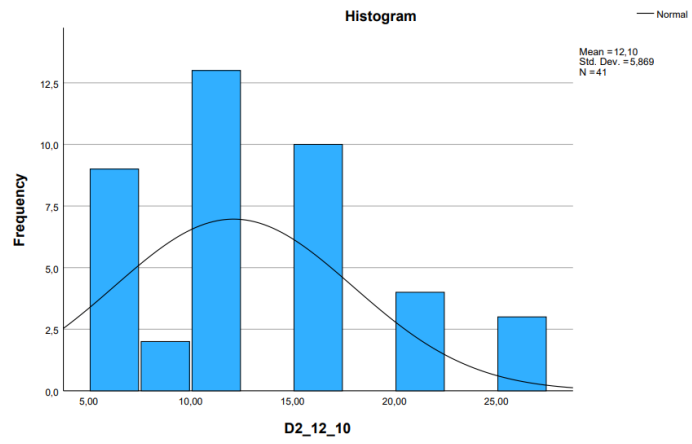
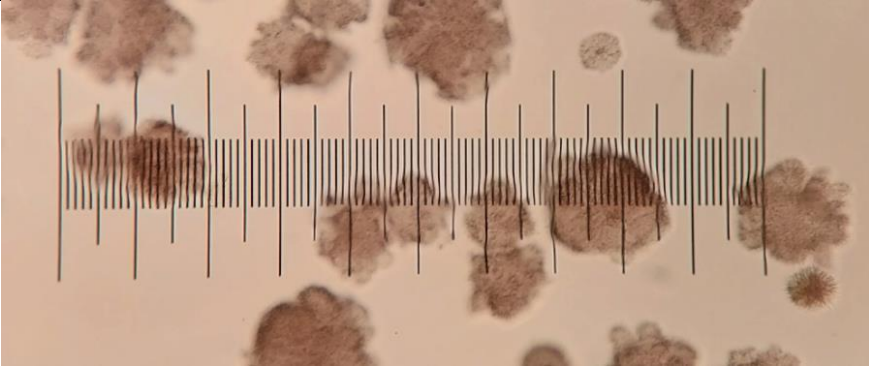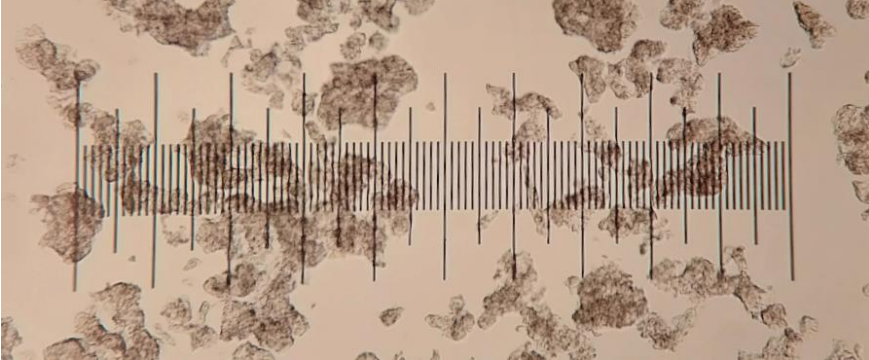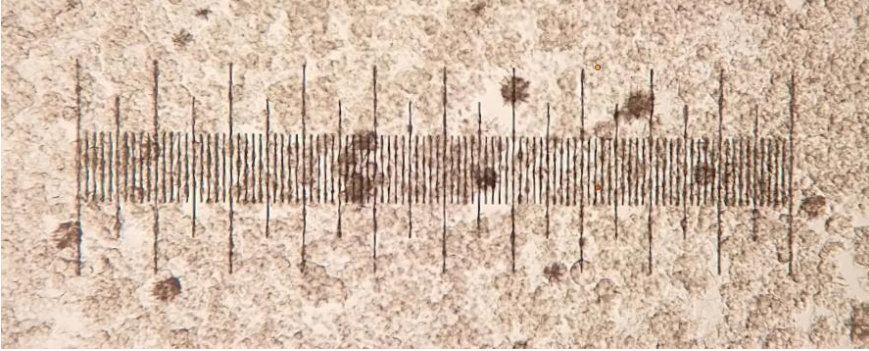| 12°C → 10°C	
10°C → 8°C	

4.2 – Static winterization of algae oil (BCr)
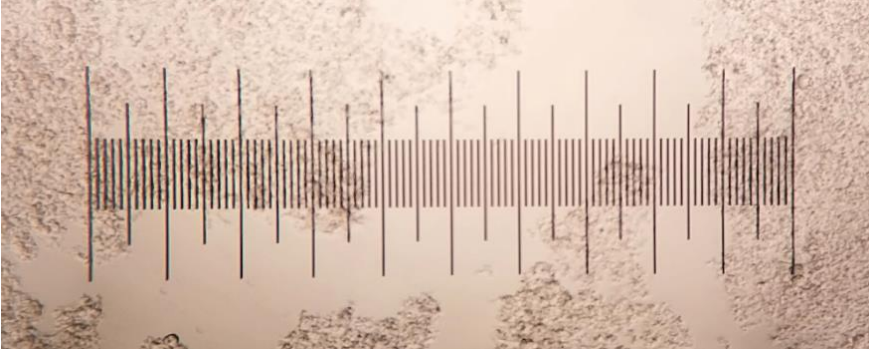
The results of static winterization of G.C Rieber BCr algae oil for each respective temperature range can be found in Table 13. The table describes the initial weight of the liquid phase prior to the respective winterization, total yield, yield of the respective liquid and solid fractions, loss during processing and elapsed time of filtering.

Table 13: An overview of the different temperature ranges utilized during static winterization, the weight of the initial liquid phase prior to winterization, the total yield after filtering, loss during processing and the yield of the respective phases. Equations (1-4) were used to calculate the respective parameters.

Temperature range	50°C → 20°C	20°C → 15°C	15°C → 10°C	10°C → 4°C
Initial weight of liquid phase	302,56g	188,21g	86,18g	46,73g
Total yield	287,24g	167,85g	73,39g	28,62g
Loss during processing	5.1%	11.2%	14.8%	38.8%
Liquid phase yield	192,20g (66.9%)	92,62g (55.2%)	54,29g (73.9%)	22,03g (77.0%)
Solid phase yield	95,04g (33.1%)	75,23g (44.8%)	19,12g (26.1%)	6,79g (23.0%)
Elapsed time for filtering (minutes)	60	145	60	90
Equilibration time (hours)	22	20	24	22

Table 14 depicts pictures of all the crystalline structures observed during the dynamic winterization process, from high to low temperature range. Each picture depicts the structures observed after tempering at the respective temperature overnight.

Table 14: An overview of all the crystalline structures observed during static winterization, with their respective temperature ranges listed.

Temperature range	Crystal structures
50°C → 20°C	
20°C → 15°C	
15°C → 10°C	
10°C → 4°C	

For the temperature ranges 50°C → 20°C and 20°C → 15°C crystallization was also observed on day 1, prior to the day 2 pictures which make up the entirety of Table 14. Table 15 depicts the crystalline structures observed on day 1 and 2, for the temperature ranges 50°C → 20°C and 20°C → 15°C respectively, compared side by side to each other to visualize the progression of crystallization overnight.

Table 15: A table depicting the crystalline structures formed during static winterization on day 1 and day 2 for the temperature ranges 50°C → 20°C and 20°C → 15°C respectively, comparing them side by side.

Temperature range	Day 1	Day 2
50°C → 20°C		
20°C → 15°C		

The diameter and types of crystals observed are depicted in Table 16. Each temperature range and the respective average crystal diameter, median and standard deviation is noted. Additionally, the largest and smallest crystal sizes for each range is also noted. The results are taken from the excel sheet in appendix 1.

Table 16: An overview of the crystal diameters observed, the median, standard deviation, largest and smallest crystals observed, and the type of crystals observed for each respective temperature range under static winterization. Values taken from excel sheet in appendix 1. Observed crystal types is derived from figure 9.

Temperature range	50°C → 20°C	20°C → 15°C	15°C → 10°C	10°C → 4°C
Average crystal diameter (μm)	116,3	88,2	20,4	12,1
Median (μm)	125	90	20	10
Standard deviation (μm)	48,1	58,0	10,6	4,7
Largest size observed	200	310	50	25
Smallest size observed	40	5	5	5
Crystal types observed	Medium/Large aggregates	Medium/Small aggregates	Needles and spherulites	Needles

The measured crystal sizes were also analyzed statistically to give an idea of their distribution, through a histogram. Table 17 depicts the histogram for each respective temperature range obtained during static winterization.

Table 17: A table depicting the histograms for each temperature range in static winterization, using values from appendix 1. The x-axis represents the crystal diameter in μm, and the y-axis frequency of the respective size.

Temperature range	Histogram
50°C → 20°C	
20°C → 15°C	
15°C → 10°C	
10°C → 4°C	

The solid phase yields for dynamic and static winterization is visualized in Figure 22, which depicts the respective solid yield for each temperature range compared to the total solid yield over all temperature ranges. Additionally, for static winterization, some temperature ranges did not yield crystallization which is reflected in the graph.
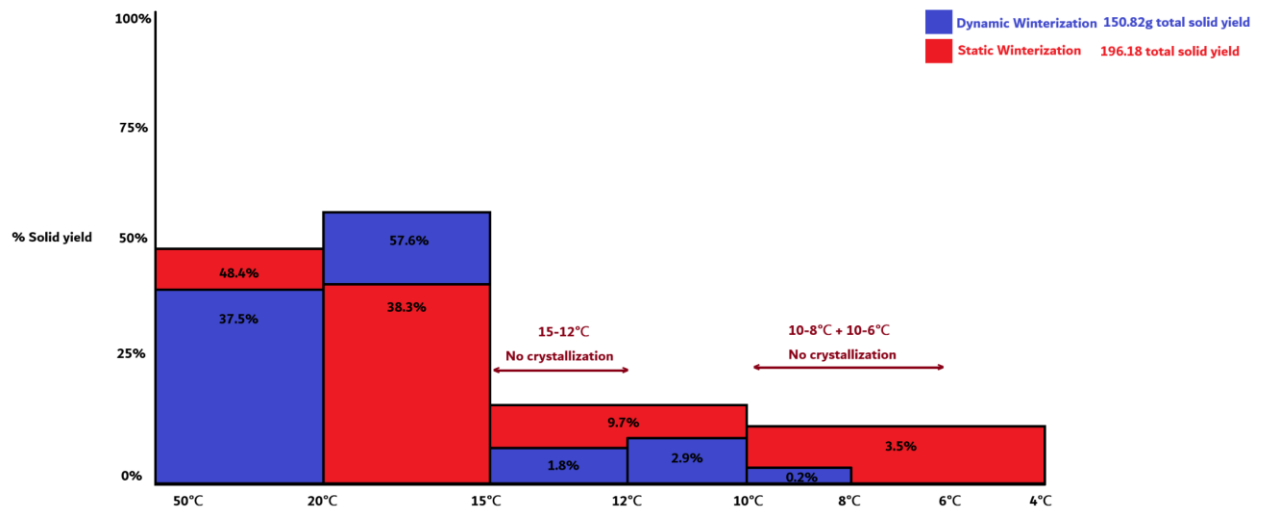

Figure 22: A graph comparing the solid phase yields between dynamic and static winterization, for each respective temperature range. The x-axis represents the temperature ranges, expressed in a sinking order, and the y-axis represents the percentage of solid-phase yield from the total amount denoted in the top right corner.

4.4 – Fatty acid composition

The fatty acid composition of all separated fractions were analyzed with the use of GC, against a commercial fatty acid standard which was run at the same time. The results of the fatty acid composition for dynamic and static winterization can be found in Table 18 and Table 19.

Table 18: A table depicting the fatty acids observed, and their respective percentages, for all fractions generated during dynamic winterization. The letters S and F stand for Solid and Liquid fractions respectively.

Temperature range and fraction	S 50-20	S 20-15	S 15-12	S 12-10	S 10-8	L 50-20	L 20-15	L 15-12	L 12-10	L 10-8
C14:0	3.63%	5.01%	4.97%	5.36%	6.19%	2.83%	2.98%	3.01%	3.54%	3.86%
C15:0	1.97%	2.50%	2.51%	2.66%	2.67%	3.48%	1.69%	2.00%	2.14%	2.40%
C16:0	45.22%	39.57%	39.21%	36.39%	36.66%	59.87%	46.85%	53.78%	52.23%	48.52%
C17:0	0.70%	0.80%	0.82%	0.84%	0.85%	0.97%	0.57%	0.73%	<0.1%	<0.1%
C18:0	0.80%	0.97%	0.97%	1.24%	1.08%	1.09%	0.55%	0.66%	0.93%	1.20%
C20:3	0.70%	0.81%	0.83%	0.91%	0.94%	0.70%	0.53%	0.47%	0.43%	0.56%
C20:5	0.50%	0.59%	0.57%	0.67%	0.69%	0.53%	0.39%	0.33%	0.30%	0.45%
C23:0	6.86%	6.89%	7.02%	7.29%	7.32%	3.93%	6.00%	5.90%	6.08%	6.41%
C24:0 / C24:1 /C22:6	39.64%	42.87%	43.10%	43.73%	43.44%	23.12%	35.05%	33.95%	34.33%	35.62%
Others	<0.1%	<0.1%	<0.1%	0.93%	0.96%	1.35%	5.55%	<0.1%	0.86%	1.76%

Table 19: A table depicting the fatty acids observed, and their respective percentages, for all fractions generated during static winterization. The letters S and F stand for Solid and Liquid fractions respectively.

Temperature range and fraction	S 50-20	S 20-15	S 15-10	S 10-4	F 50-20	F 20-15	F 15-10	F 10-4
C14:0	4.89%	2.72%	3.73%	<0.1%	3.86%	5.24%	5.75%	6.25%
C15:0	2.73%	1.66%	2.35%	<0.1%	2.01%	2.64%	2.75%	2.80%
C16:0	48.88%	51.09%	46.55%	1.02%	39.40%	37.30%	33.44%	31.09%
C17:0	0.93%	0.58%	0.90%	<0.1%	<0.1%	<0.1%	<0.1%	0.82%
C18:0	1.07%	0.55%	1.03%	<0.1%	0.69%	1.04%	1.16%	1.03%
C20:3	0.57%	0.51%	0.65%	<0.1%	0.64%	0.90%	1.09%	1.19%
C20:5	0.42%	0.38%	0.48%	<0.1%	0.51%	0.72%	0.77%	0.86%
C23:0	5.71%	6.06%	6.64%	<0.1%	5.83%	7.10%	7.80%	7.86%
C24:0 / C24:1 /C22:6	31.67%	34.93%	37.68%	0.97%	34.59%	41.70%	44.84%	45.74%
Others	3.56%	1.53%	<0.1%	92.72%	12.47%	3.38%	2.39%	2.36%

4.5 – Thermodynamic properties (DSC)

For the analysis of thermodynamic properties, the temperature ranges analyzed is described in Table 20. Each temperature range has its respective DSC graph. Each graph has a respective number of transitions from left to right, with the temperature in the heat flow minimum point marked. The respective transitions also have a phase transition onset ($T_{g\ onset}$) and phase transition end ($T_{g\ end}$) temperature marked, with its corresponding heat of fusion (ΔH_{fus}) in J/g.

Table 20: An overview of the DSC graphs generated by TA Universal Analysis for the respective winterization fractions. The winterization method is listed in the left row, with each column depicting a solid or liquid fraction and its respective DSC graph. The x-axis represents temperature, while the y-axis represents the heat flow (Q) difference between the sample and reference.

Winterization and temperature range	Liquid fraction	Solid fraction
Dynamic 50°C → 20°C		

Dynamic 20℃ → 15℃	
Dynamic 15℃ → 12℃	
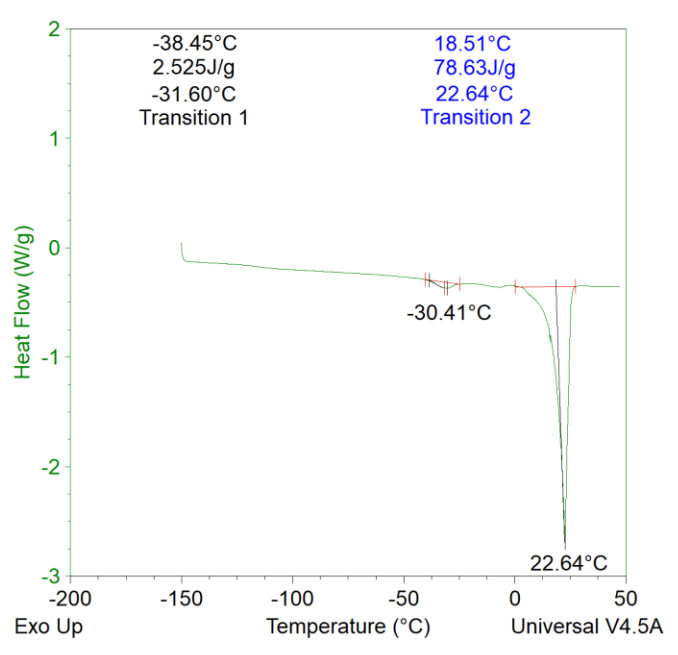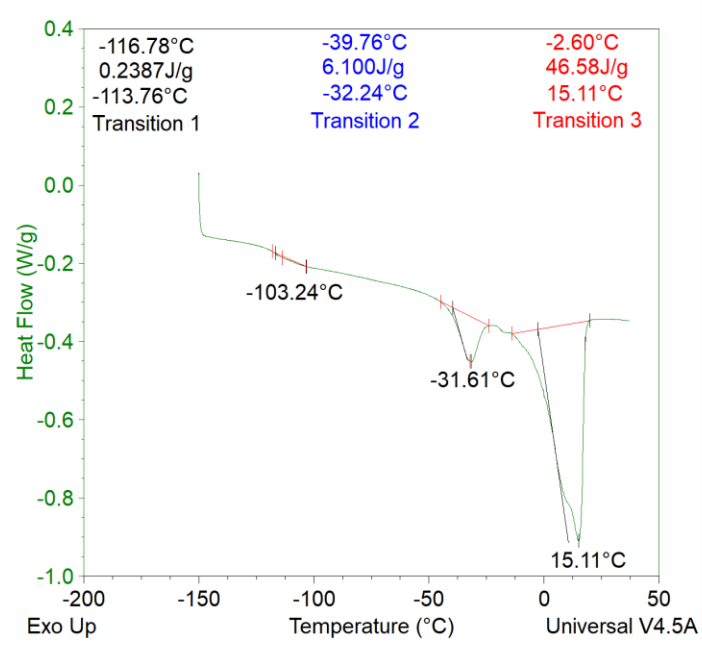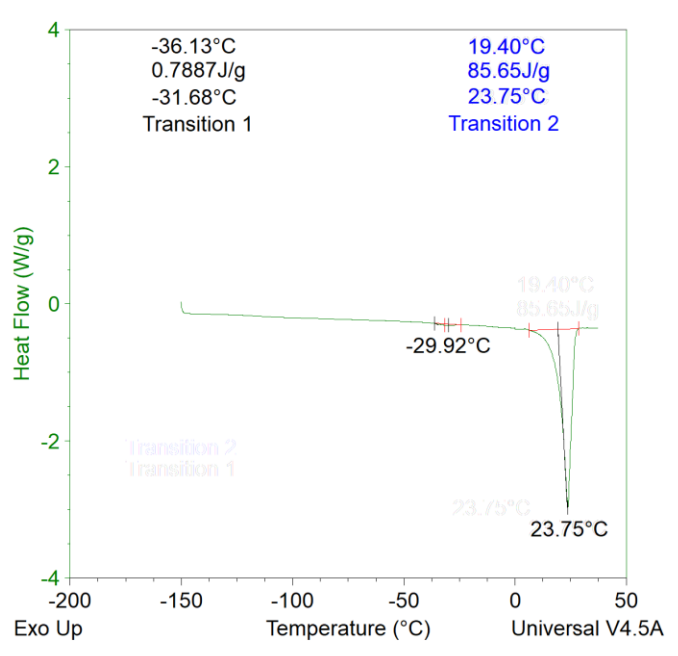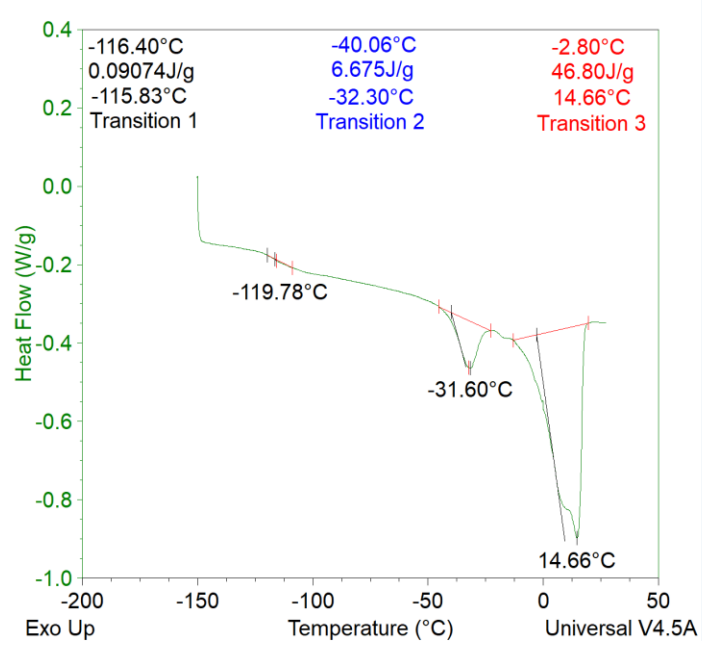
5. Discussion

5.1 – Crystal dimensions and network formation

During the dynamic winterization there were a total of 5 temperature ranges which was utilized for separation of fractions (see Table 8). Due to the presence of different TAGs in the differing fractions, as a result of the different crystallization temperatures, several distinct crystal structures, dimensions and types can be observed (see Table 10) Interestingly, it seems that the temperature ranges 20°C → 15°C and 15°C → 12°C yielded the largest crystals in terms of diameter, averaging at $64{,}2 \pm 38{,}0\mu m$ and $36{,}1 \pm 24{,}1\mu m$ respectively. These ranges also had the highest degrees of aggregation when compared to the other temperature ranges. This may be due to the fact that these ranges seemed to largely form spherulites exclusively, which seems to promote aggregation and network formation. Network formation is especially prevalent in the 20°C → 15°C fraction, where larger aggregates are seen forming networks together. It is also interesting to note that in day 1 and day 2 comparisons (see Table 10 and Table 15) that larger aggregates have already seemed to form shortly after crystallization, and these aggregates appear to form larger networks the following day. This may be an effect of Ostwald ripening, wherein the larger crystal structures grow bigger as dissolved crystals deposit on top of them, ultimately increasing their size. Though, the phenomenon where larger networks are formed from aggregates growing together may be due to sintering, which connects several aggregates together. Interestingly, we can also observe smaller crystal structures such as needles and spherulites on day 2 which are separated from larger networks, which seems to suggest a degree of crystallization that is independent of larger structures, throughout the slurry, being promoted overnight. This may be due to crystals which were initially in an unstable polymorphic configuration undergoing transitions to more stable forms in the liquid, and as such, forming new nuclei in the surrounding solution.

The ranges 50°C → 20°C, 12°C → 10°C and 10°C → 8°C for dynamic winterization seems to form smaller needles and spherulites exclusively. These fractions also expectingly had the smallest crystal diameters as a result of this. For the 50°C → 20°C in dynamic winterization the solution is exerted to a high rate of cooling (0.080°C/min), which may promote the formation of smaller crystals. This is due to a higher degree of homogenous crystallization throughout the liquid, which promotes crystal growth where crystals interdict each other in formation, ultimately

preventing the formation of larger crystal structures. This is also reinforced by the appearance of a very homogenous field of crystals as seen in Table 9. No large structures are observed, which seems to reinforce this assumption. However, the temperature ranges 15°C→12°C and 12°C→10°C suggest otherwise. These fractions had a lower rate of cooling, as seen in Table 5 (0.011°C/min), but still showed very small crystal sizes (14,7 ± 10,1μm and 14,0 ± 10,0μm respectively). This can also be observed in Table 8 for the respective ranges. It is however important to note that cooling rate alone is not the deciding factor on crystal growth and the resulting morphologies, size and network formation. A possible explanation to this phenomenon may be due to the fact that both of these temperature ranges present a smaller total amount of TAGs in the crystalline phases, and these TAGs crystallize in such a way that they prevent the formation of larger structures. In general, however, the occurrence of generally smaller crystal diameters throughout the entirety of the dynamic winterization experiments is consistent with research done on other fats. Applying shear-forces during crystallization may yield a higher nucleation rate, which in turn results in a greater amount of smaller crystals forming throughout the fat during crystallization (Tran & Rousseau, 2016). These shear forces may also promote secondary nucleation, through fracturing and breaking crystals formed through primary nucleation and distributing these fractured crystalline needles throughout the solution to promote the formation of more crystals. This could possibly be the leading cause to the difference in average crystal diameter between the 50°C → 20°C for the dynamic and static winterization (see Table 11 and Table 16). The dynamic winterization range showed a large number of smaller crystals, while the static showed very large crystals overall. This means that this temperature range is capable of producing larger crystalline structures overall, but the shear-forces applied through stirring more than likely inhibited formation of these larger structures, through shattering them past a critical limit and scattering them throughout the solution. This limit is of course attributed to a certain shear-rate, meaning a limit where the agitation is not strong enough to inhibit this formation, however this is something that would be dependent on a plethora of factors, such as fat composition, cooling rate, temperature range, etc. This will be covered more in-detail in section 5.2.

For the static winterization, a total of 4 temperature ranges were crystallized. Initially, the same temperature ranges as for dynamic winterization was utilized, however for several of the temperature ranges, crystallization was not observed (see Table 6 and Table 14). To mitigate this,

the lower temperature point was lowered by 2°C and crystallization was attempted again. This then led to the temperature ranges 15°C→10°C and 10°C→4°C being used instead of 15°C→12°C and 10°C→8°C as was done for the dynamic winterization temperature ranges. For the temperature ranges 50°C → 20°C and 20°C→15°C the largest crystalline structures overall could be observed, independent of winterization method. The 50°C → 20°C static winterization temperature range had the largest crystals by far, with an average diameter of 116,3 ± 48,1 μm. Comparing this to the dynamic winterization with the same range, we can observe that the crystals grown during static winterization vastly outsize the former which only had an average diameter of 19,2 ± 12,3 μm. This seems to suggest that for this temperature range, static winterization led to the crystallization of far larger crystals overall. The same can be observed for the 20°C→15°C for dynamic and static winterization, where the latter outgrows the former vastly. This same pattern can however not be observed for the lower temperature ranges (15°C and onward). The differences in size are negligible for these temperature ranges, and they all seemed to form the same small needles and spherulite morphologies, with the exception of the dynamic winterization's 15°C→12°C temperature range which formed some aggregates. This seems to suggest that the application of shear-forces in this case promoted the greatest differences in average crystal diameter for the temperature ranges 50°C → 20°C and 20°C→15°C and led to negligible differences in average crystal diameter for the lower temperature ranges. This may be closely related to the constituting fats of the algae oil, since the solid-phase yields of the respective ranges contain the greatest portion of the overall solid yield (see Figure 22). This observation shows that a significant portion of the algae oil consists of TAGs which crystallize at 50°C → 15°C. This may be the leading cause for the overall small crystal diameters which were observed on the lower temperature ranges. The reason for this is due to an overall lack of TAGs which may crystallize at lower temperatures, which will lead to a lack of TAGs to deposit on nuclei formed during primary nucleation. This will inhibit crystal growth past a certain threshold. This could be observed independently of which winterization method was utilized, which suggests that shear-forces did not have any significant impact on the crystal formation in these temperature ranges.

5.2 – The effect of shear-forces on crystallization

The application of shear-forces on crystallization seems to carry several implications. Perhaps the most obvious implication which was observed during the practical experiments in this thesis, is the promotion of crystallization at shorter temperature ranges. This could be observed specifically in the temperature ranges 15°C→12°C and 10°C→8°C for the dynamic winterization. These temperature ranges were utilized for the static winterization as well, however in this case no crystallization could be observed (see Table 6). Instead, the temperature ranges 15°C→10°C and 10°C→4°C needed to be utilized to yield crystallization. This seems to suggest that applying shear-forces to the algae oil during equilibration promotes crystallization at a higher temperature than which could be naturally attained if no shear-forces were applied. The effect of shear-forces on crystallization of marine lipids is not well understood, however the effect on other fats such as milkfat and vegetable oils are well-known. Metin & Hartel (2005) have investigated the effect on shear-forces during crystallization of these fats and found that *"Agitation may promote nucleation because of the mechanical disturbance that supplies energy to overcome the energy barrier for nucleation"*. This correlates well with the findings in this thesis, which suggests that the reason for dynamic winterization allowing for crystallization at lower temperature ranges when compared to static winterization, is due to the shear-forces promoting nucleation through supplying energy that overcomes the energy needed for nucleation to occur.

Additionally, the agitation provided by shear-forces may also increase the cooling rate of the solution, due to more uniformly mixing the fat and thus aiding in equilibrating the temperature homogenously. An important factor to note here is the differences in crystallization temperature for the static and dynamic winterization processes' (see Table 5 and Table 6), wherein 15°C→12°C and 10°C→8°C for the static winterization did not yield crystallization on the same temperature as during dynamic winterization. Even though agitation may have yielded a faster cooling rate for the dynamic winterization experiments, this is in all likelihood not the reason for crystallization occurring at these temperature ranges, in contrast to static winterization. The static winterization experiments were equilibrated at the same temperature overnight, which eventually would lead to the same end-temperature in both the experiments. This gives more reasoning for agitation supplying the energy to overcome the nucleation energy barrier, being the leading factor to crystallization. Interestingly, below a certain limit, shear-rate may lead to a higher frequency of collisions between crystals leading to the formation of larger crystals overall (Tran & Rousseau,

2016). As mentioned previously, this shear limit is dependent on several factors and is more than likely specific for each fat. This limit may be interesting to investigate in further detail and see how it manifests in marine lipids specifically.

The mode of shear-application may also have a significant impact on the crystalline structures formed. In industrial applications impeller mixers or scraped surface heat exchangers (SSHE) may be used. Although the small-scale experiments done in this thesis does not utilize either of these methods, the turbulent flow induced by the magnetic stirring may be simplified to imitate an impeller mixer. Tran (2017) investigated the mode of shear-applications influence on crystalline structures formed and found the following. *"Statically crystallized samples showed expected spherulitic microstructures while shear-crystallized samples, regardless of shear type, inhibited the formation of spherulites and promoted the formation of spherical clusters of needle-like crystals."*. Tran's findings are consistent with the results found in this thesis; static winterization mainly yielded spherical crystalline structures for the higher temperature ranges. For dynamic winterization mainly needles and clusters were seen throughout all temperature ranges, and an increased degree of aggregation for the ranges 20°C→15°C and 15°C→12°C. These findings generally strengthen the already existing research on fats and show that they carry over to marine lipids as well. The parameters of crystallization temperature, cooling rate, shear-forces and their mode of application all seem to greatly impact crystal morphology and their resulting structures (Tran & Rousseau, 2016). For further work, it may be interesting to investigate exactly how all of these parameters specifically impact the crystallization and crystal structures of marine lipids specifically, and if they somehow differ. The matter of a critical shear-rate limit which may promote the formation of larger crystal sizes, or alternatively yield fracturing of larger crystal structures and promote smaller needle and platelet structures, has not yet been investigated for marine lipids. Acevedo et al. investigated the effects of laminar-shear on fully-hydrogenated soybean oil and how the parameters of shear-rate and crystallization temperature impact the formation of crystal morphologies (Acevedo et al., 2012). The findings showed that spheroidal crystal structures formed as a function of the shear-rate, which strengthened the proof of existence of a critical shear-rate that promotes crystal aggregation and growth below a certain limit. Exceeding this limit may however lead to larger structures shattering and promoting the formation of smaller structures, and inhibit aggregation to form larger crystalline networks (Chaiseri & Dimick, 1995) (Garside & Davey, 1980). This shear-limit

function has been investigated mostly in vegetable oils, which typically contain different TAG compositions than marine lipids. Research on this shear-rate limit has not yet been conducted for marine lipids. However, the findings in this thesis seem to suggest that the shear-rate utilized for marine lipids yielded expected results when compared to Acevedo's findings. The shear-rate which was utilized in the dynamic winterization experiments probably exceeded this critical shear-rate and therefore yielded smaller crystalline structures overall, through the fracturing of larger crystal structures that may have otherwise formed, as seen in the static winterization experiments. Investigating where this critical shear-limit lay specifically for marine lipids may be an interesting area to investigate in further detail.
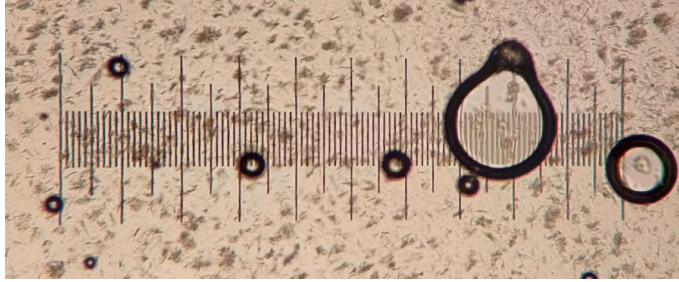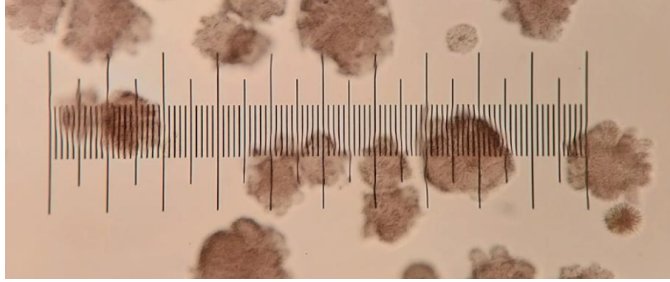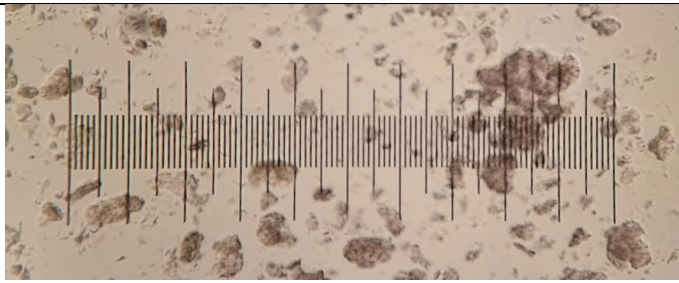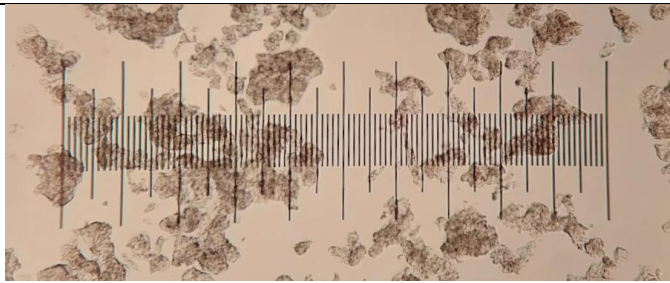
5.3 – Separation efficiency

The primary goal of winterization is to separate the different fractions of the fat, utilizing their melting and crystallization points to achieve this. This separation process is dependent on a plethora of factors, namely crystal size, distribution, the polymorphism of the present crystals, and their three-dimensional shape (Smith, 2001). As mentioned in section 5.1, the morphology and three-dimensional structures of the crystals and their resulting networks is dependent on several factors, and this in turn has the potential to greatly affect the separation efficiency of the solid and liquid fractions. During the crystallization process, different TAGs start crystallizing due to their inherent thermodynamic properties, and resultingly form crystals. In this process, the solid phase starts forming and may interact with the liquid-phase in an adverse manner. A phenomenon that takes place during this process is entrainment. Entrainment occurs when the liquid fraction becomes entrapped within the solid-phase's crystalline structures. This may either manifest through liquid entrapment between individual crystals that form agglomerates, known as intra-particle entrapment, or between larger crystal agglomerates, known as inter-particle entrapment (Hishamuddin et al., 2020). The extent of this entrainment, that being the amount of liquid-phase entrapped in the solid-phase, is dependent on the aforementioned factors of crystal size, morphology and distribution. When separation takes place, the liquid which is entrapped may not pass through the filter and therefore reduce the efficiency of separation. This in turn will give less yield of the liquid-fraction, and at the same time reduce the quality of the solid-phase's purity. This aspect is a relevant problem even with today's technology, and as a result the composition of the solid phase can never truly present a completely pure fraction containing only the crystallized TAGs respectively.

Another important factor in regard to separation efficiency is whether agitation is applied or not, as this massively affects the crystallization conditions as previously mentioned. Smith (2001) investigated entrainment within stirred systems (shear-driven) and found *"In stirred systems, especially, the growing crystals can agglomerate, trapping olein within the particles as they do so. This trapped olein can be virtually impossible to remove by any separation method."*. An important factor to note here however is that this assumes a shear-rate which does not exceed the critical limit, as was probably the case in this thesis' experiments for dynamic winterization. As mentioned, below the critical shear-rate the growth of crystals will be promoted and instead for m larger crystals overall. In this thesis' experiments however, smaller crystalline structures were formed, which led to a lower degree of agglomeration when compared to static winterization. A benefit of this is that very little of the liquid-phase is trapped in the solid-phase, through intra- and inter-particle entrainment. Although this reduces the amount of entrainment in total, the presence of smaller crystal particles presents another problem that manifests in filtering efficiency. These smaller particles may become trapped in the filter's pores, and clog them, leading to difficulty with pulling the liquid-phase through. This can in turn reduce efficiency and retain liquid in the solid phase. A consensus however is that spherical crystals, which often manifest in β'-polymorphism, is the easiest to separate as they don't clog the filter and don't entrap too much liquid-phase. This stands in contrast of β crystals which often manifest as needles and clog the filter.

The largest differences in crystal morphology and networks could be seen for the temperature ranges 50°C→20°C and 20°C→15°C for dynamic and static winterization. These temperature ranges also had the largest yields of their respective solid fractions, which means this is where a large amount of the compositional TAGs in the algae oil reside (see Table 8 and Table 13). Table 21 shows a comparison between dynamic and static winterization crystal structures for their respective temperature ranges.

Table 21: An overview of the crystalline structures observed during dynamic and static winterization, for the temperature ranges 50℃→20℃ and 20℃→15℃, which compares the structures observed between the respective methods.

Temperature range	Dynamic winterization	Static winterization
50℃→20℃		
20℃→15℃		

For the 50℃→20℃ temperature range, there is a vast difference in the crystal structures and sizes between the winterization methods. Dynamic winterization yielded quite small crystals with a needle morphology, that were finely dispersed in the slurry. These crystals did not agglomerate and form networks, which means that most likely there was little liquid entrainment. This is strengthened by the fact that this fraction also had a relatively high liquid yield, which was 228,09g and comprising 80.1% of the total yield (see Table 8). The static winterization on the other hand yielded quite large spherulites and showed slight agglomeration. This means that it is probable to assume part of the liquid fraction was trapped through intra-particle and inter-particle entrainment. This is also strengthened by the fact that the liquid phase yield here was 192,20g and comprising 66.9% of the total yield (see Table 13). When comparing to the dynamic winterization, this method gave a 13.2% decrease in liquid-fraction yield. Even though there is the likelihood of the static winterization's needle crystals clogging the filter, this effect seems to have had a less adverse impact than the entrainment which may have happened for the static winterization. Comparatively, the static winterization had a faster filtering, taking 60 minutes compared to dynamic winterization's 95 minutes. This is however most likely due to the fact that the dynamic winterization had more liquid that had to be pulled through, though clogging of the

pores due to the presence of needle crystals could be a factor for the additional time required for filtering.

For the 20°C→15°C temperature range, the crystal morphologies are more uniform. The static winterization crystals were however slightly larger than their counterpart. The static winterization crystals also showed a higher degree of agglomeration, and larger networks. This may come as a result of the fact that no shear-forces were present to break up and the networks which may form. This in turn could allow a higher degree of sintering to connect the structures together and allow for more agglomeration. The dynamic winterization crystals did also show a degree of agglomeration, but not on the same level as their static counterparts. This fraction also had the appearance of some smaller needle crystals. When it comes to the liquid-yield for the dynamic and static winterization experiments, their yield was quite similar, though the static winterization yielded slightly more. The dynamic winterization liquid-phase yield was 82,49g and comprised 48.7% of the total yield (see Table 8), while the static winterization liquid-phase yield was 92,62g and comprised 55.2% of the total yield (see Table 13). An important note here however is that the liquid fraction which was yielded from 50°C→20°C was the basis for this winterization, and the weight differed between these two, where the dynamic winterization started with 224,74g in total, and the static winterization started with 188,21g in total. Even so, the static winterization yielded more liquid fraction than the dynamic winterization. Both methods yielded agglomeration in this case, which suggests a degree of entrainment present for both. The dynamic winterization did however yield slightly less, and also had a longer elapsed time for filtering compared to the static winterization, taking 200 and 145 minutes respectively. The reasoning for this could be needle crystals which clog the filter pores, and therefore lead to a longer time needed for the liquid fraction to pull through the filter.

5.4 – Thermodynamic properties

As mentioned, the TAGs which comprise fats are often numerous, and as such have different melting points and crystallization points as a result of the fatty acids which they consist of (Walstra, 1987). There is also an inherent relationship between the heat of fusion (ΔH_{fus}), i.e the energy required to convert a solid into a liquid, and the melting temperatures for the TAGs. While individual FAs may have specific melting temperatures, TAGs composed of several FAs will have melting ranges instead. This in hand will give most fats melting ranges, wherein the ratio of liquid to solid fat can vary depending on temperature. This can also be observed in the DSC graphs in Table 20, where all the temperature ranges and their respective fractions have several transition points which can be observed. At these areas, certain TAGs which compose the fat convert from a crystalline solid form to a liquid phase, as a result of the increasing temperature. By calculating the integral of these transition points on the graphs, we can find ΔH_{fus} at specific temperatures, which will correspond with a TAG that is able to undergo a phase-transition at the given temperature. This ΔH_{fus} will of course vary depending on a plethora of factors related to the TAG, such as the comprising FAs, their inherent structures, and any eventual polymorphism which the crystalline structures may exist in.

Table 22 depicts all the fractions' respective temperature range, their phase transitions' heat of fusion (ΔH_{fus}) in J/g, the respective phase transition onset ($T_{g\ onset}$) and phase transition end ($T_{g\ end}$) in °C.

Table 22: A table depicting the respective fractions' phase-transitions, and their temperature onset ($T_{g\ onset}$), end ($T_{g\ end}$) and the heat of fusion (ΔH_{fus}) for the respective transition temperatures.

	Transition 1	Transition 2	Transition 3
Liquid 50°C→20°C	$T_{g\ onset}$: -38.88 °C $T_{g\ end}$: -31.45 °C ΔH_{fus}: 4.722 J/g	$T_{g\ onset}$: -13.67 °C $T_{g\ end}$: -5.98 °C ΔH_{fus}: 2.046 J/g	$T_{g\ onset}$: 13.27 °C $T_{g\ end}$: 20.09 °C ΔH_{fus}: 57.67 J/g
Solid 50°C→20°C	$T_{g\ onset}$: -38.58 °C $T_{g\ end}$: -31.88 °C ΔH_{fus}: 1.694 J/g	$T_{g\ onset}$: 14.84 °C $T_{g\ end}$: 20.67 °C ΔH_{fus}: 32.25 J/g	$T_{g\ onset}$: 39.52 °C $T_{g\ end}$: 48.13 °C ΔH_{fus}: 58.32 J/g
Liquid 20°C→15°C	$T_{g\ onset}$: -116.78 °C $T_{g\ end}$: -113.76 °C ΔH_{fus}: 0.2387 J/g	$T_{g\ onset}$: -39.76 °C $T_{g\ end}$: -32.24 °C ΔH_{fus}: 6.100 J/g	$T_{g\ onset}$: -2.60 °C $T_{g\ end}$: 15.11 °C ΔH_{fus}: 46.58 J/g
Solid 20°C→15°C	$T_{g\ onset}$: -38.45 °C $T_{g\ end}$: -31.60 °C ΔH_{fus}: 2.525 J/g	$T_{g\ onset}$: 18.51 °C $T_{g\ end}$: 22.64 °C ΔH_{fus}: 78.63 J/g	$T_{g\ onset}$: $T_{g\ end}$: ΔH_{fus}:
Liquid 15°C→12°C	$T_{g\ onset}$: -116.40 °C $T_{g\ end}$: -115.83 °C ΔH_{fus}: 0.091 J/g	$T_{g\ onset}$: -40.06 °C $T_{g\ end}$: -32.30 °C ΔH_{fus}: 6.675 J/g	$T_{g\ onset}$: -2.80 °C $T_{g\ end}$: 14.66 °C ΔH_{fus}: 46.80 J/g
Solid 15°C→12°C	$T_{g\ onset}$: -36.13 °C $T_{g\ end}$: -31.68 °C ΔH_{fus}: 0.789 J/g	$T_{g\ onset}$: 19.40 °C $T_{g\ end}$: 23.75 °C ΔH_{fus}: 85.65 J/g	$T_{g\ onset}$: $T_{g\ end}$: ΔH_{fus}:

Of note from this table, is the fact that the liquid fractions expectedly have a lower T_g onset and T_g end temperature for their most energy demanding phase-transitions (ΔH_{fus}) when compared to their solid fraction counterparts. This temperature difference seems to occur roughly 10-20°C later for the solid fraction, than its liquid fraction counterpart. Interestingly, each temperature range also contained a phase-transition occurring around the -30°C temperature mark, regardless of fraction. This seems to suggest that a specific part of the algae oil was present in all fractions, and was able to pull through the filter, and still have a part remain entrained in the solid fraction. Though the ΔH_{fus} seems to vary slightly between each temperature range and fraction, it still seems to correlate with the same phase-transition which occurs in all the other temperature ranges and fractions. When observing the ΔH_{fus} for the -30°C temperature marks and comparing them

between the solid and liquid fractions respectively, we can observe that the liquid fractions ΔH_{fus} is comparatively higher, which suggests a higher ratio of this specific TAG present in the liquid fractions. This correlates with the assumption that the -30°C phase-transitions in the solid fractions is due to entrainment. Intriguingly, from the 20°C→15°C temperature range and lower, both liquid fractions can be observed to have a glass transition occurring. This glass transition seems to have a $T_{g\ onset}$ of -116°C, and a $T_{g\ end}$ around -113°C, though the former varied slightly between the temperature ranges. When compared with TAGs from Table 1, this glass transition might represent the TAG 18:2ω(9c,12c) (2x) 16 (LiLiP), although the $T_{g\ onset}$ seems to deviate slightly and occur at a higher temperature than the TAG described in Table 1. This might be a result of inaccurate integration or slight variations in the precision of instruments utilized in this thesis compared to Table 1. The $T_{g\ end}$ temperature however seems to be accurate, especially when compared with the 20°C→15°C temperature range's first phase-transition point. Expectingly, none of the solid fractions exhibited signs of a glass transition, as any TAG which is capable of undergoing glass transition would more than likely be pulled through the filter, as they never exist in a purely solid form. The only possibility would be if such a TAG was entrained in the solid phase, though this seems to not have occurred in this case. For all the temperature ranges, the phase-transitions with the highest relative ΔH_{fus} occurred between the temperature range -2°C and 48°C, which suggest that the majority of the TAGs which compose the algae oil have melting ranges in this specific temperature range. It is also possible to investigate the relationship between solid and liquid fraction ratios at given temperatures by utilizing the DSC graphs. As mentioned in section 2.6, there is an inherent relationship between these fractions, where the liquid fraction may act as a solvent for the solid fraction, and ultimately affect the ratio of solid to liquid at a greater degree. This effect can also be observed by investigating this ratio. Utilizing equation 5, we can describe the ΔH_{fus} for a given melting temperature. This describes the dependence between ΔH_{fus} and the melting temperature T_m.

Equation 5

$$\Delta H = 2.08 * 10^{-7} * \left(\frac{1}{273.02 + Tm}\right)^{-3.61}$$

This equation can be utilized for finding the ratio of solid to liquid content in a given TAG mixture of marine lipids (Tolstorebrov et al., 2014). Consequently, the amount of melted solid-mass for a given ΔT can be found by investigating the energy absorbed by the DSC sample during the specific temperature range (i.e $ET_2 - T_1$) and plotting this to the average heat of fusion ($\Delta H_{fus\ avg}$) for the given temperature range. This gives rise to the following equation.

Equation 6

$$mT2 - T1 = \frac{E(T2 - T1)}{\Delta Hfus\ avg.}$$

By then calculating the integral of mT, where T is the temperature range expressed in the DSC graph, we can find the percentage of liquid fraction oil as a function of temperature. This gives rise to the following equation.

Equation 7

$$mt = \int_{T\ m0}^{T} mdT$$

In this equation, mt is the percentage of melted sample at a given temperature range, T and T_{m0} is the temperature range in which DSC graph is expressed for, and mdT is the change in weight with respect to temperature. By exporting the inverse running integral of the DSC graphs depicted in Table 20, and utilizing equations 5-7, we can plot the percentage of liquid-phase volume by percentage, as a function of temperature. This can be seen in Figure 23, which depicts this relationship for all analyzed samples.
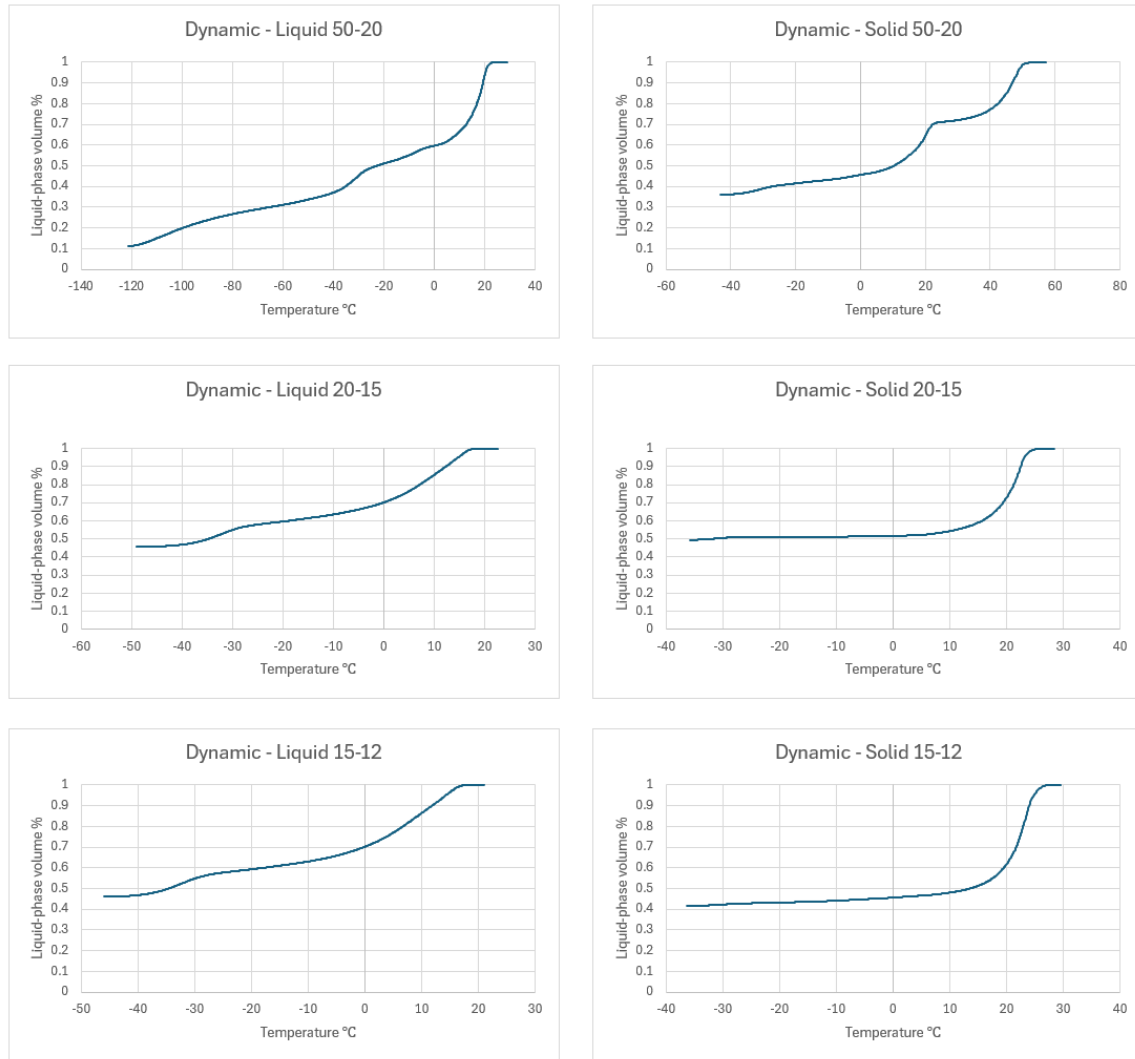
Figure 23: A figure depicting the dynamic winterization's oil fractions as a function of temperature. The y-axis is the percentage of liquid oil at a given temperature, while the y-axis depicts temperature in ℃.

For all the temperature ranges, there is a clear relationship between the solid and liquid fractions that have been separated. At all given temperature points, the separated liquid fractions has a higher liquid-phase volume compared to their solid fraction counterparts. There is also a clear difference in the temperature in which the respective liquid and solid fractions reach their maximum liquid-phase volume peaks. All the liquid fractions are completely liquid at 20℃, while their solid fraction counterparts only reach this point after at least a 10℃-temperature increase, with the most extreme result showing for the 50℃→20℃ solid fraction. In this fraction, the liquid and solid counterparts have nearly a 30℃-temperature difference for their respective liquid-phase volume peaks.

The liquid-phase volume for the liquid fractions seems to steadily increase as the temperature increases, reaching a peak at around 20°C. We can additionally observe a phase-transition occurring at $T_{g\ onset}$ = -30°C, which is consistent with observations in Table 22. On the other hand, the solid-fractions peak liquid-phase volume is reached at roughly 25-30°C, with a $T_{g\ onset}$ = 20°C. The 50°C→20°C stands as the exception by having this $T_{g\ onset}$ = 20°C, but also having an additional phase-transition at roughly $T_{g\ onset}$ = 40°C. This is expected, due to the fact that this fraction most likely contains the higher melting point TAGs that were fractionated in the first initial winterization. For the 20°C→15°C and 15°C→12°C, their melting peaks seem to occur at roughly the same time. This may correlate to the fact that the 15°C→12°C solid fraction had quite a low yield (2.72g), which may be a result of TAGs that were just under the crystallization point of the prior winterization.

5.5 – Fatty acid composition

During the analysis of fatty acid composition of the temperature ranges obtained from static and dynamic winterization, the commercial fatty acid standard "Advanced FAME Supelco 37" was utilized. The retention time (rT) of each fatty acid was compared to the rT's observed in each sample. When observing the rT's for the fatty acids *lignoceric acid* (C24:0), *nervonic acid* (C24:1) and *docosahexaenoic acid* (DHA / C22:6), their peaks in the GC graph had significant overlap, which made separating them from one another difficult (see appendix 11 and 12). Though, seeing as the algae oil utilized for this thesis is already known to contain significant amounts of *docosahexaenoic acid*, as was informed beforehand from the labelling on the algae oil, we assume that all the peaks observed with the respective rT's for these fatty acids are all *docosahexaenoic acid*. There was also no indications of any MUFA's observed in the GC graphs. Additionally, all the PUFA's found in the samples were ω-3 fatty acids. These are the fatty acids *eicosatrienoic acid* (C20:3), *eicosapentaenoic acid* (C20:5) and *docosahexaenoic acid* (C22:6). Table 23 and Table 24 show the concentrations of SFA and PUFA in the analyzed samples for dynamic and static winterization respectively, as well as the respective concentrations of the ω-3 fatty acids *eicosatrienoic acid* (C20:3)*, eicosapentaenoic acid* (C20:5) and *docosahexaenoic acid* (C22:6). For the static winterization, the sample Solid 10-4 is omitted due to assumed contamination, which did not give any meaningful results.

Temperature range and fraction	S 50-20	S 20-15	S 15-12	S 12-10	S 10-8	L 50-20	L 20-15	L 15-12	L 12-10	L 10-8
SFA	57.21 %	53.25 %	53.00 %	51.11 %	51.31 %	72.06 %	56.80 %	64.05 %	62.24 %	59.67 %
PUFA	40.84 %	44.27 %	44.50 %	45.30 %	45.06 %	24.35 %	35.96 %	34.75 %	35.06 %	36.63 %
% C20:3	0.70%	0.81%	0.83%	0.91%	0.94%	0.70%	0.53%	0.47%	0.43%	0.56%
% EPA (C20:5)	0.50%	0.59%	0.57%	0.67%	0.69%	0.53%	0.39%	0.33%	0.30%	0.45%
% DHA (C22:6)	39.64 %	42.87 %	43.10 %	43.73 %	43.44 %	23.12 %	35.05 %	33.95 %	34.33 %	35.62 %

Temperature range and fraction	S 50-20	S 20-15	S 15-10	F 50-20	F 20-15	F 15-10	F 10-4
SFA	61.47%	60.10%	58.85%	49.77%	50.67%	48.16%	47.05%
PUFA	32.66%	35.82%	38.81%	35.74%	43.31%	46.70%	47.79%
% C20:3	0.57%	0.51%	0.65%	0.64%	0.90%	1.09%	1.19%
% EPA (C20:5)	0.42%	0.38%	0.48%	0.51%	0.72%	0.77%	0.86%
% DHA (C22:6)	31.67%	34.93%	37.68%	34.59%	41.70%	44.84%	45.74%

When observing the SFA and PUFA concentrations for the dynamic winterization, we can see variable trends in the concentrations between the samples. For the solid fractions, there seems to be a steady lowering in the SFA content, between all the temperature ranges, except for

10°C→8°C where it has a minor increase. The overall content does however seem to stay stable around 57-51% Consequentially, the PUFA content increases in all of these temperature ranges as well, increasing from about 40% to 45%. For the liquid fractions a variable pattern is seen between the temperature ranges, with an initial lowering, an increase and then a lowering yet again. The liquid fractions also had a surprisingly high content of SFA, with the 50°C→20°C containing 72.06% SFA, though the following winterizations seemed to lower this amount. The PUFA content acted as the inverse of this, and had an initial increase, a slight decrease and then yet another increase. The variations were however quite small, and only varied by about 1-2%. For all the temperature ranges, these observations in SFA and PUFA content did not act out as initially expected. Expectingly, one might assume that the SFA content in the solid fractions would steadily increase, and the PUFA content to decrease, and the inverse for the liquid fractions. This obviously did not happen. Similar observations as was made for PUFA can be made for the content of ω-3 fatty acids in all the temperature ranges. Surprisingly, the content of ω-3 was higher in the solid fraction than the liquid. Seeing as these fatty acids undergo glass transitions instead of crystallizing in a solid form, this suggests a high degree of entrainment happening during dynamic winterization.

When comparing with results from other studies (Morales-Medina et al., 2016) (Khan et al., 2021), there is an obvious trend of the PUFA content increasing in the liquid fraction, and the SFA fraction increasing in the solid fraction. This is expected to occur as fatty acids, which are often saturated, crystallize at the given temperature ranges and are separated out of the liquid fraction, thereby increasing the total volume of PUFA present in the fraction. There is, however, no solid trend for this happening in the dynamic winterizations performed. Looking for similar results in other studies did not yield any meaningful findings. When compared with Table 24, which has not yet been discussed, we can however very clearly observe the expected trend that similar studies show. This leaves speculation for the fact that the shear forces induced in the dynamic winterization had significant influence in the formation of crystals. It is known that utilizing a slow-cooling rate, along with a low shear-rate may result in a higher number of compound crystals forming during crystallization, and therefore influencing the melting range of the crystals which are formed (Metin & Hartel, 2005). Compound crystals are, as discussed in section 2.2, crystals which incorporate several TAGs in the crystal structure. Though we assume the shear-rate limit to be exceeded in the experiments performed in this case, there may yet be a

similar effect which had occurred during crystallization of the oil. The effect of compound crystal formation during dynamic winterization may have caused the melting ranges of the present TAGs to vary to such a degree that they crystallized outside of their expected areas, and therefore lead to the results observed. An example of this may be a TAG consisting of mainly PUFA which is expected to crystallize at a relatively low temperature, forming compound crystals with mainly SFA containing TAG crystals. The resulting melting range of the compound crystals which are formed will then be shifted towards a higher temperature, therefore crystallizing the PUFA containing TAG at a higher temperature than which may have taken place at the absence of compound crystals. This in turn will lead to the solid fraction containing PUFA containing TAGs, despite the solid fraction initially being expected to mainly contain SFA TAGs. This will also inherently lower the PUFA content of the resulting liquid fraction and influence the fatty acid composition of both fractions. Even so, there is a general trend observed among the results, that the PUFA content increases as the temperature range lowers, which is according to theory. Especially for the 50°C→20°C range, there is a clear increase in the PUFA content.

When observing the SFA and PUFA concentrations for the static winterization, there is a much clearer trend being observed. The exception stands for the solid fractions, where the SFA content seems to decrease as the temperature is being lowered, however this might be explained by the fact that the total SFA content is being reduced as the previous solid fractions remove the majority of the SFA which crystallizes in earlier fractions, therefore leaving a higher fraction of PUFA behind instead. This can also be observed as the PUFA content increases by up to 6% from the highest to the lowest temperature range. There is also a possibility of entrainment happening, where liquid oil is trapped between the crystal structures through intra- and inter-entrainment. This is especially more likely, due to the crystal morphologies observed in static winterization, where large spherulites and agglomerates formed. The SFA content for the solid fractions seem to decrease steadily, with the highest concentration being seen in the 50°C→20°C range, which makes sense as this was the fraction with the highest solid content yield. The 10°C→4°C solid sample was unfortunately assumed to be contaminated and did not yield any meaningful results, however we may assume that the trend in SFA content is equal as the previous ranges. When it comes to the ω-3 fatty acids, the content seems to steadily increase as the temperature lowers, which is additional proof of entrainment happening, as these fatty acids will not crystallize into a normal solid-phase. For *docosahexaenoic acid* (C22:6) the content increases, but for

eicosatrienoic acid (C20:3) and *eicosapentaenoic acid* (C20:5), there seems to be a slight dip in the content during the 20°C→15°C range. This does, however, increase again in the following temperature range.

The liquid fractions for the static winterization have an expected trend, where the SFA content decreases as the temperature range goes lower, and the PUFA content increases. This fraction specifically is the most conformant to previous studies (Morales-Medina et al., 2016) (Khan et al., 2021). The only exception stands for the 20°C→15°C temperature range, where the inverse was observed for the solid fractions, we can see a slight increase in the SFA content and slight decrease in PUFA. The following temperature ranges does however show the opposite, which is according to expectations. The total SFA content does not however seem to decrease by a lot, as the difference between the fractions for the 50°C→20°C and 10°C→4°C temperature ranges only has a difference of above 2%. We can however see a steady increase in the PUFA content, with a total increase of nearly 12% from the highest to the lowest temperature range. Additionally, we can observe an almost similar increase in the concentration for the ω-3 fatty acids, where *docosahexaenoic acid* (C22:6) increases by over 10%. Though the total content of the other ω-3 fatty acids, *eicosatrienoic acid* (C20:3) and *eicosapentaenoic acid* (C20:5), is quite low, we can still see a slight increase. In general, the results for static winterization are mostly conformant to theory, and past studies done. The PUFA content increases across nearly all temperature ranges, as the SFA content is lowered due to selective separation of TAGs which crystallize at the given temperatures.

6. Conclusion

In this thesis, the effect of shear-driven and static winterization on crystal morphology and separation efficiency was investigated. Both methods of winterization had significant and distinct influences on the crystalline structures formed during crystallization, the respective yields, and the efficiency during processing. The effects of applying shear-forces during crystallization had a distinct influence when compared to crystallizing with no agitation present in the oil. Shear forces led to the formation of small crystals finely dispersed in the solution. This is thought to have happened due to exceeding a critical shear-rate limit, which greatly influences the morphologies during crystallization. The absence of shear-forces seems to have influenced the crystalline formation in a manner of greatly increasing the average diameter of crystals formed. Additionally, a larger degree of agglomeration and spherulite formation was observed, which stands in contrast to the shear-driven winterization's smaller needle like crystals.

When considering the separation efficiency of both winterization methods, the absence of shear-forces may have proven beneficial by forming crystals that are easier to separate. This stands in contrast to shear-driven winterization, which led to the formation of crystals that may have clogged the filter pores. Though agitation did allow for crystallization at lower temperature increments. Considering the results from GC-analysis, the absence of shear-forces also proved more efficient due to consistently increasing the PUFA content in the liquid fractions, which stands in contrast to the shear-driven winterization's results. The results from DSC showed that winterization was effective in separating TAGs into fractions which had differing melting ranges. The liquid fractions from the winterization had a consistently higher liquid-phase volume when compared to the solid-fraction counterparts. DSC showed the different phase-transition points which occurred in the different fractions, as well as the ΔH_{fus} for the phase-transitions.

In conclusion, winterization with an absence of shear-forces proved to be a more efficient winterization method in this thesis. Applying shear-forces during winterization had a negative impact on separation efficiency and yield, though this is more than likely due to exceeding a shear-rate limit. Utilizing a lower shear-rate may have led to more beneficial results for the shear-driven winterization.

6.1 – Suggestion for future research

A significant influence of the results in this thesis is the utilization of a shear-rate in the dynamic winterization which exceeded a critical limit. Existing studies suggest that shear-forces will generally have a positive impact on crystal morphology and crystal formation. For future research, it might be beneficial to utilize a shear-rate which does not exceed this limit. Comparing the results of this against the static winterization results may prove to provide a better insight on the benefits of both methods. This is especially important due to the fact that most industrial applications of winterization utilize shear-forces, so comparing the two on equal grounds is important. Another aspect which may be interesting to investigate is the DSC properties of all the fractions. In this thesis this was not done due to time and resource constraints, so investigating this in the future may be interesting and provide more insight on the differences in thermodynamic properties for the samples obtained by both methods.

7. Reference list

2. Abiad, M., Campanella, O., & Carvajal, M. T. (2014). Effect of Spray Drying Conditions on the Physicochemical Properties and Enthalpy Relaxation of α-Lactose. *International Journal of Food Properties*, *17*. https://doi.org/10.1080/10942912.2012.710287

3. Acevedo, N. C., Block, J. M., & Marangoni, A. G. (2012). Critical laminar shear-temperature effects on the nano- and mesoscale structure of a model fat and its relationship to oil binding and rheological properties [10.1039/C2FD20008B]. *Faraday Discussions*, *158*(0), 171-194. https://doi.org/10.1039/C2FD20008B

4. Alfieri, A., Imperlini, E., Nigro, E., Vitucci, D., Orrù, S., Daniele, A., Buono, P., & Mancini, A. (2017). Effects of Plant Oil Interesterified Triacylglycerols on Lipemia and Human Health. *Int J Mol Sci*, *19*(1). https://doi.org/10.3390/ijms19010104

5. Bou Mira, M. (2016). *Metabolism of omega-3 very long-chain polyunsaturated fatty acids in Atlantic salmon (Salmo salar L) : Effects of different dietary levels of EPA and DHA on fish performance and health = Metabolisme av omega-3 fettsyrer i atlantisk laks (Salmo salar L) : effekt av ulike nivåer av EPA and DHA i foret på fiskens helse* Norwegian University of Life Sciences, Department of Animal and Aquacultural Sciences]. Ås.

6. Breivik, H. (2007). *Long-chain omega-3 specialty oils*. Oily Press.

7. Chaiseri, S., & Dimick, P. S. (1995). Dynamic crystallization of cocoa butter. II. Morphological, thermal, and chemical characteristics during crystal growth. *Journal of the American Oil Chemists' Society*, *72*(12), 1497-1504. https://doi.org/https://doi.org/10.1007/BF02577843

8. Coultate, T. (2023). *Food: the chemistry of its components*. Royal Society of Chemistry.

9. Dyre, J. C. (2006). Colloquium: The glass transition and elastic models of glass-forming liquids. *Reviews of Modern Physics*, *78*(3), 953-972. https://doi.org/10.1103/RevModPhys.78.953

10. Garside, J., & Davey, R. J. (1980). INVITED REVIEW SECONDARY CONTACT NUCLEATION: KINETICS, GROWTH AND SCALE-UP. *Chemical Engineering Communications*, *4*(4-5), 393-424. https://doi.org/10.1080/00986448008935918

11. Hartel, R., & Kaylegian, K. (2001). Advances in milk fat fractionation. *Crystallization processes in fats and lipid systems*, 381-427.

12. Hishamuddin, E., Nagy, Z. K., & Stapley, A. G. F. (2020). Thermodynamic analysis of the isothermal fractionation of palm oil using a novel method for entrainment correction. *Journal of Food Engineering*, *273*, 109806. https://doi.org/https://doi.org/10.1016/j.jfoodeng.2019.109806

13. Khan, A., Nadeem, M., Imran, M., & Khalique, A. (2021). Impact of winterization on fatty acids' composition, isomers, and oxidative stability of conjugated linoleic acids produced from selected

vegetable oils. *Journal of Food Processing and Preservation*, *45*(3), e15254. https://doi.org/https://doi.org/10.1111/jfpp.15254

14. Kreulen, H. P. (1976). Fractionation and winterization of edible fats and oils. *Journal of the American Oil Chemists' Society*, *53*(6), 393-396. https://doi.org/10.1007/BF02605729

15. Lei, Q., Ba, S., Zhang, H., Wei, Y., Lee, J. Y., & Li, T. (2016). Enrichment of omega-3 fatty acids in cod liver oil via alternate solvent winterization and enzymatic interesterification. *Food Chemistry*, *199*, 364-371. https://doi.org/https://doi.org/10.1016/j.foodchem.2015.12.005

16. Litwinenko, J. W., Rojas, A. M., Gerschenson, L. N., & Marangoni, A. G. (2002). Relationship between crystallization behavior, microstructure, and mechanical properties in a palm oil-based shortening. *Journal of the American Oil Chemists' Society*, *79*(7), 647-654. https://doi.org/10.1007/s11746-002-0538-y

17. McGill, A. S., & Moffat, C. F. (1992). A study of the composition of fish liver and body oil triglycerides. *Lipids*, *27*(5), 360-370. https://doi.org/10.1007/BF02536151

18. Metin, S., & Hartel, R. W. (2005). Crystallization of fats and oils. *1*, 45-76.

19. Morales-Medina, R., De León, G., Munio, M., Guadix, A., & Guadix, E. (2016). Mass transfer modeling of sardine oil polyunsaturated fatty acid (PUFA) concentration by low temperature crystallization. *Journal of Food Engineering*, *183*, 16-23. https://doi.org/https://doi.org/10.1016/j.jfoodeng.2016.03.009

20. Nguyen, V., Rimaux, T., Truong, V., Dewettinck, K., & Van Bockstaele, F. (2020). Fat crystallization of blends of palm oil and anhydrous milk fat: A comparison between static and dynamic-crystallization. *Food Res Int*, *137*, 109412-109412. https://doi.org/10.1016/j.foodres.2020.109412

21. NTNU, I. f. b. o. m. (2022). Bligh & Dyers metode, MATV1009. Matkjemi 1.

22. Petricorena, Z. C. (2015). Chemical composition of fish and fishery products. *Handbook of food chemistry*, *1*, 28.

23. Pike, I. H., & Jackson, A. (2010). Fish oil: production and use now and in the future. *Lipid Technology*, *22*(3), 59-61. https://doi.org/https://doi.org/10.1002/lite.201000003

24. Russo, G. L., Langellotti, A. L., Oliviero, M., Sacchi, R., & Masi, P. (2021). Sustainable production of food grade omega-3 oil using aquatic protists: Reliability and future horizons. *New Biotechnology*, *62*, 32-39. https://doi.org/https://doi.org/10.1016/j.nbt.2021.01.006

25. Smith, K. W. (2001). Crystallization of palm oil and its fractions. *Crystallization processes in fats and lipid systems*, 357-380.

26. Sullivan, J. C., Budge, S. M., & St-Onge, M. (2009). Determining Ethyl Esters in Fish Oil with Solid Phase Microextraction and GC–MS. *Journal of the American Oil Chemists' Society*, *86*(8), 743-748. https://doi.org/https://doi.org/10.1007/s11746-009-1412-5

27. Swanson, D., Block, R., & Mousa, S. A. (2012). Omega-3 fatty acids EPA and DHA: health benefits throughout life. *Advances in nutrition*, *3*(1), 1-7.

28. Tolstorebrov, I. (2014). *A study of the ultra-low temperature application for fish freezing and storage* Norwegian University of Science and Technology, Faculty of Engineering Science and Technology, Department of Energy and Process Engineering]. Trondheim.

29. Tolstorebrov, I., Eikevik, T., & Bantle, M. (2014). A DSC determination of phase transitions and liquid fraction in fish oils and mixtures of triacylglycerides. *Food Research International*, *58*, 132-140.

30. Tran, T., & Rousseau, D. (2016). Influence of shear on fat crystallization. *Food Research International*, *81*, 157-162. https://doi.org/https://doi.org/10.1016/j.foodres.2015.12.022

31. Walstra, P. (1987). Fat Crystallization. In J. M. V. Blanshard & P. Lillford (Eds.), *Food Structure and Behaviour* (Vol. 1). Academic Press Limited.

32. Walstra, P., Kloek, W., & Van Vliet, T. (2001). Fat crystal networks. *Crystallization processes in fats and lipid systems*, 289-328.

33. Yoon, B., Jackman, J., Valle, E., & Cho, N. (2018). Antibacterial Free Fatty Acids and Monoglycerides: Biological Activities, Experimental Testing, and Therapeutic Applications. *International Journal of Molecular Sciences*, *19*, 1114. https://doi.org/10.3390/ijms19041114

8. Appendix

Appendix 1 – Excel sheet of measured crystal diameters, average diameter, median, standard deviation and largest/smallest diameters observed.

|	A	B 50-20 (D1)	C 50-20(D2)	D 20-15(D1)	E 20-15(D2)	F	G 15-12 (D2)	H 12-10 (D2)	I 10-8 (D2)	J	K 50-20 (D1)	L 50-20 (D2)	M 20-15 (D1)	N 20-15 (D2)	O 15-10 (D2)	P 10-4 (D2)
2		20	20	60	60		60	20	5		85	50	50	25	40	10
3		5	30	50	90		50	10	10		90	160	100	65	50	5
4		20	20	60	50		30	10	5		75	140	20	40	20	5
5		25	20	50	80		70	40	30		90	125	10	120	35	5
6		30	30	30	30		20	15	30		110	155	10	165	20	5
7		25	10	30	20		60	50	5		120	160	15	140	20	5
8		10	25	50	90		20	25	5		125	135	10	110	30	10
9		5	20	60	180		10	5	10			95	25	140	40	15
10		30	40	60	55		45	5	8			100	20	110	20	15
11		20	20	30	25		25	15	10			190	20	60	35	20
12		5	5	100	45		75	10	13			200	40	310	20	10
13		10	15	105	85		60	8	10			150	35	125	35	10
14		35	20	60	15		45	15	10			125	30	130	20	10
15		25	10	50	30		40	20	35			90	30	90	20	10
16		20	30	70	50		60	10	30			70	40	80	20	15
17		20	10	70	25		15	5	30			110	25	30	10	10
18		15	20	75	80		25	5	20			130	40	190	25	5
19		35	5	40	30		60	35	10			170	30	80	10	15
20		30	10	20	110		30	10	15			50	20	70	25	10
21		20	10	35	30		50	15	10			60	40	90	15	15
22		10	40	50	65		25	15	10			40	35	120	20	10
23		15	5	110	40		40	5	25			50	100	100	25	5
24		20	5	115	50		75	10	15			70	35	110	5	20
25		25	5	90	60		20	10	20			80	30	80	15	20
26		50	5	130	25		45	10	30			190	80	60	20	10
27		10	5	100	50		35	15	5			130	25	70	20	15
28		5	40	50	55		30	10	20				35	130	25	10
29		5	10	80	105		20	20	10				20	135	10	15
30		5	25	30	165		10	10	25				30	105	5	10
31		15	35	50	100		15	15	10				35	25	10	15
32		15	40	50	70		5	5	5				30	5	15	10
33		5	40	35	85		8	5	10				50	35	15	15
34		20	35	45	35		45	10	5				65	40	40	15
35		20	25	30	75		20	25	5				65	15	30	10
36		15	14	80	50		45	5	8				60	150	15	25
37		20	5	35	35		100	8	8				40	125	10	15
38		5	40	60	40		75	15	8				60	130	15	15
39		25	8	40	50		80	20	5				50	100	15	10
40		25	8		90		20	10	10				35	15	5	15
41		30	5		150		10	40	10				25	10	15	15
42		10	20		55		15	15	5				10	5	20	12
43		15	40				10	15	30				15	40	5	15
44		15	25				5	5	10				50	75	10	
45		25	15				7	10	25				25	95		
46			10				15	25	13				25	25		
47			10													
48	Average	18.40909	19.23913	60.13158	64.14634		36.11111	14.68889	13.95556		12.85714	116.3462	36.44444	88.22222	20.34884	12.07143
49	Median	20	20	50	55		30	10	10		90	125	30	90	20	10
50	SD	9.986778	12.31293	27.29931	38.04442		24.06546	10.10351	8.981352		19.02379	48.11565	21.12254	57.96899	10.65673	4.682051
51	Largest	35	40	130	180		100	40	35		125	200	100	310	50	25
52	Smallest	5	5	20	20		5	5	5		75	40	10	5	5	5

Appendix 2 – An image taken through a Carl Zeiss compound microscope with 4x zoom showcasing the crystalline structures formed during dynamic winterization, while tempering at 20°C. Note the large shards in the top and bottom, which are glass shards from the microscope slides used.
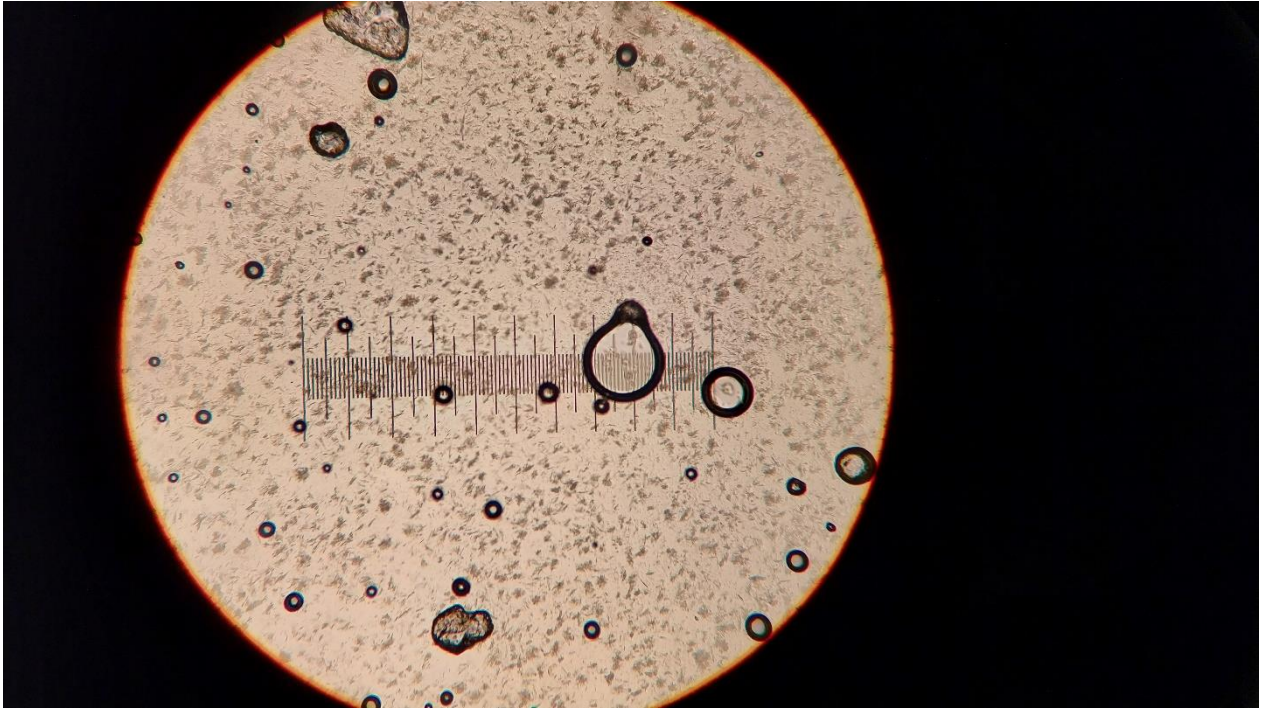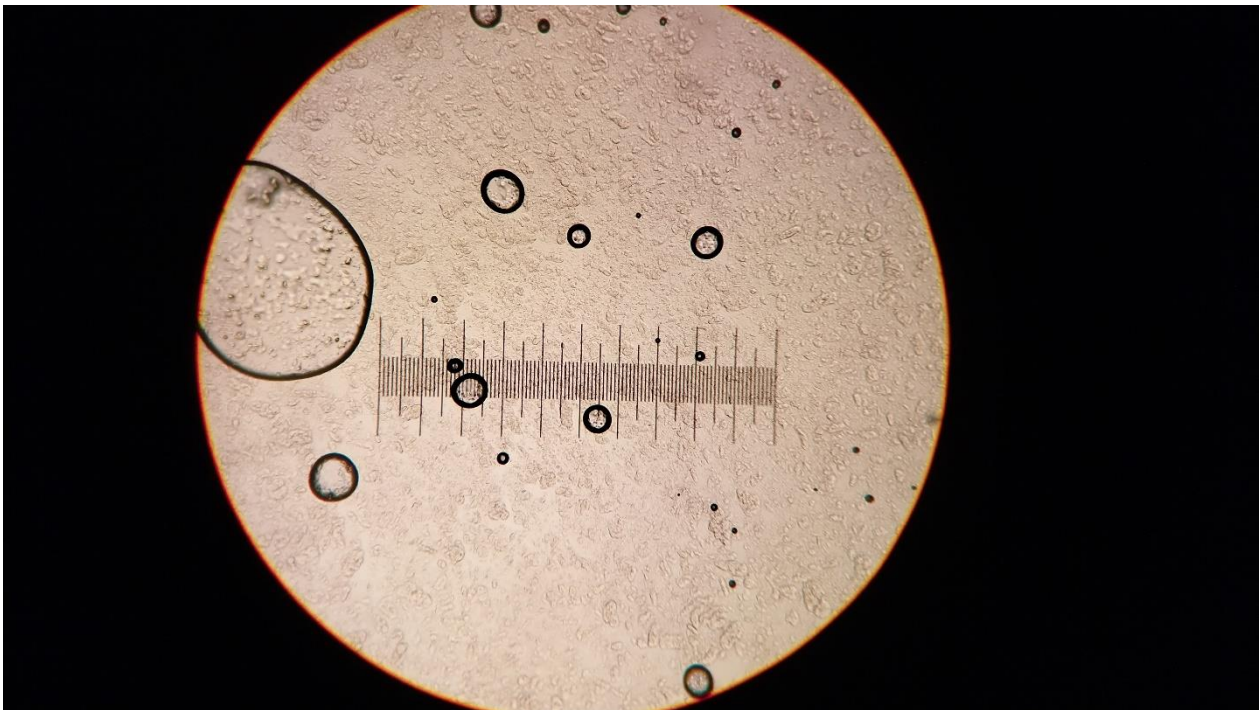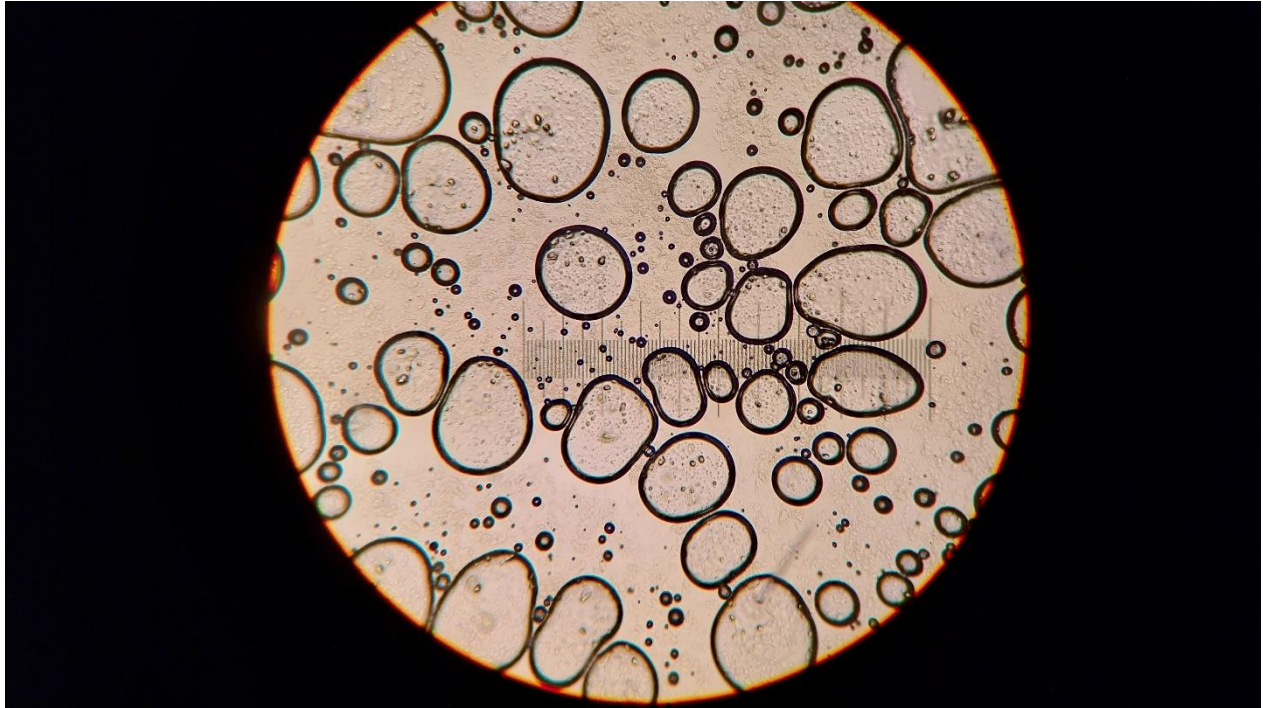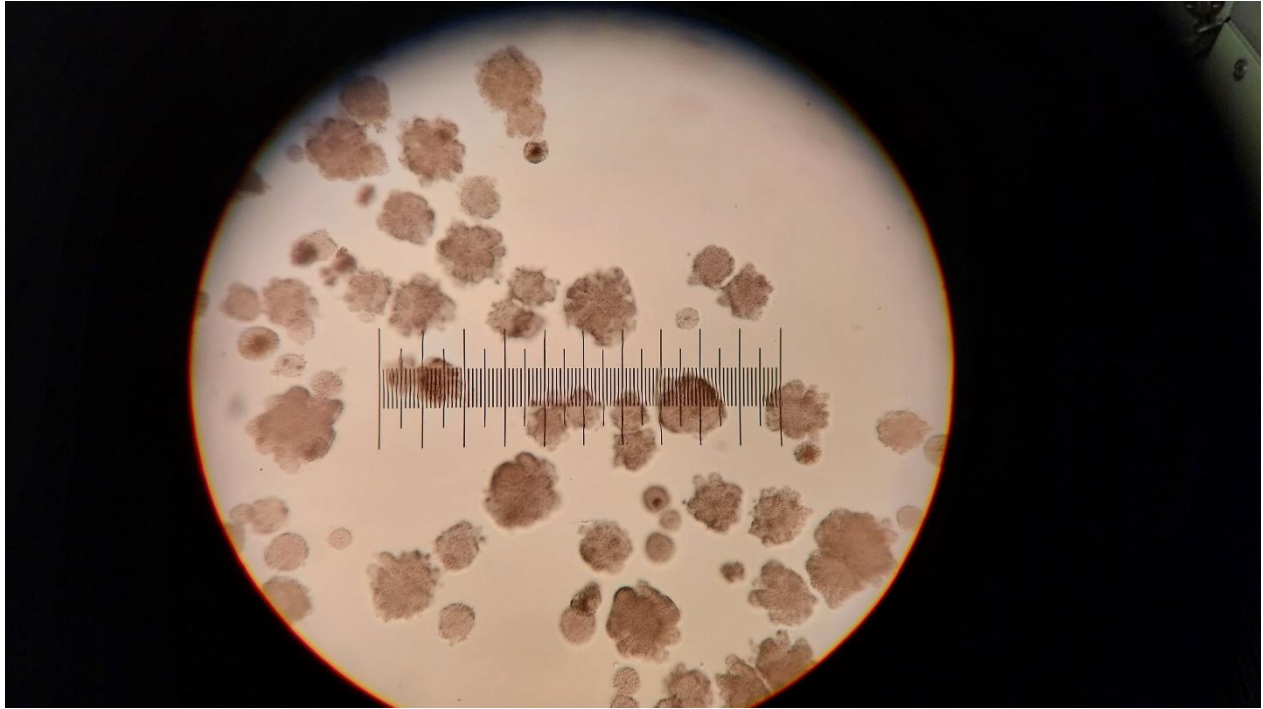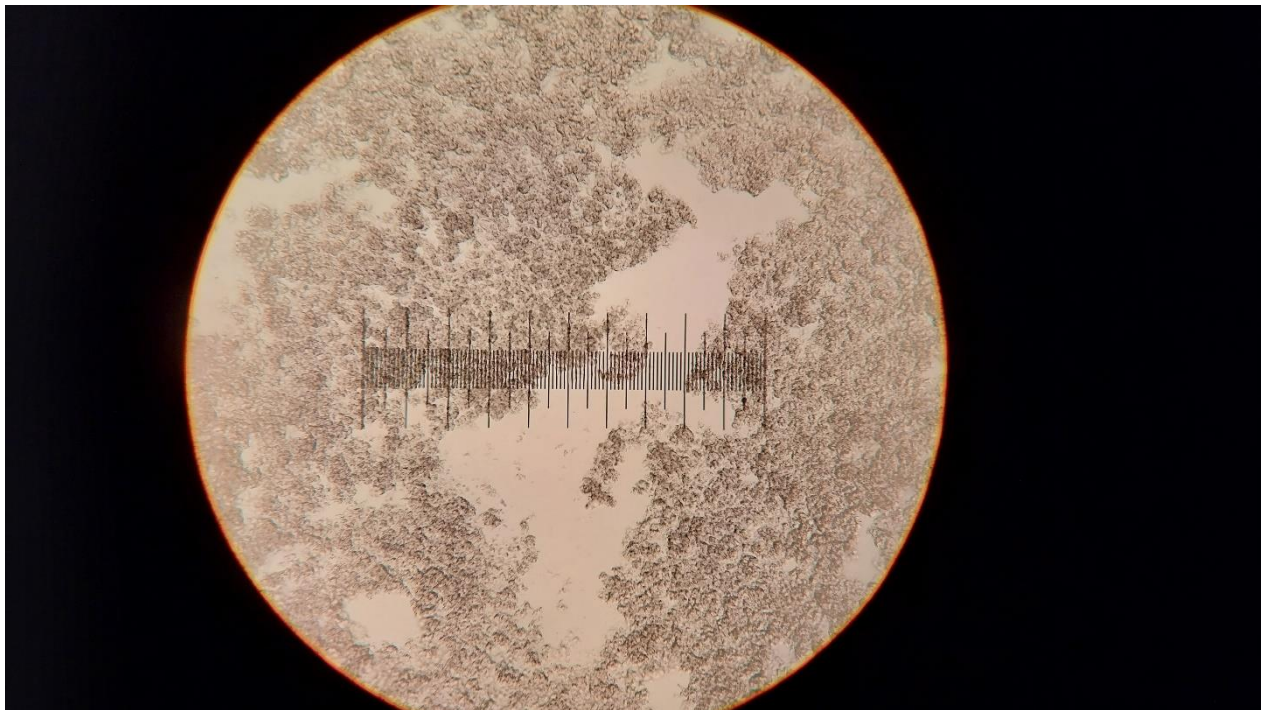
Appendix 3 – An image taken through a Carl Zeiss compound microscope with 4x zoom showcasing the crystalline structures formed during dynamic winterization, while tempering at 15°C.

Appendix 4 - An image taken through a Carl Zeiss compound microscope with 4x zoom showcasing the crystalline structures formed during dynamic winterization, while tempering at 12°C.
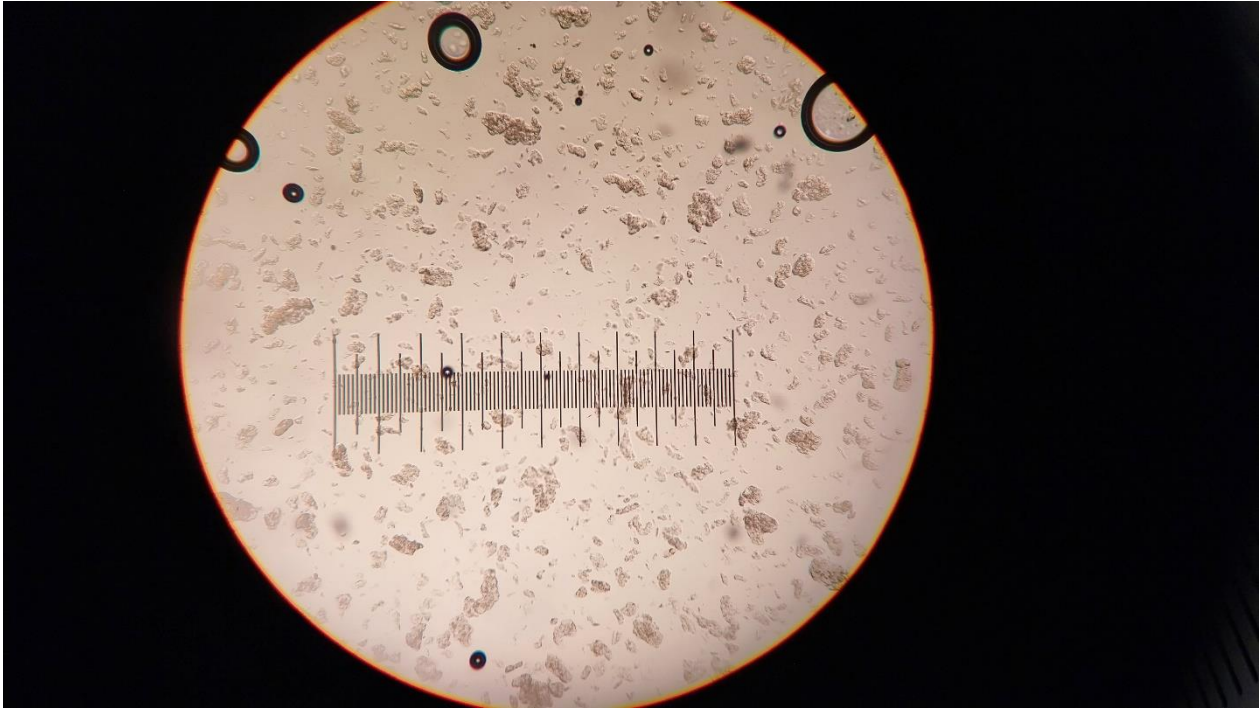
Appendix 5 – An image taken through a Carl Zeiss compound microscope with 4x zoom showcasing the crystalline structures formed during dynamic winterization, while tempering at 10°C.

Appendix 6 – An image taken through a Carl Zeiss compound microscope with 4x zoom showcasing the crystalline structures formed during dynamic winterization, while tempering at 8°C. Note the large circular structures, which are all air bubbles formed in solution.

Appendix 7 – An image taken through a Carl Zeiss compound microscope with 4x zoom showcasing the crystalline structures formed during static winterization, while tempering at 20°C.

Appendix 8 – An image taken through a Carl Zeiss compound microscope with 4x zoom showcasing the crystalline structures formed during static winterization, while tempering at 15℃.

Appendix 9 – An image taken through a Carl Zeiss compound microscope with 4x zoom showcasing the crystalline structures formed during static winterization, while tempering at 10℃.

Appendix 10 – An image taken through a Carl Zeiss compound microscope with 4x zoom showcasing the crystalline structures formed during static winterization, while tempering at 4°C.
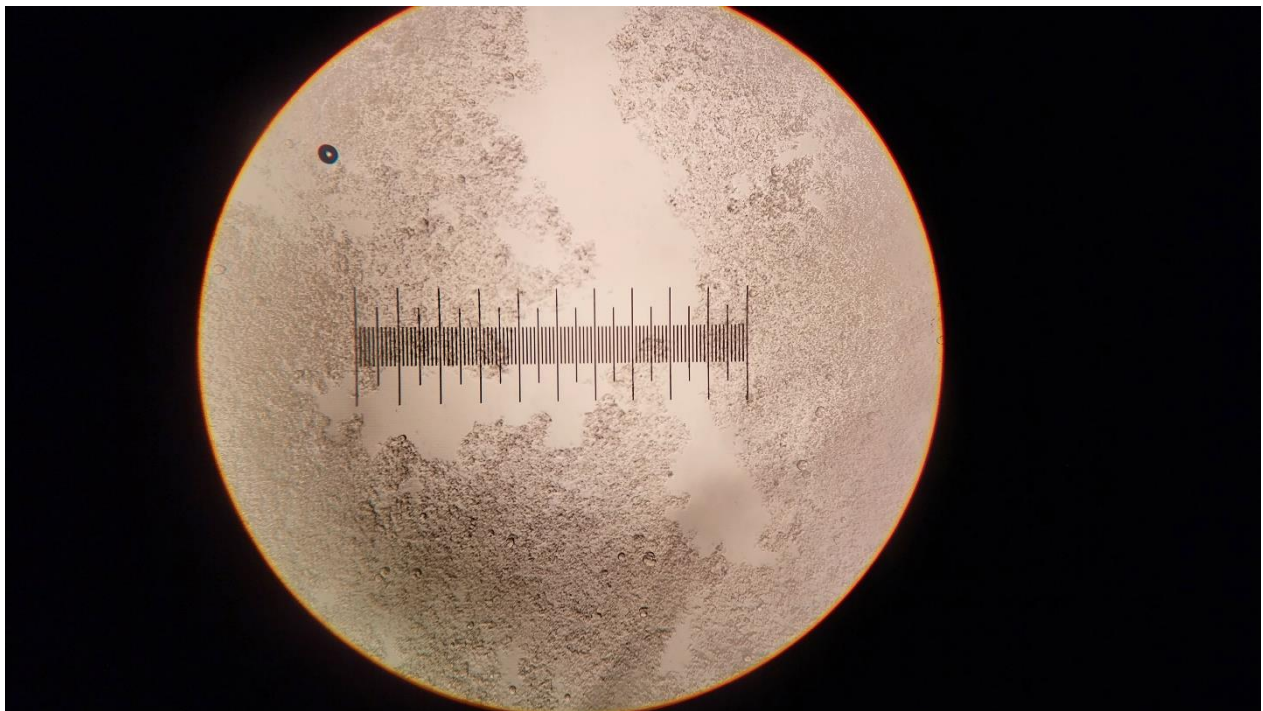
Appendix 11 – A GC graph of the commercial fatty acid standard "Advanced FAME Supelco 37" which was utilized during GC analysis, with all peaks identified with the respective fatty acid.
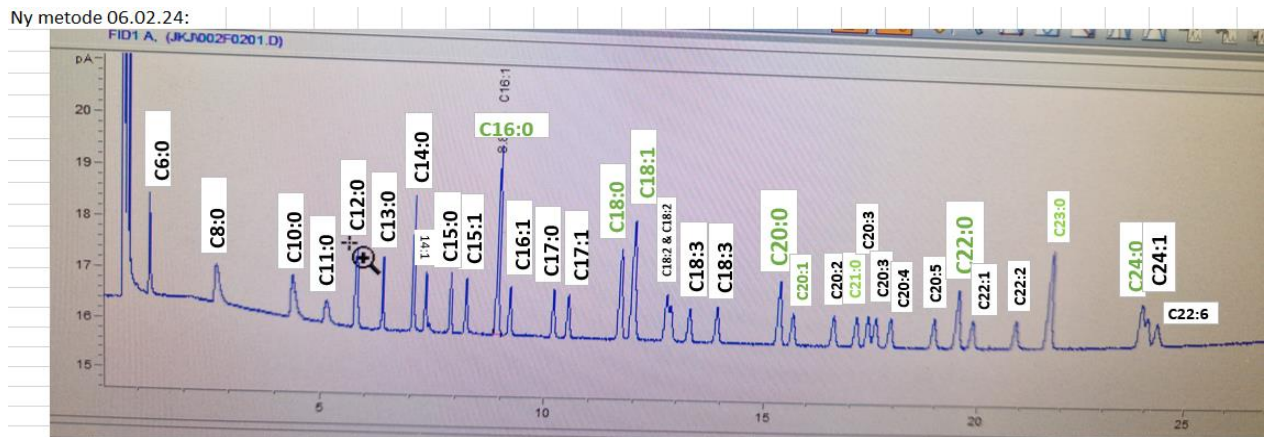
Appendix 12 – The GC graph of the commercial fatty acid standard utilized during GC analysis, which was run alongside the samples. This was the basis for the retention time of each fatty acid.
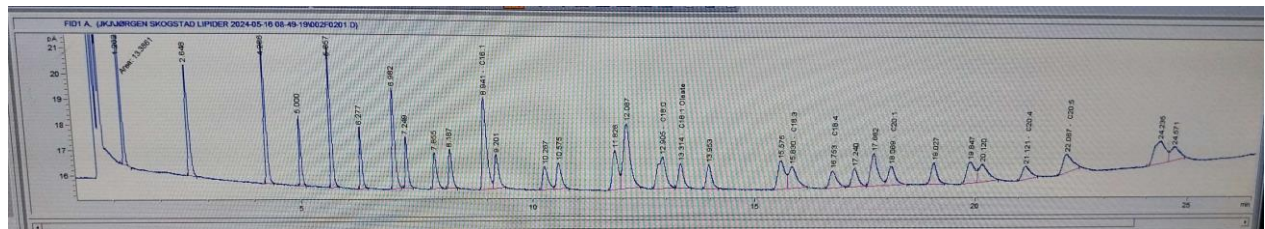
Appendix 13 – The GC graph for dynamic winterization, solid fraction 50°C-20°C temperature range
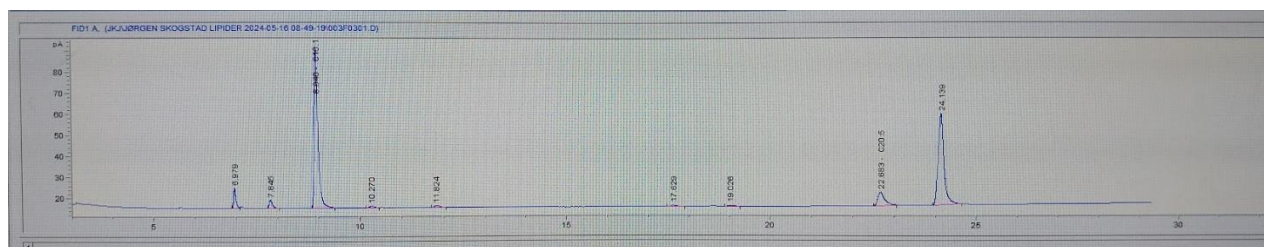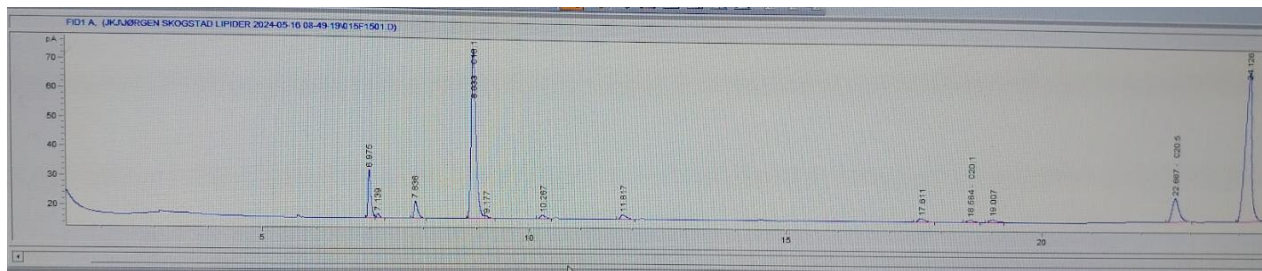

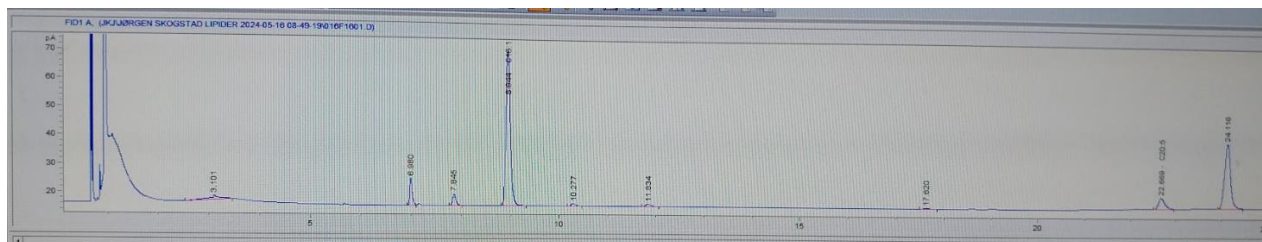Appendix 14 - The GC graph for dynamic winterization, solid fraction 20°C-15°C temperature range
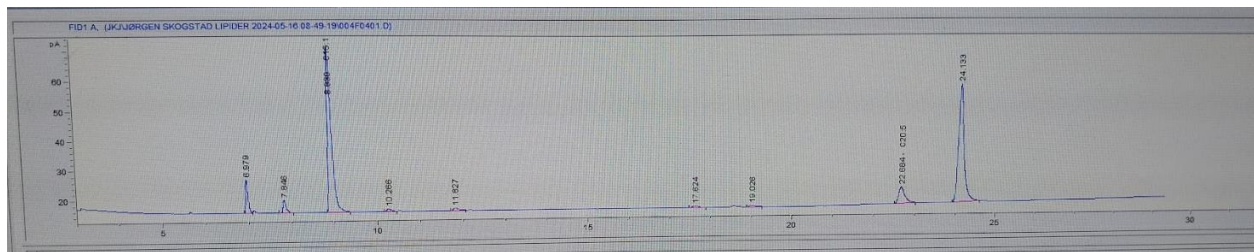
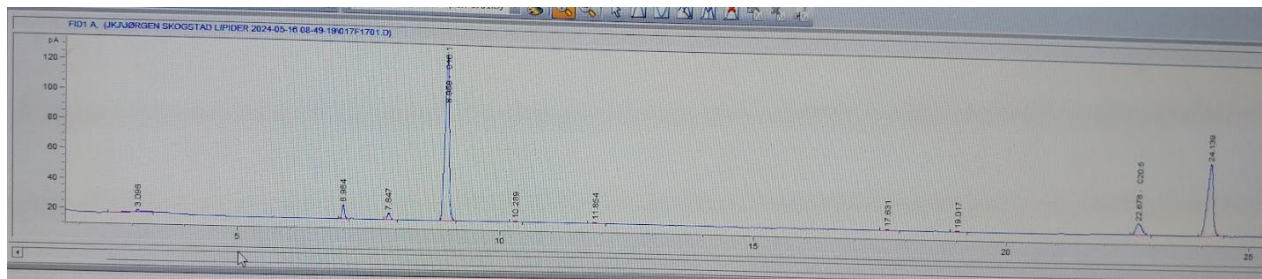Appendix 15 - The GC graph for dynamic winterization, solid fraction 15°C-12°C temperature range
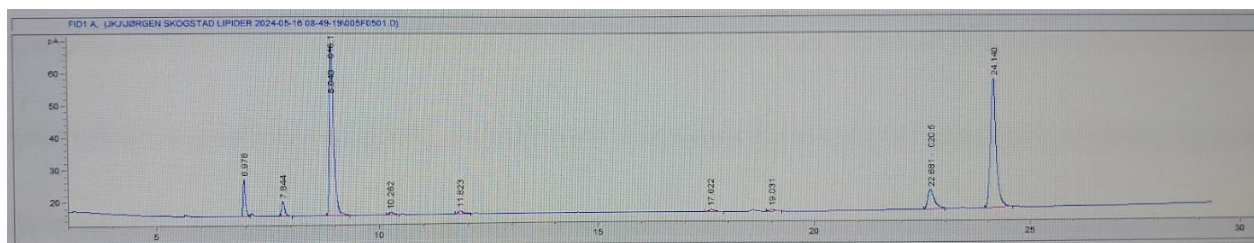
Appendix 16 – The GC graph for dynamic winterization, solid fraction 12°C-10°C temperature range
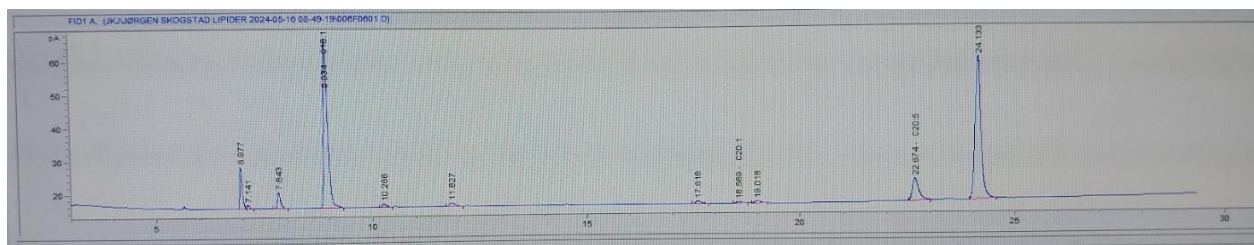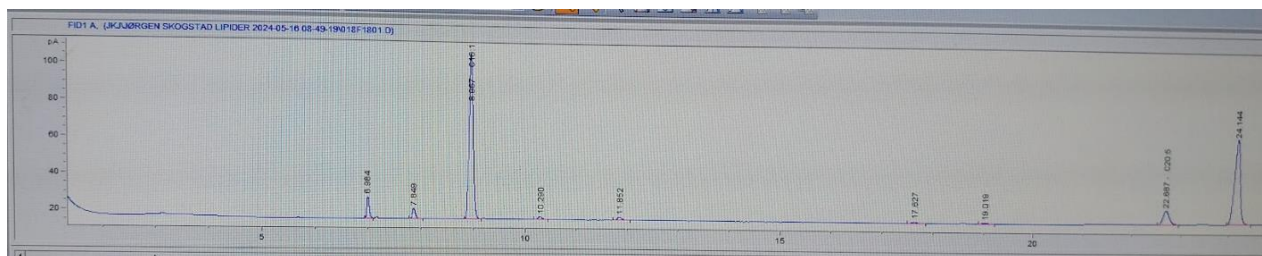

Appendix 17 – The GC graph for dynamic winterization, solid fraction 10°C-8°C temperature range
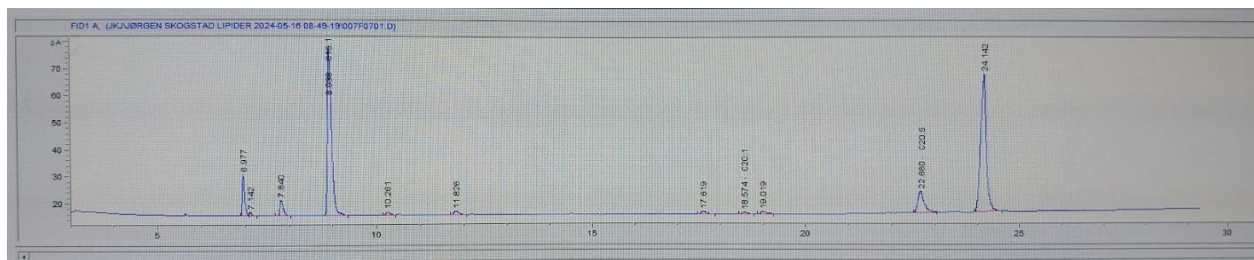
Appendix 18 – The GC graph for dynamic winterization, liquid fraction 50°C-20°C temperature range
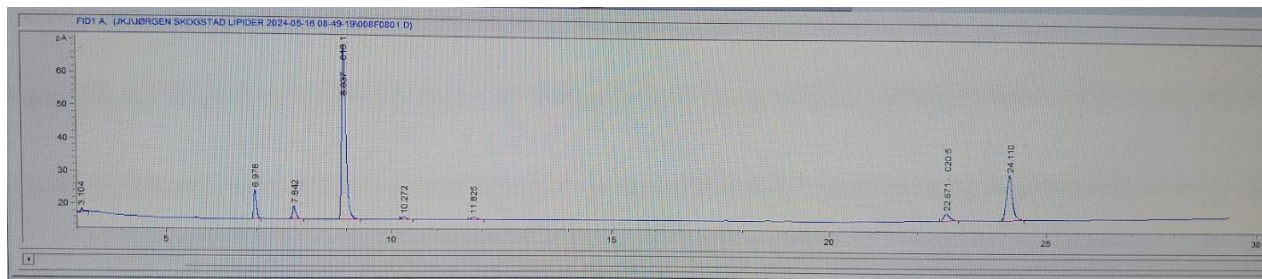
Appendix 19 – The GC graph for dynamic winterization, liquid fraction 20℃-15℃ temperature range
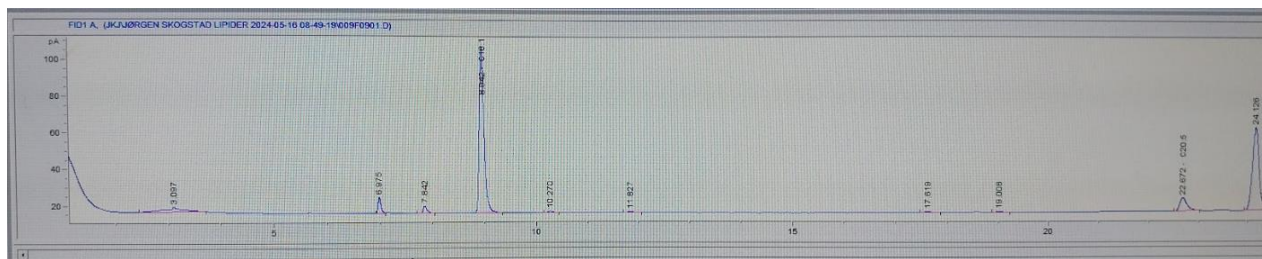
Appendix 20 - The GC graph for dynamic winterization, liquid fraction 15℃-12℃ temperature range

Appendix 21 - The GC graph for dynamic winterization, liquid fraction 12℃-10℃ temperature range

Appendix 22 - The GC graph for dynamic winterization, liquid fraction 10℃-8℃ temperature range

Appendix 23 - The GC graph for static winterization, liquid fraction 50°C-20°C temperature range
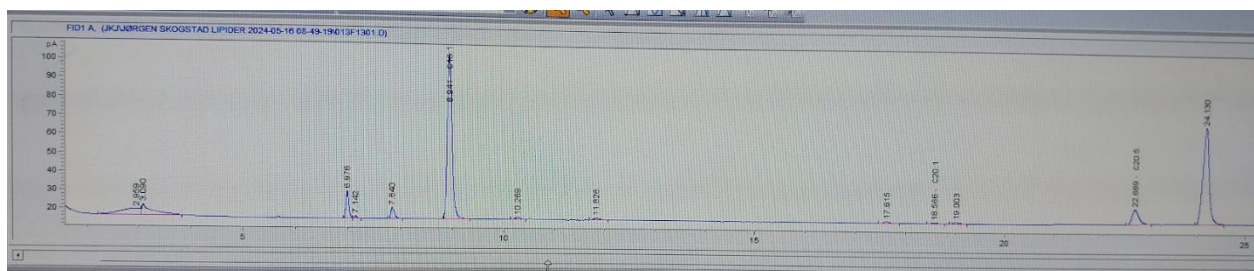
Appendix 24 - The GC graph for static winterization, liquid fraction 20°C-15°C temperature range
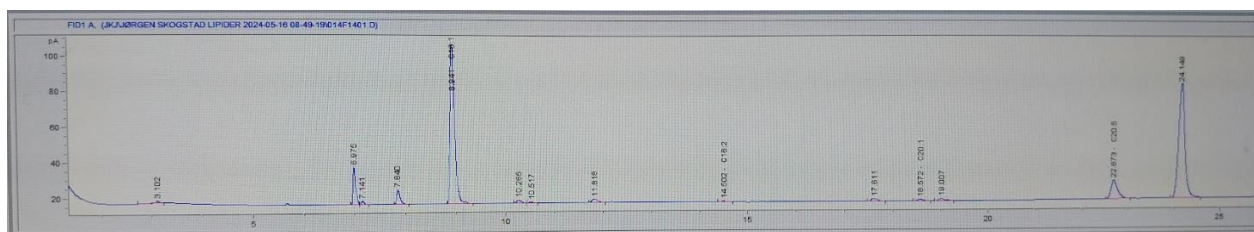
Appendix 25 - The GC graph for static winterization, liquid fraction 15°C-10°C temperature range
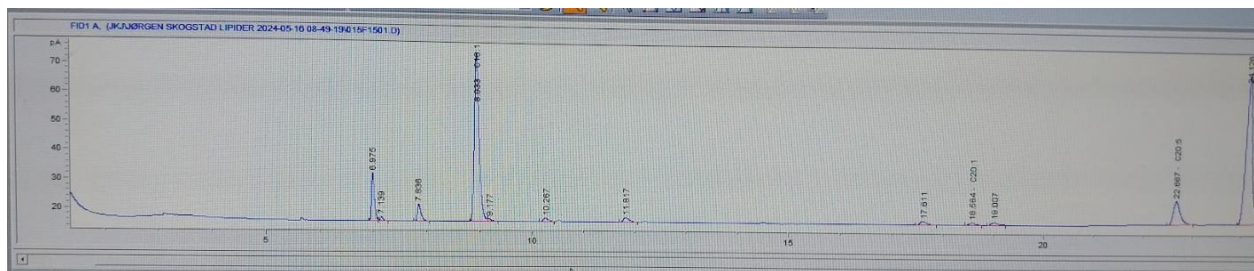
Appendix 26 - The GC graph for static winterization, liquid fraction 10°C-4°C temperature range

Appendix 27 - The GC graph for static winterization, solid fraction 50°C-20°C temperature range

Appendix 28 - The GC graph for static winterization, solid fraction 20°C-15°C temperature range

Appendix 29 - The GC graph for static winterization, solid fraction 15°C-10°C temperature range

Appendix 30 - The GC graph for static winterization, solid fraction 10°C-4°C temperature range. Note the large peak in the first minute. This is the assumed contamination peak.
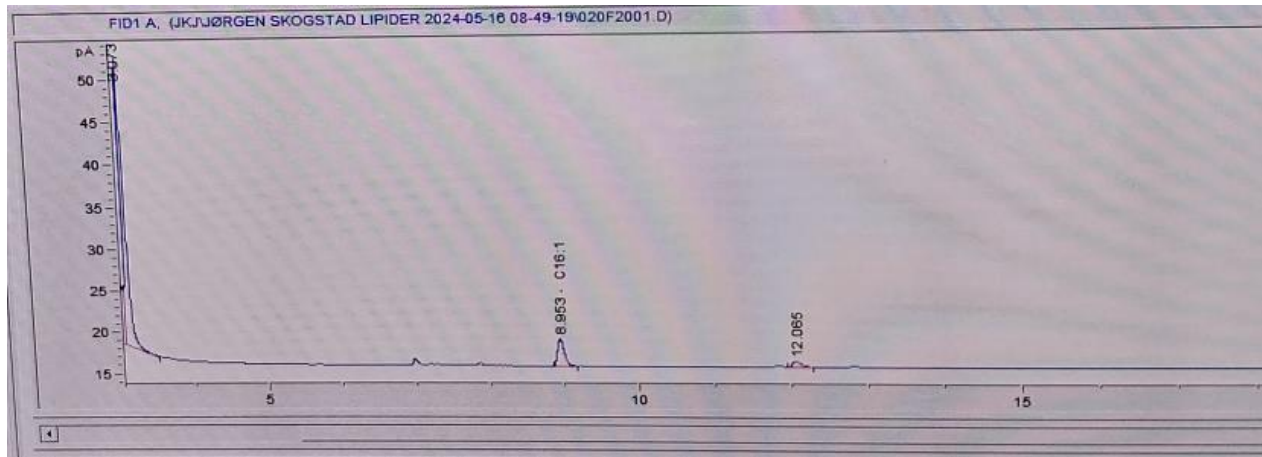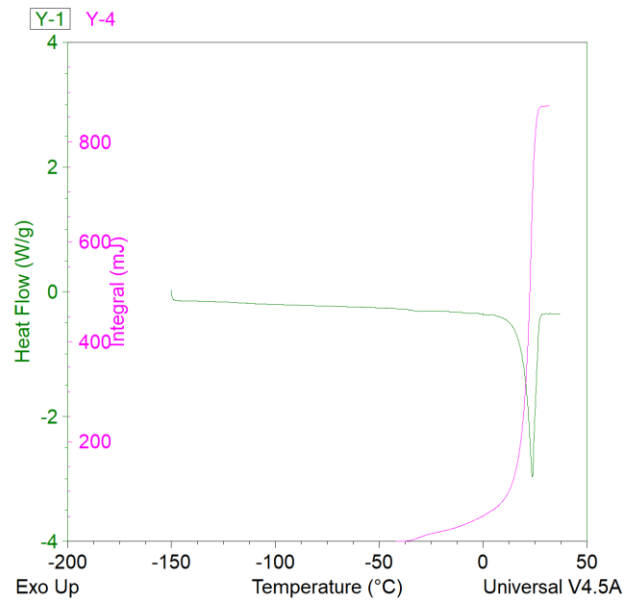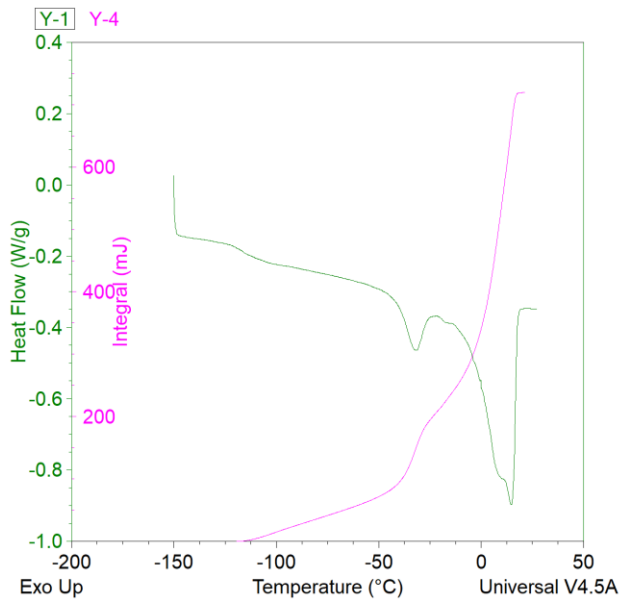
Appendix 31 – The DSC graphs for dynamic winterization temperature range 50°C-20°C with the liquid and solid fractions respectively depicted. The green line depicts the heat flow at the given temperature, while the pink line is the inverted running integral run alongside the chosen temperature range.
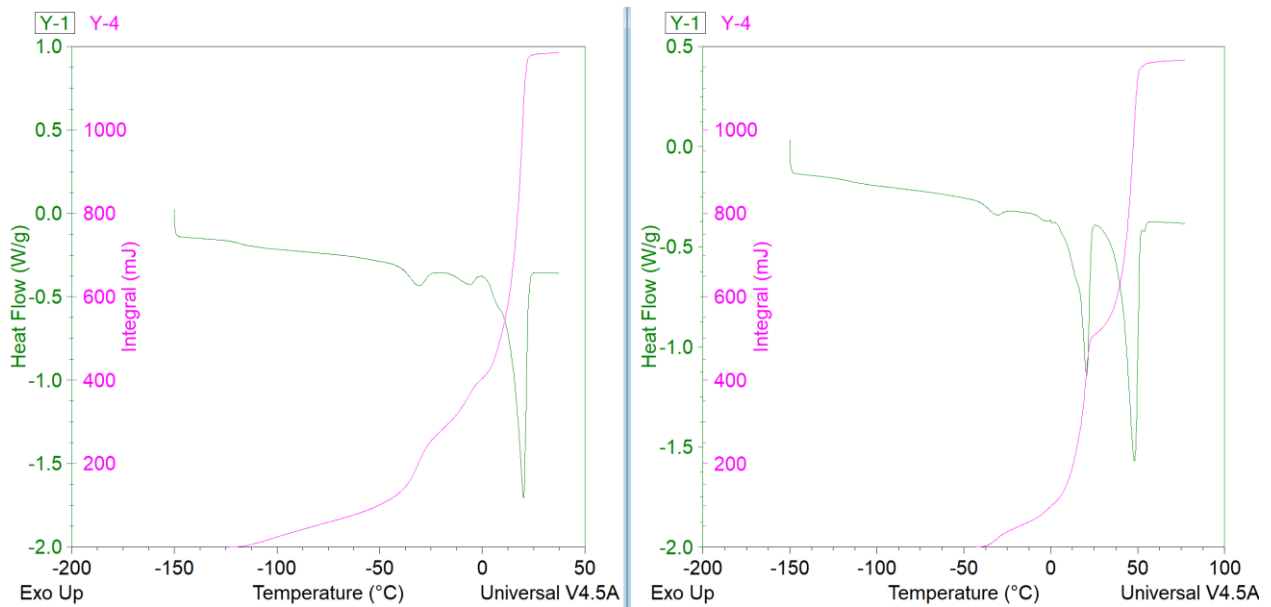
Appendix 32 – The DSC graphs for dynamic winterization temperature range 20°C-15°C with the liquid and solid fractions respectively depicted. The green line depicts the heat flow at the given temperature, while the pink line is the inverted running integral run alongside the chosen temperature range.
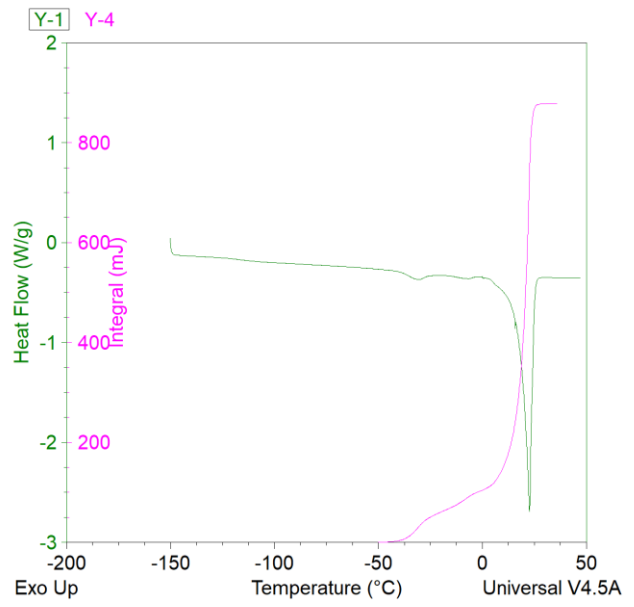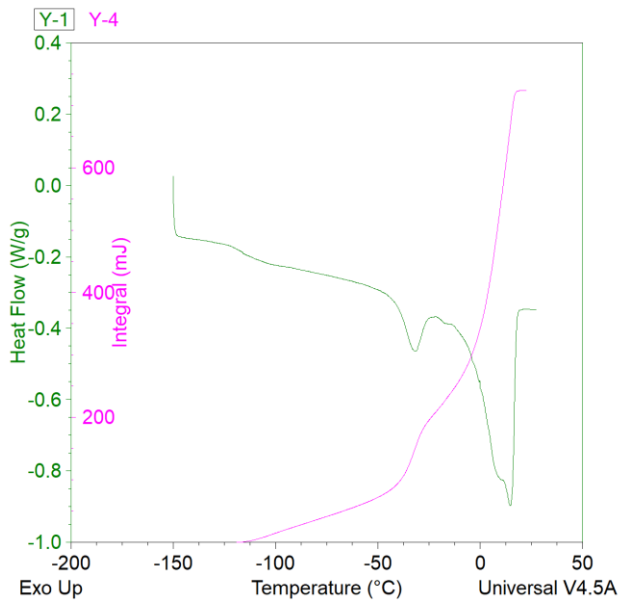
Appendix 33 – The DSC graphs for dynamic winterization temperature range 15°C-12°C with the liquid and solid fractions respectively depicted. The green line depicts the heat flow at the given temperature, while the pink line is the inverted running integral run alongside the chosen temperature range.